Università degli Studi di Ferrara

Dottorato di Ricerca in FISICA

XIX Ciclo

Coordinatore Prof. Filippo Frontera

Quality assurance and Quality control on the MWPCs for the LHCb Experiment

Candidato
Dott. Antonio Franconieri

Tutore
Prof. Mauro Savriè

Anno 2004/2006

Contents

Introduction **1**

1 CP Violation in the Standard Model **3**
Introduction . . . 3
1.1 C, P and T symmetries . . . 4
1.2 CP Violation . . . 5
1.3 The $B^0 - \bar{B}^0$ system . . . 8
1.4 Classification of CP-Violating effects . . . 13
1.4.1 *Direct* CP violation. . . . 14
1.4.2 *Indirect* CP violation . . . 15
1.4.3 CP violation in *interference* of mixing and decay. . . . 16
1.5 CKM-Parameters calculation and important decays . . . 18
1.5.1 $B_d^0 \to \pi^+\pi^-$ . . . 19
1.5.2 $B_d^0 \to J/\Psi K_s^0$ . . . 21
1.5.3 $B_s^0 \to D_s^- K^+$ . . . 23
1.5.4 $B_s^0 \to J/\Psi\Phi$, . . . 24
1.5.5 Global fit in the Standard Model . . . 25
1.6 Decay reconstruction method. . . . 26

2 LHCb Experiment at LHC **29**
Introduction . . . 29
2.1 LHC and p-p physics . . . 30
2.2 LHCb Detector . . . 34
2.2.1 The Vertex Locator (VELO) . . . 35
2.2.2 Ring Imaging Cherenkov Detectors . . . 37
2.2.2.1 RICH 1 . . . 37
2.2.2.2 RICH 2 . . . 38
2.2.3 Tracking System . . . 39
2.2.3.1 The Trigger Tracker (TT) . . . 40
2.2.3.2 Dipole Magnet . . . 41
2.2.3.3 Tracking Stations . . . 41
2.2.4 Calorimeter System . . . 42
2.2.4.1 Scintillator Pad Detector (SPD) and PreShower detector (PS) . . . 42

2.2.4.2 The Electromagnetic Calorimeter 43
2.2.4.3 The Hadron Calorimeter 43
2.2.5 Muon System 44
2.2.6 Trigger 44
2.2.6.1 The Level-0 trigger 45
2.2.6.2 The Level-1 trigger 45
2.2.6.3 The High Level Trigger 46
2.2.7 Software Framework 46
2.2.7.1 Simulation 47
2.2.7.2 Analysis 47
2.3 Muon System 48
2.3.1 Detector structure 49
2.3.2 Level-0 muon trigger 53
2.3.3 The Multiwire Proportional Chambers 55
2.3.4 Electronics 58

3 Quality Management Systems 61
Introduction 61
3.1 ISO 9001:2000 and Process Approach 62
3.2 QMS and Documentations 63
3.2.1 Documentation requirements 64
3.3 Management responsibility 65
3.4 Resource management 67
3.5 Product realization 67
3.5.1 Planning 67
3.5.2 Product requirements 68
3.5.3 Design and development 68
3.5.4 Material Purchasing (supply) 69
3.5.5 Supplying informations 69
3.5.6 Verification of purchased product 69
3.5.7 Production and service provision 70
3.5.8 Identification and traceability 70
3.5.9 Preservation of product and customer property 70
3.5.10 Control of monitoring and measuring devices 71
3.6 Measurement, analysis and improvement 71
3.6.1 Internal inspections 72
3.6.2 Monitoring and measurement of processes and products . 72
3.6.3 Control of nonconforming product 72
3.6.4 Analysis of data 73
3.6.5 Corrective and Preventive actions 73

4 MWPC production in Ferrara 75
Introduction 75
4.1 Pre-production Tests 76
4.1.1 Panel planarity, cleaning and visual inspections 76
4.1.2 HV bar Height 77

4.2 Production . . . 79
4.2.1 Wiring . . . 82
4.2.2 WPM (Wire Pitch Measurement) . . . 85
4.2.3 Panel gluing . . . 85
4.2.4 Soldering process . . . 89
4.2.5 WTM . . . 91
4.2.6 Preliminary HV Conditioning & HV Test . . . 93
4.2.7 Assembling . . . 95
4.2.7.1 Panels preparation . . . 97
4.2.7.2 Chamber Assembling . . . 97
4.3 Post-production test . . . 100
4.3.1 Gas Tightness . . . 100
4.3.2 HV Test . . . 102
4.3.2.1 HV conditioning (direct and reverse polarity) . . . 103
4.3.2.2 Current Leak scan . . . 105
4.3.3 Gas Gain Uniformity test . . . 105

5 GIF tests, production and quality control results 113
Introduction . . . 113
5.1 Gamma Irradiation Facility tests . . . 113
5.1.1 Experimental setup and performed test . . . 115
5.1.2 Test results . . . 117
5.2 Production summary . . . 119
5.3 Pre-production test results . . . 123
5.3.1 HV bar height measurement results . . . 123
5.4 Production Tests . . . 142
5.4.1 WPM results . . . 142
5.4.2 WTM results . . . 153
5.5 Post-production Tests . . . 160
5.5.1 Gas tightness test results . . . 160
5.5.2 HV test results . . . 164
5.5.3 Gas gain uniformity test results . . . 168

Conclusions 175

March 9, 2007

Introduction

The LHCb experiment will take place at the LHC accelerator at CERN in 2007. It is a single arm spectrometer dedicated to study CP violation and rare phenomena in b hadron decays. LHCb is designed to pursue an extensive program on B-physics, over-constraining the Standard Model predictions about CP violation, and looking also for any possible inconsistency in the theory.

The LHCb experiment has finished its R&D at the end of 2003, when the re-optimized design of the detector has been carried out. At the time of this thesis, the detector is under construction and it is expected to be complete for the first data taking in the second half of 2007. The LHCb Muon System will play a fundamental role in the experiment. Muon triggering and offline muon identification are in fact fundamental requirements of the LHCb experiment: muons are present in the final states of many CP-sensitive B decays and also in some rare B decays which may reveal new physics beyond the Standard Model.

The muon detector will be equipped with 1368 multiwire proportional chambers (MWPC) produced in six different sites; one of these sites is located in Ferrara, where the production and test of more than 200 MWPC has been carried out since 2004. Subject of this thesis is the detailed description of all the procedures concerning production performed in the Ferrara site, focusing the interest on Quality assurance and Quality control tests.

Chapter 1 introduces the formalism to describe CP violation in the Standard Model and the mixing of neutral B mesons. The phenomenology of CP violation measurements is also introduced, considering the four most interesting decay channels used to reconstruct the 'Unitarity Triangles'. The requirement to determine the flavor of the neutral B meson at production is also discussed, including the effect any wrong tag assignment has on the systematic error of the asymmetry measurement

Chapter 2 gives an overview of the LHCb detector design, starting from the LHC accelerator and ending with the Muon Spectrometer. All sub-detectors are briefly described while a very detailed description of the Muon Detector is finally given considering also the LHCb software for simulation, reconstruction and analysis.

In *Chapter 3* are summarized the used guidelines in the implementation of a Quality Management System (QMS). The considered statements, given by ISO 9001:2000 normative, have been used to improve the effectiveness of the QMS adopted for the construction of the MWPC described in the following chapter.

Chapter 4 is aimed to describe deeply all the procedures, specifications and requirements, concerning the MWPC constructed in the Ferrara site. A full description of the MWPC construction method is given, considering each step individually, and focusing the interest on the various quality tests performed, needed to ensure the satisfaction of the quality requirements given by the LHCb collaboration.

In *Chapter 5* are then presented the results concerning production and quality tests, considering separately the different typologies of MWPC constructed, and then summarizing the results for the whole production.

Chapter 1

CP Violation in the Standard Model

Introduction

The Standard Model of Particle Physics is a theory which describes the strong, weak, and electromagnetic fundamental forces, as well as the fundamental particles that make up all matter: it is a quantum field theory, and consistent with both quantum mechanics and special relativity.

The basic building blocks of matter are six leptons and six quarks that interact by means of force-carrying particles called bosons. Every phenomenon observed in nature should be understood as the interplay of the fundamental particles and forces of the Standard Model (SM), but, at present, we know that the Standard Model does not tell the whole story, and physicists all over the world are searching for physics beyond the Standard Model that will lead to a larger, more elegant "theory of everything" (GUT[1]).

The need of a larger theory has to be searched in the weak spots of the Standard Model and in all of its unanswered questions. First of all it does not include a theory of gravity; the origin of mass in the Standard Model is described by the Higgs theory, but the Higgs boson has not yet observed; and last, but perhaps the most important, a large number of parameters in the theory are not fundamental, but must be measured experimentally.

Some of these free parameters are the phases which govern the breaking of the CP symmetry, so that CP violation could be considered one of the weak spots of the Standard Model, because it does not have a fundamental, well explained, origin.

Several experiments in the next years will provide an effort for checking the SM and searching proofs for new Physics (Physics Beyond the Standard Model),

[1]Grand unification, grand unified theory, or GUT is one of several very similar theories or models in physics that unify what are considered three "fundamental" gauge symmetries: hypercharge, the weak force, and quantum chromodynamics.

and so that, CP violation will play a crucial role. Cosmological observations demonstrated that anti-matter almost disappeared, under the hypothesis that it was present in the same amount of matter at the beginning of the Universe, after the Big Bang. So, the observed asymmetry between matter and antimatter in our universe requires large CP-violating effects[1]. Through these experiments we will understand if this CP violation can be fitted into the current theory, or if it will lead to the success of theories based on New Physics.

1.1 C, P and T symmetries

The interactions, in the Standard Model, arise from the requirement that the theory is invariant[2] under local gauge transformations[2]. Invariance under a local complex phase transformation, U(1) symmetry, leads to the electromagnetic interaction and the conservation of charge. The electroweak theory is derived by combining this, with invariance under a local, non-Abelian SU(2) group of isospin transformations. In the electroweak theory the weak hypercharge current is conserved, and the interactions are mediated by three massive and one massless vector gauge bosons. The theory of the strong interaction, QCD, follows from invariance under the SU(3) group of local color transformations indicating the color current is conserved.

In the case of discrete symmetries, the operators of the group can have only a finite number of values. This is true for the transformations of charge conjugation, parity and time reversal.

Under C, particles and antiparticles are interchanged, by conjugating all internal quantum numbers in the system, eg. $Q \rightarrow -Q$ for electromagnetic charge.

Under P, the handness of space is reversed, so: $x \rightarrow -x$, $y \rightarrow -y$, $z \rightarrow -z$.

Under T, we have a time reversal operation that transforms t to -t by mean of an anti-unitary operator, with $T \mid f(t,x) > \rightarrow \mid f^*(-t,x) >$.

We know that discrete symmetries can be broken. If CP was an exact symmetry, the laws of Nature would be the same for matter and for antimatter. We observe that most phenomena are C- and P-symmetric, and therefore, also CP-symmetric; in addition CPT is a fundamental symmetry of all quantum field theories. In particular, all of these symmetries are respected by the gravitational, electromagnetic and strong interactions. The weak interaction, on the other side, violates C and P in the strongest possible way[3], and also a T violation have been observed in neutral K decays[3].

[2]When a physical system is invariant under a particular transformation we can introduce a Symmetry. Translation and rotation in space are examples of continuous symmetries where the parameters of the operators in the symmetry group have an infinite number of values. The invariance of the laws of physics under translation and rotation leads to the conservation of linear and angular momentum.

[3]The charged W boson only couples to the left-handed electron, e_L^-, and not to the P-conjugate right-handed electron, e_R^-, or the C-conjugate left-handed positron, e_L^+.

While weak interactions violate C and P separately, CP is still preserved in most weak interactions processes [4]. The CP symmetry is however, violated in certain rare processes, as discovered in neutral K decays in 1964, and more recently, in decays of neutral B_d mesons by the BaBar[4] and Belle[5] B-factories. The B meson system is supposed to be a very promising source for CP violation studies, but until now it has not been possible to study the B_s meson[5].

At LHCb, considering the large amount of energy available in the center of mass, all the b species can be studied, and in particular here it will be provided the most significant measurements of CP symmetry violation in the B_s system. By mean of it, we will be able to check the Standard Model predictions for CP violation, and therefore, we will have the possibility to search for new physics beyond the Standard Model.

1.2 CP Violation

In the Standard Model of weak and electroweak interactions, CP violation arises from the presence of a single irremovable phase in the unitary complex mixing matrix for the three quark generations:

$$\begin{pmatrix} u \\ d \end{pmatrix} , \begin{pmatrix} c \\ s \end{pmatrix} , \begin{pmatrix} t \\ b \end{pmatrix} . \tag{1.1}$$

The quarks participate in the weak interaction as linear combinations of mass eigenstates allowing mixing between the generations. Each generation of massive fermions is composed of a doublet of left-handed particles, weak isospin $+\frac{1}{2}$ and $-\frac{1}{2}$, and two right-handed singlet particles, weak isospin 0. The weak interaction couples only to the left-handed component of a particle.

The irremovable phase is called the Kobayashi-Maskawa phase, and the matrix, which allows to pass from mass eigenstates to weak interaction eigenstates, is the well known Cabibbo-Kobayashi-Maskawa (CKM) mixing matrix. Flavor changing processes between the quarks are only permitted via charged current interactions with couplings given by the CKM matrix:

$$V_{CKM} = \begin{pmatrix} V_{ud} & V_{us} & V_{ub} \\ V_{cd} & V_{cs} & V_{cb} \\ V_{td} & V_{ts} & V_{tb} \end{pmatrix} \tag{1.2}$$

[4]The charged W boson has the same coupling to the CP-conjugate of the left-handed electron, the right handed positron e^+_R.

[5]B-factories operate at the Υ(4S)-resonance with a mass of 10.58 GeV, and therefore they can only study the decays of B_d mesons.

Such a 3 x 3 unitary matrix can have 9 independent parameters, counting the real and imaginary parts of a complex element as two parameters. Since there can be 6 fermions involved in the charged weak current, there are 5 relative phase transformations, leaving 4 independent parameters. The 4 independent parameters consist of 3 mixing angles between the 3 generations of quarks θ_{12}, θ_{13}, θ_{23}, and a single complex phase, δ_{13}.

The CKM matrix can be explicitly parametrized as shown here, where $c_{ij} = \cos\theta_{ij}$ and $s_{ij} = \sin\theta_{ij}$:

$$V_{CKM} = \begin{pmatrix} c_{12}c_{13} & s_{12}c_{13} & s_{13}e^{-i\delta_{13}} \\ -s_{12}c_{23} - c_{12}s_{23}s_{13}e^{i\delta_{13}} & c_{12}c_{23} - s_{12}s_{23}s_{13}e^{i\delta_{13}} & s_{23}c_{13} \\ s_{12}s_{23} - c_{12}s_{23}s_{13}e^{i\delta_{13}} & -c_{12}s_{23} - s_{12}c_{23}s_{13}e^{i\delta_{13}} & c_{23}c_{13} \end{pmatrix} \quad (1.3)$$

CP symmetry holds if all the elements in the CKM matrix are real, and so the complex phase δ_{13} introduces CP violation in the Standard Model. Since there is only this single source of CP violation, the Standard Model is strongly predictive for CP asymmetries.

A useful perturbative parametrization of the CKM matrix, the Wolfenstein parametrization, is given in Equation 1.4, for 4 parameters (λ, A, ρ, η)[6]. The expansion parameter, λ, is the sine of the Cabibbo angle, and has a value $|V_{us}| = 0.22$. The expansion is given for terms up to the order λ^5, the CP violating phase is η, and A, ρ are the remaining two parameters:

$$V_{CKM} = \begin{pmatrix} 1 - \frac{1}{2}\lambda^2 - \frac{1}{8}\lambda^4 & \lambda & A\lambda^3(\rho - i\eta) \\ -\lambda + \frac{1}{2}A^2\lambda^5[1 - 2(\rho + i\eta)] & 1 - \frac{1}{2}\lambda^2 - \frac{1}{8}\lambda^4(1 + 4A^2) & A\lambda^2 \\ A\lambda^3[1 - (1 - \frac{1}{2}\lambda^2)(\rho + i\eta)] & -A\lambda^2 + + \frac{1}{2}A\lambda^4[1 - 2(\rho + i\eta)] & 1 - \frac{1}{2}A^2\lambda^4 \end{pmatrix} \quad (1.4)$$

This particular parametrization leads to an easier understanding of each single CKM matrix element, and above all of the mixing between the quark generations. In particular, the coupling between the first and second generations is $\mathcal{O}(\lambda)$, and between the second and third generations it is $\mathcal{O}(\lambda^2)$, suggesting a relative suppression factor of $\sim\lambda$ between flavor changing decays, which are otherwise equivalent. From the imaginary terms in Equation 1.4, which are proportional to η, CP violating effects will be seen in decays involving the transitions $b \to u$ and $t \to d$ to order λ^3, and smaller CP violating effects, of order λ^4, will be seen in the transition $t \to s$.

The unitarity of the CKM matrix implies various relations among its elements. There are 6 orthogonality conditions, two of these relations are specially interesting for b Physics [6]. The first one (1.5) can be obtained from the first and

[6]For studies of CP violation in the decays of B mesons the most useful unitarity relations

third column and concerns the B_d^0 mesons. The second one (1.6) is obtained from the first and third row and implies the B_s^0 mesons.

$$V_{ud}V_{ub}^* + V_{cd}V_{cb}^* + V_{td}V_{tb}^* = 0 \tag{1.5}$$

$$V_{tb}V_{ub}^* + V_{ts}V_{us}^* + V_{td}V_{ud}^* = 0 \tag{1.6}$$

Each orthogonality condition requires the sum of three complex quantities to vanish and so they can be geometrically represented in the complex plane as triangles (6 triangles with the same area). These are the "*Unitarity Triangles*".

In Figures 1.1 and 1.2 are shown the triangles representing the two unitarity conditions 1.5 and 1.6: the sides of each one have been divided by $|V_{cd}^*V_{cb}|$, so that the base of the first triangle extends from the origin of the diagram to the point (1,0).

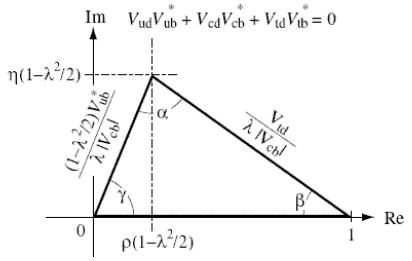

Figure 1.1: Unitarity triangle related to Equation 1.5.

The angles α,β, γ, $\delta\gamma$ are defined as:

$$\begin{aligned} \alpha &\equiv \arg\left(-\frac{V_{td}V_{tb}^*}{V_{ud}V_{ub}^*}\right) \quad \beta \equiv \arg\left(-\frac{V_{cd}V_{cb}^*}{V_{td}V_{tb}^*}\right) \\ \gamma &\equiv \arg\left(-\frac{V_{ud}V_{ub}^*}{V_{cd}V_{cb}^*}\right) \quad \delta\gamma \equiv \arg\left(-\frac{V_{us}^*V_{ts}}{V_{cd}V_{cb}^*}\right) \end{aligned} \tag{1.7}$$

and in Figure 1.2 the angle is: $\gamma' = \gamma - \delta\gamma$.

include one or more couplings involving the b quark and ideally have sides with lengths that are the same order in λ.

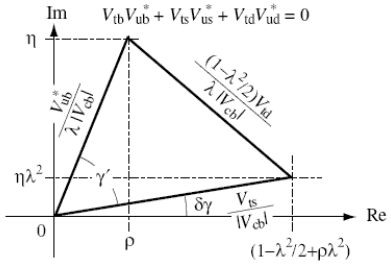

Figure 1.2: Unitarity triangle related to Equation 1.6.

The Wolfenstein parametrization and these considerations can lead us to a convention-independent description in terms of the unitarity triangles. Just taking the expression for the angle $\delta\gamma$ from Equation 1.7, and considering the contribution of each CKM matrix element as given in Equation 1.4, we can see that V_{us},V_{cd} and V_{cb} are real up to order λ^4. The only complex contribution is from V_{ts}, so that $\delta\gamma = \arg(V_{ts})$. Up to order λ^4, dividing each entry of the matrix by its modulus we will have the complex argument of each entry:

$$\begin{pmatrix} 1 & 1 & e^{-i\gamma} \\ 1 & 1 & 1 \\ e^{-i\beta} & e^{i\delta\gamma} & 1 \end{pmatrix} + \mathcal{O}(\lambda^5) \tag{1.8}$$

What is really remarkable is that up to order $\mathcal{O}(\lambda^4)$, the angles β, γ and $\delta\gamma$ are the only non-zero phases in the CKM matrix. It means that only in decays involving $b \to u$, $d \to t$ or $s \to t$ transitions we can observe CP-Violation, therefore focusing our interest on the decays of B_d^0 and B_s^0 mesons and then on the $B^0 - \bar{B}^0$ system.

1.3 The $B^0 - \bar{B}^0$ system

There are two neutral $B^0 - \bar{B}^0$ meson systems, $B_s^0 - \overline{B_s^0}$ and $B_d^0 - \overline{B_d^0}$ [7], which exhibit particle-antiparticle mixing. At the LHC both B_d^0 and B_s^0 mesons will be produced from the hadronisation of quarks with definite flavor:

$$B_q^0 = (\bar{b}q), \quad \overline{B_q^0} = (b\bar{q}) \tag{1.9}$$

[7] Generically they are denoted together as $B_q^0 - \overline{B_q^0}$, $q = s, d$.

In the Standard Model, since flavor is not conserved in the weak interaction, mixing between B_q^0 and $\bar{B}_q^0$ mesons is possible. The mixing is dominated by the box diagrams shown in Figure 1.4, where one or both t quarks can be replaced by u or c quarks. Here, as we know, the amplitude is proportional to the mass in the loop, so that the dominating contribution is due to the t quark.

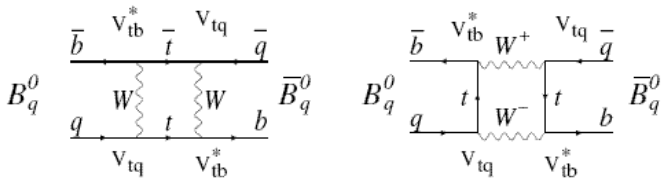

Figure 1.3: Mixing in the $B_q^0 - \overline{B_q^0}$ system.

The flavor eigenstates and the mass eigenstates are not equivalent, but the mass eigenstates are formed from a mixture of the flavor eigenstates, so that, we can write the composition of such a mass eigenstate, ψ, as follows:

$$|\psi(t)>= a(t)|B_q> +b(t)|\overline{B_q}> \tag{1.10}$$

Then the Schrödinger equation, $i\frac{d}{dt}\begin{pmatrix} a(t) \\ b(t) \end{pmatrix} = H\begin{pmatrix} a(t) \\ b(t) \end{pmatrix}$, give us the time evolution of this state, so we can write the Hamiltonian as follows:

$$H = \begin{bmatrix} h_{11} & h_{12} \\ h_{21} & h_{22} \end{bmatrix} = M - \frac{i}{2}\Gamma = \left(\begin{bmatrix} M_{11} & M_{12} \\ M_{21}^* & M_{22} \end{bmatrix} - \begin{bmatrix} \Gamma_{11} & \Gamma_{12} \\ \Gamma_{21}^* & \Gamma_{22} \end{bmatrix} \right) \tag{1.11}$$

where the Hermitian matrices M and Γ are defined as $M = \frac{1}{2}\left(H + H^\dagger\right)$, and $\Gamma = i\left(H + H^\dagger\right)$.

To have an invariance under the combined CPT transformation we need the mass and integrated lifetime of the B_q^0 and its antiparticle, $\bar{B}_q^0$, to be equal, so, the diagonal elements of H are the same. As a consequence, $M_{11} = M_{22} \equiv M$,

and $\Gamma_{11} = \Gamma_{22} \equiv \Gamma$. Hence, the mass eigenstates of the Hamiltonian are mixtures of the flavor eigenstates shown in 1.9, they are characterized by their masses, and then defined as the heavy, B_H, and light, B_L, states:

$$|B_L >= p|B_q > +q|\overline{B_q} > \qquad |B_H >= p|B_q > -q|\overline{B_q} > \tag{1.12}$$

The normalization condition is

$$|p|^2 + |q|^2 = 1. \tag{1.13}$$

and the eigenvalues of $|B_{H,L} >$, $\omega_{H,L}$, can be found by solving the characteristic equation:

$$|H - I| = 0. \tag{1.14}$$

where I is the 2x2 identity matrix and H is the Hamiltonian defined in Equation 1.11. So that, the eigenvalues are:

$$\begin{aligned}\omega_{H,L} = M - \frac{i}{2}\Gamma \pm \sqrt{\left(M_{12} - \frac{i}{2}\Gamma_{12}\right)\left(M_{12}^* - \frac{i}{2}\Gamma_{12}^*\right)} = \\ = (M \pm \frac{\Delta M}{2}) - \frac{i}{2}(\Gamma \pm \frac{\Delta\Gamma}{2}) = M_{H,L} - \frac{i}{2}\Gamma_{H,L}\end{aligned} \tag{1.15}$$

where $M_{H,L}$ are the masses of the two eigenstates, and $\Gamma_{H,L}$ are the widths. The difference in the masses and widths are $\Delta M = M_H - M_L$, and $\Delta\Gamma = \Gamma_H - \Gamma_L$.

Solving the eigenvalues problem for H yields the relation between p and q in Equation 1.12:

$$\frac{q}{p} = \sqrt{\frac{M_{12}^* - \frac{i}{2}\Gamma_{12}^*}{M_{12} - \frac{i}{2}\Gamma_{12}}} = \frac{\Delta M - i\frac{\Delta\Gamma}{2}}{2(M_{12} - \frac{i}{2}\Gamma)} \tag{1.16}$$

The time evolution of the mass eigenstates B_H ad B_L can be written as:

$$|B_H(t)>= e^{-i(M_H-\frac{i}{2}\Gamma_H)t}(p|B_q>-q|\bar{B}_q>)$$

$$|B_L(t)>= e^{-i(M_L-\frac{i}{2}\Gamma_L)t}(p|B_q>+q|\bar{B}_q>) \tag{1.17}$$

and, from Equation 1.12, the relation between the flavor and mass eigenstates is given by:

$$|B_q>= \frac{1}{2p}\left[|B_H>+|B_L>\right]$$

$$|\bar{B}_q>= \frac{1}{2q}\left[-|B_H>+|B_L>\right] \tag{1.18}$$

So that, the evolution of the initial particle ad anti-particle states of definite flavor, B_q and $\bar{B}_q$ can be described by Equation 1.19 as follows:

$$|B_q(t)>= \frac{1}{2p}[e^{-i(M_H-\frac{i}{2}\Gamma_H)t}(p|B_q>-q|\bar{B}_q>)+e^{-i(M_L-\frac{i}{2}\Gamma_L)t}(p|B_q>+q|\bar{B}_q>)]$$

$$|\bar{B}_q(t)>= \frac{1}{2q}[-e^{-i(M_H-\frac{i}{2}\Gamma_H)t}(p|B_q>-q|\bar{B}_q>)+e^{-i(M_L-\frac{i}{2}\Gamma_L)t}(p|B_q>+q|\bar{B}_q>)] \tag{1.19}$$

Then we can simplify those equations just defining the $g_{\pm}(t)$ function, which includes all the non-constant time related parts:

$$g_{\pm}(t) = \frac{1}{2}[e^{-i(M_H-\frac{i}{2}\Gamma_H)t} \pm e^{-i(M_L-\frac{i}{2}\Gamma_L)t}] \tag{1.20}$$

As a result we can write Equation 1.19 as follows:

$$|B_q(t)>= g_+(t)|B_q> + g_-(t)\frac{q}{p}|\bar{B}_q>$$
$$|\bar{B}_q(t)>= g_-(t)\frac{p}{q}|B_q> + g_+(t)|\bar{B}_q> \tag{1.21}$$

Using these equations it is possible to write the probabilities for finding a B_q or a $\bar{B}_q$, given the initial state, B_q, after a time t :

$$|<B_q|B_q(t)>|^2 = |g_+(t)|^2$$
$$|<\bar{B}_q|B_q(t)>|^2 = |g_-(t)\frac{q}{p}|^2 \tag{1.22}$$

and for an initial $\bar{B}_q$, after a time t :

$$|<B_q|\bar{B}_q(t)>|^2 = |g_-(t)\frac{p}{q}|^2$$
$$|<\bar{B}_q|\bar{B}_q(t)>|^2 = |g_+(t)|^2 \tag{1.23}$$

Hence, the flavor states B_q and $\bar{B}_q$ remain unchanged over time, or oscillate into each other, with a time-dependent probability proportional to $|g_+(t)|^2$and $|g_-(t)|^2$ respectively:

$$|g_\pm(t)|^2 = \frac{1}{2}e^{-\bar{\Gamma}t}\left[\cosh\left(\frac{\Delta\Gamma}{2}t\right) \pm \cos\left(\Delta M t\right)\right] \tag{1.24}$$

where $\bar{\Gamma} = (\Gamma_H + \Gamma_L)/2$.

Observing both B_q^0 and $\bar{B}_q^0$ decays, what we see is that they can have different differential life times. In the B_d^0 meson case, channels common to both B_d^0 and $\bar{B}_d^0$ are favored in terms of the CKM matrix element involved for the

B_d^0 case, but doubly suppressed for the $\bar{B}_d^0$ case, or vice-versa. Anyway, this contribution is not very important, as we know that for the difference is:

$$\frac{\Delta\Gamma_d}{\bar{\Gamma}_d} = \mathcal{O}(10^{-3}) \tag{1.25}$$

Otherwise, for B_s^0 mesons, the lifetime difference is considerably larger. The most recent measurements indicate

$$\frac{\Delta\Gamma_s}{\bar{\Gamma}_s} < 0.54 \tag{1.26}$$

at the 95% confidence level [7].

The oscillation parameter, defined as $x = \frac{\Delta M}{\bar{\Gamma}}$, has been measured for both the B_d^0 and B_s^0 systems[8]:

$$x_d = 0.776 \pm 0.008$$

$$x_s > 19.9 \text{ at the CL } 95\%. \tag{1.27}$$

So that, for both B_d^0 and B_s^0 meson decays $\Delta M \ll \Delta\Gamma$, hence $\Gamma_{12} \ll M_{12}$ and therefore to a good approximation we have:

$$|p| = |q| \tag{1.28}$$

for both B_d^0 and B_s^0 systems.

1.4 Classification of CP-Violating effects

We distinguish three types of CP-violating effects in meson decays:

- CP violation in decay, which occurs in charged meson decays where mixing effects are absent, also known as *direct* CP violation.

- CP violation in mixing, which occurs in charged-current semileptonic neutral meson decays, also known as *indirect* CP violation.
- CP violation in *interference* between a decay without mixing, and a decay with mixing, as occurs only in decays to final states that are common to a neutral meson and to his antiparticle, including all CP eigenstates.

1.4.1 *Direct* CP violation.

When the amplitude for a decay and its CP conjugate process have different magnitudes, can occur, due to CP-violating interference between terms in the decay amplitude, a CP violation in the decay. Because of it we will observe a difference between the rate for $B_q \to f$ and the CP conjugate process $\bar{B_q} \to \bar{f}$. If the decay amplitudes are written as $A_f \equiv < f|H_{weak}|B_q >$, and $\bar{A}_{\bar{f}} \equiv < \bar{f}|H_{weak}|\bar{B_q} >$, then

$$A_f = \sum_i A_i e^{i\phi_i} e^{i\delta_i}, \quad \bar{A}_{\bar{f}} = \sum_i A_i e^{-i\phi_i} e^{i\delta_i} \tag{1.29}$$

where the two types of phases in the amplitudes are ϕ_i, the weak phases, and δ_i, the strong phases.

The weak phases are the phases which occur in the CKM matrix, and hence are due to complex parameters in the Lagrangian of the weak interaction. These appear in complex conjugate form in the CP conjugate amplitude, so with a different sign in A_f and $\bar{A}_{\bar{f}}$.

The strong phases are due to final state interactions, in scattering or decay amplitudes, even when the Lagrangian is real. Since they appear in A_f and $\bar{A}_{\bar{f}}$ with the same sign, they do not violate CP.

When CP is conserved, all the weak phases are equal, $\phi_i = \phi_j$, and so

$$\left| \frac{\bar{A}_{\bar{f}}}{A_f} \right| = 1 \tag{1.30}$$

Otherwise, if it is possible for the meson to decay by several mechanisms with different amplitudes and, above all, with different weak and strong phases, interference between the decay amplitudes causes a difference in the rates for $B_q \to f$ and $\bar{B_q} \to \bar{f}$. Then,

$$\left| \frac{\bar{A}_{\bar{f}}}{A_f} \right| \neq 1 \tag{1.31}$$

and this is the condition that defines CP Violation in decay. This type of CP Violation has been easily measured from the decays of charged mesons, where mixing is not possible. Historically, the decay of K mesons provided the first experimental evidence[8] of CP-Violation[3]. Several charged B decays will be studied at LHCb[9], most notably $B^{\pm} \to DK^{\pm}$.

1.4.2 *Indirect* CP violation

CP violation in the mixing occurs when the mass eigenstates are not CP eigenstates, and so, when CP violation enters the time evolution described by the Schrödinger equation. As before, this implies a difference in the rates $B_q \to \bar{B}_q$ and $\bar{B}_q \to B_q$, which requires the magnitude of the off-diagonal elements of the Hamiltonian to be different:

$$\left| M_{12} - \frac{i}{2}\Gamma_{12} \right| \neq \left| M_{12}^{*} - \frac{i}{2}\Gamma_{12}^{*} \right| \tag{1.32}$$

due to a phase difference between M_{12} and Γ_{12}. From Equation 1.16, we easily understand the condition that defines CP violation in the mixing:

$$\left| \frac{q}{p} \right| \neq 1 \tag{1.33}$$

An interesting example of CP violation in the mixing could be the $D^0 - \bar{D}^0$ mixing. It has not yet observed, but, by itself, it can provide a relevant prove of new physics. Within the Standard Model, indeed, the CP-violating effects are predicted to be negligibly small, since the mixing and the relevant decays are described, to an excellent approximation, by physics of the first two generations[9]. Observation of CP violation in $D^0 - \bar{D}^0$ mixing (at a level much higher than $\mathcal{O}(10^{-3})$) will constitute an unambiguous signal of new physics. At present, the most sensitive searches involve the $D \to K^{\pm}\pi^{\pm}$ and $D \to K^{+}K^{-}$ modes.

[8] CP violation was discovered for the first time in $K \to \pi\pi$ decays in 1964.

[9] For the B meson system, both B_d^0 and B_s^0, experimental measurements indicate that $\Gamma_{12} \ll M_{12}$ is a good approximation, and hence $|p| = |q|$. Therefore CP violation in the mixing of B mesons is expected to be a small effect, with the parameter $1 - \left|\frac{q}{p}\right|^2$ of order (10^{-3}) for the B_d^0 system and (10^{-4}) for the B_s^0 system [7].

1.4.3 CP violation in *interference* of mixing and decay.

This third type of CP violation is potentially the most interesting for the neutral B meson system. When a B_q^0 and $\bar{B}_q^0$ can both decay to the same final state, f, then CP violation can occur as a result of interplay between the mixing and decay amplitudes. By calculating these decay rates and mixing amplitudes, then observing them experimentally, it is possible to measure the free theoretical parameters in the CKM matrix.

Starting from Equation 1.21, we can write the decay amplitude for a neutral B_q meson decaying to a final state f, $B_q \to f$:

$$< f|H_{weak}|B_q(t) >= g_+(t) < f|H_{weak}|B_q > + \frac{q}{p} g_-(t) < f|H_{weak}|\bar{B}_q > \quad (1.34)$$

where H_{weak} is the Hamiltonian of the weak interaction, $< f|H_{weak}|B_q >$ and $< f|H_{weak}|\bar{B}_q >$ are time-independent amplitudes. Similarly we can write the decay amplitude for a neutral $\bar{B}_q$ meson decaying to a final state f, $\bar{B}_q \to f$:

$$\begin{aligned} < f|H_{weak}|\bar{B}_q(t) >= g_-(t)\frac{p}{q} < f|H_{weak}|B_q > + g_+(t) < f|H_{weak}|\bar{B}_q >= \\ = \frac{p}{q}\left(g_-(t) < f|H_{weak}|B_q > + g_+(t)\frac{q}{p} < f|H_{weak}|\bar{B}_q > \right) \end{aligned} \quad (1.35)$$

Now let's define:

$$\begin{aligned} A_f &\equiv < f|H_{weak}|B_q > \quad & \bar{A}_f &\equiv < f|H_{weak}|\bar{B}_q > \\ A_{\bar{f}} &\equiv < \bar{f}|H_{weak}|B_q > \quad & \bar{A}_{\bar{f}} &\equiv < \bar{f}|H_{weak}|\bar{B}_q > \end{aligned} \quad (1.36)$$

we can write the Equation 1.21 as follows (just for the first case as example):

$$< f|H_{weak}|B_q(t) >= A_f \left(1 + \frac{q}{p}\frac{\bar{A}_f}{A_f}\right) e^{-iM_L t} e^{-i\Gamma_L t} + A_f \left(1 - \frac{q}{p}\frac{\bar{A}_f}{A_f}\right) e^{-iM_H t} e^{-i\Gamma_H t} \quad (1.37)$$

Then, we know that the decay rate for $B_q \to f$ is proportional to the squared matrix element $| < f|H_{weak}|B_q(t) > |^2$ and similarly the decay rate for $\bar{B}_q \to f$ is proportional to the squared matrix element $| < f|H_{weak}|\bar{B}_q(t) > |^2$; the same condition can be extended to the decays $B_q \to \bar{f}$, and $\bar{B}_q \to \bar{f}$, where $\bar{f}$ is the

CP conjugate state to f. Now, by defining the quantities

$$\eta \equiv \frac{q}{p}\frac{\bar{A}_f}{A_f}, \quad \bar{\eta} \equiv \frac{p}{q}\frac{A_{\bar{f}}}{\bar{A}_{\bar{f}}} \tag{1.38}$$

and then, to simplify the expressions, the functions

$$\begin{aligned}
I_+(t) &= (1+|\eta|^2)\cosh\left(\frac{\Delta\Gamma t}{2}\right) + 2Re(\eta)\sinh\left(\frac{\Delta\Gamma t}{2}\right) \\
I_-(t) &= (1-|\eta|^2)\cos(\Delta M t) - 2\sin(\Delta M t)Im(\eta) \\
\bar{I}_+(t) &= (1+|\bar{\eta}|^2)\cosh\left(\frac{\Delta\Gamma t}{2}\right) + 2Re(\bar{\eta})\sinh\left(\frac{\Delta\Gamma t}{2}\right) \\
\bar{I}_-(t) &= (1-|\bar{\eta}|^2)\cos(\Delta M t) - 2\sin(\Delta M t)Im(\bar{\eta})
\end{aligned} \tag{1.39}$$

we can write, neglecting the phase-space factor and some constants, the decay rates for all the given cases:

$$B_q \to f: \quad r_f(t) \quad \propto \quad \frac{1}{2}e^{-\bar{\Gamma}t}|A_f|^2\left[I_+(t)+I_-(t)\right] \tag{1.40}$$

$$\bar{B}_q \to f: \quad r_{\bar{f}}(t) \quad \propto \quad \frac{1}{2}e^{-\bar{\Gamma}t}\left|\frac{p}{q}\right|^2|A_f|^2\left[I_+(t)-I_-(t)\right] \tag{1.41}$$

$$\bar{B}_q \to \bar{f}: \quad \bar{r}_{\bar{f}}(t) \quad \propto \quad \frac{1}{2}e^{-\bar{\Gamma}t}|\bar{A}_{\bar{f}}|^2\left[\bar{I}_+(t)+\bar{I}_-(t)\right] \tag{1.42}$$

$$B_q \to \bar{f}: \quad r_{\bar{f}}(t) \quad \propto \quad \frac{1}{2}e^{-\bar{\Gamma}t}\left|\frac{q}{p}\right|^2|\bar{A}_{\bar{f}}|^2\left[\bar{I}_+(t)-\bar{I}_-(t)\right] \tag{1.43}$$

For the B_d and B_s meson systems, to a good approximation, $|q/p| = 1$, so we don't expect significant CP violation in the mixing. Then, if $|\bar{A}_f/A_f| = 1$ as well, CP is conserved both, in the mixing and the decay. The complex ratios η and $\bar{\eta}$, defined in Equation 1.36, are independent of phase convention, and physically meaningful for describing the CP violating effects. The condition

$$\eta \neq \pm 1 \tag{1.44}$$

defines CP violation in the interference between mixing and decay[10], but it is possible to have CP violation in the interference between mixing and decay also when $|\eta| = 1$, but $Im(\eta) \neq 0$, so that η is a pure phase. At present this is the most theoretically clean situation for extracting the values of the CKM parameters from experimental measurements.

A useful way to estimate CP violation, from the time-dependent decay rates of neutral B_q^0 and $\bar{B_q^0}$ mesons, to the same final state f and its CP conjugate state $\bar{f}$, is to use the time-dependent decay rate asymmetries $\mathcal{A}_{\mathcal{CP}}$ and $\overline{\mathcal{A}}_{\overline{\mathcal{CP}}}$, defined as functions of the decay rates given in Equations 1.40, 1.41, 1.42 and 1.43:

$$\mathcal{A}_{\mathcal{CP}} = \frac{r_f(t) - \bar{r}_f(t)}{r_f(t) + \bar{r}_f(t)} \quad \overline{\mathcal{A}}_{\overline{\mathcal{CP}}} = \frac{\bar{r}_{\bar{f}}(t) - r_{\bar{f}}(t)}{\bar{r}_{\bar{f}}(t) + r_{\bar{f}}(t)} \tag{1.45}$$

Now we know that for the decays of B mesons we can use the approximation $|p| = |q|$, so that the 1.45 can be written in a simpler way using the expressions for $I_-(t)$, $I_+(t)$, $\bar{I}_-(t)$ and $\bar{I}_+(t)$ given before:

$$\mathcal{A}_{\mathcal{CP}} = \frac{I_-(t)}{I_+(t)} = \frac{(1 - |\eta|^2)\cos(\Delta M t) - 2\sin(\Delta M t) Im(\eta)}{(1 + |\eta|^2)\cosh\left(\frac{\Delta\Gamma t}{2}\right) + 2Re(\eta)\sinh\left(\frac{\Delta\Gamma t}{2}\right)} \tag{1.46}$$

$$\overline{\mathcal{A}}_{\overline{\mathcal{CP}}} = \frac{\bar{I}_-(t)}{\bar{I}_+(t)} = \frac{(1 - |\bar{\eta}|^2)\cos(\Delta M t) - 2\sin(\Delta M t) Im(\bar{\eta})}{(1 + |\bar{\eta}|^2)\cosh\left(\frac{\Delta\Gamma t}{2}\right) + 2Re(\bar{\eta})\sinh\left(\frac{\Delta\Gamma t}{2}\right)} \tag{1.47}$$

In the next section we will discuss the application of this equation finalized to extract the angles of the unitary triangles.

1.5 CKM-Parameters calculation and important decays

As written in section 1.2, the Wolfenstein parametrization is based on the 4 parameters, A, λ, ρ, and η. The two unitary triangles in Figures 1.1 and 1.2 are determined by ρ and η, since the value of λ is well known, and the parameter A can be extracted from measurements of λ and $|V_{cb}|$.

[10]The existence of CP violation in the mixing or CP violation in the decay is sufficient to satisfy 1.44, since $|\eta| \neq 1$.

The two parameters ρ and η can be derived from the $|V_{ub}|$, $|V_{cb}|$, $|V_{td}|$ and $|V_{ts}|$ matrix elements. The values of $|V_{ub}|$ and $|V_{cb}|$ can be determined from B meson decays generated by tree diagrams; $|V_{td}|$ and $|V_{ts}|$ can be calculated from $B_s^0 - \overline{B_s^0}$ and $B_d^0 - \overline{B_d^0}$ oscillation frequency[11]. Once the ρ and η parameters are derived from the mixing matrix elements, the angles α, β, γ and $\gamma\delta$ in the two unitary triangles considered can be calculated indirectly [10]. On the other side direct measurements of those angles can be done in the Standard Model framework from CP asymmetry in different final states of B meson decays, a possible way is[12]:

- α from $B_d^0 \to \pi^+\pi^-$
- β from $B_d^0 \to J/\Psi K_s^0$
- γ from $B_s^0 \to D_s^{\pm} K^{\mp}$
- $\delta\gamma$ from $B_s^0 \to J/\Psi\Phi$

1.5.1 $B_d^0 \to \pi^+\pi^-$

The $B_d^0 \to \pi^+\pi^-$ decay, shown in Figure 1.4, allows us to determine the α angle of the first unitary triangle. The final state is generated by the $b \to u$ tree diagram and by the small but not negligible $b \to d$ penguin diagram.

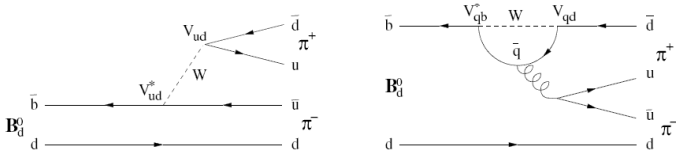

Figure 1.4: The tree level diagram for $B_d^0 \to \pi^+\pi^-$ decay (left) and its leading penguin contributions (right), where $\bar{q}$ can be a $\bar{t}$, $\bar{c}$, or $\bar{u}$ quark.

[11] At present the $B_d^0 - \overline{B_d^0}$ oscillation is well measured, while only a lower limit is known for the $B_s^0 - \overline{B_s^0}$ oscillation frequency.

[12] If a new flavor-changing neutral current is introduced, it can have a large effect on the neutral B mesons oscillation and the values of $|V_{td}|$ and $|V_{ts}|$ experimentally extracted would no longer correspond to their real values. Moreover the angles extracted from the considered decays would be affected.

Let's consider that the decay is governed only by the first (left) diagram in Figure 1.4. With reference to Equation 1.8, the phase of each CKM element, which contribute at each vertex, is zero, and the corresponding leading order penguin diagram, has the same overall phase[13]. As a result there is no CP-violation in the decay, $|A_F/\bar{A}_F| = 1$, hence $|\eta| = 1$, and also the term proportional to $\cos(\Delta M t)$ vanishes. Therefore although $|q| = |p|$ is a good approximation, and hence CP violation in the mixing is not significant, CP violation can occur in the interference between mixing and decay. So, for this decay, the parameter η, defined in Equation 1.38, is the phase difference between the two interfering decay paths:

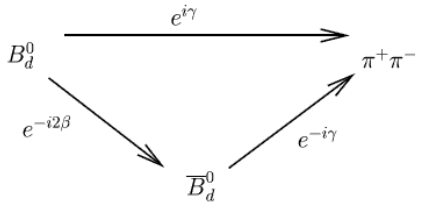

Figure 1.5: The two different decay paths and their phases in the $B_d^0 \to \pi^+\pi^-$ decay.

$$\eta = \frac{q}{p}\frac{\bar{A}_f}{A_f} = \frac{q}{p}(1) = e^{-2i(\beta+\gamma)} \tag{1.48}$$

Now, in this case[14], from Equation 1.46, the measurable asymmetry can be written as follows:

$$\mathcal{A}_{\mathcal{CP}} = -\sin(\Delta M t)\sin(2(\beta+\gamma)). \tag{1.49}$$

Unfortunately, the contribution from the penguin diagram in Figure 1.4 (right) is not negligible. The penguin pollution introduces a strong phase factor making the relation to the unitary triangle more difficult. What we will observe is a CP violation in the decay, meaning that the decay rates for $B_d^0 \to \pi^+\pi^-$

[13]The non-zero phase, and therefore CP-violating, contribution from the $b \to u$ transition is negligible, as it is both doubly Cabibbo suppressed and loop mass suppressed.

[14]In the B_d^0 system, $\Delta\Gamma$ is small, so some terms in the expression for the asymmetry can be neglected.

and $\bar{B}^0_d \to \pi^+\pi^-$ are different. Due to this, $A_F/\bar{A}_F \neq 1$, so Equation 1.49 is no longer correct, and there is also a contribution proportional to $\cos(\Delta Mt)$, then the CKM angles β and γ, and hence $\alpha = \pi - \beta - \gamma$, need to be extracted with some additional consideration.

Let's introduce two separate terms, one related to the direct, a^{dir}, and the other one to the interferenced, a^{int}, CP violation, into Equation 1.46 so that in this decay we have:

$$\mathcal{A}_{\mathcal{CP}} = \frac{I_-(t)}{I_+(t)} = a^{int}\left(\Delta Mt\right) - a^{dir}\cos\left(\Delta Mt\right) \tag{1.50}$$

where

$$a^{int} = \frac{2Im(\eta)}{1+|\eta|^2} \tag{1.51}$$

and

$$a^{dir} = \frac{1-|\eta|^2}{1+|\eta|^2} \tag{1.52}$$

Now we can re-express Equations 1.51 and 1.52 in terms of the penguin, P, and tree contribution, T, to relate them to the α angle as follows:

$$a^{int} = \sin(2\alpha) + 2\left|\frac{P}{T}\right|\cos(\delta_{P/T})\cos(2\alpha)\sin\alpha \tag{1.53}$$

$$a^{dir} = 2\left|\frac{P}{T}\right|\sin(\delta_{P/T})\sin\alpha \tag{1.54}$$

where $\delta_{P/T}$ is the difference between the strong phases of the penguin pollution and the tree contribution.

1.5.2 $B^0_d \to J/\Psi K^0_s$

The $B^0_d \to J/\Psi K^0_s$ decay is the so called 'golden channel[15]' and allows us the measurement of the CP violating parameter β. This decay is dominated by its tree level diagram, so we can apply all the considerations given for the previous

[15]This is the most tested channel from the BaBar a Belle B-factories.

case in paragraph 1.5.1.

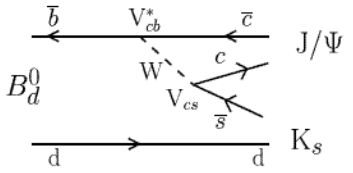

Figure 1.6: Tree-level diagram for the $B^0_d \to J/\Psi K^0_s$ decay

Also here the phase of each CKM element is zero, contribution from the $b \to u$ transition is negligible, there is no CP-violation in the decay, $|A_f/\bar{A}_f| = 1$, $|\eta| = 1$, and the term proportional to $\cos(\Delta M t)$ vanishes too. We remember that $|q| = |p|$ with good approximation, so CP violation in the mixing is also negligible. The source of CP violation is in the interference with $B^0 - \bar{B}^0$ and $K^0 - \bar{K}^0$mixing and decay. η is then calculated, as in Equation 1.48, as phase difference between the two interfering decay paths, but here, because $J/\Psi K^0_s$ is a CP-odd state, $\frac{\bar{A}_f}{A_f} = -1$, we have a negative η:

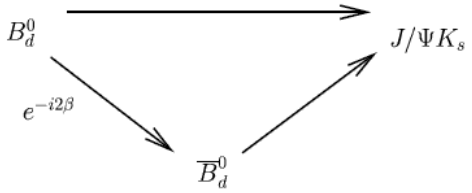

Figure 1.7: The two different decay paths and the phase difference in the $B^0_d \to J/\Psi K^0_s$ decay.

$$\eta = \frac{q}{p}\frac{\bar{A}_f}{A_f} = \frac{q}{p}(-1) = -e^{-2i\beta} \tag{1.55}$$

After all those considerations, Equation 1.46 becomes simpler, and the measurable asymmetry can be written as follows:

$$\mathcal{A}_{\mathcal{CP}} = -\sin(\Delta M t)\sin(2\beta). \tag{1.56}$$

Finally, the experimentally measurable asymmetry given in Equation 1.56 gives us the needed relation with β.

1.5.3 $B_s^0 \to D_s^- K^+$

The $B_s^0 \to D_s^- K^+$ decay, similarly to the previous case, has no Penguin pollution, but presents two crucial differences. First of all, both the B_s^0 and $\bar{B_s^0}$ can decay to the same final state via tree diagrams with a phase difference of $-\gamma$. The second issue is that $D_s^- K^+$ is not a CP eigenstate and there is a CP conserving contribution Δ_S due to the strong interaction.

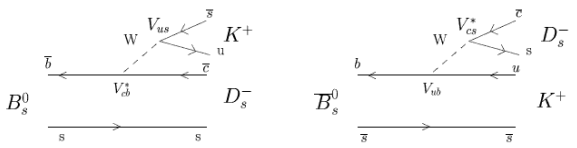

Figure 1.8: Tree-level diagrams for $B_s^0 \to D_s^- K^+$and $\bar{B_s^0} \to D_s^- K^+$decays.

The only contribution from CP violation in the interference between mixing and decay, leads to a overall phase difference, Δ_{CP}, of $-\gamma + 2\delta\gamma$, but, since $D_S K$ is not a CP-eigenstate, the overall phase difference is not simply equal to η, so that η and $\bar{\eta}$ have to be written considering Δ_S:

$$\eta = |\eta| e^{i(\Delta_{CP} + \Delta_S)}$$

$$\bar{\eta} = |\overline{\eta}| e^{i(-\Delta_{CP} + \Delta_S)} \tag{1.57}$$

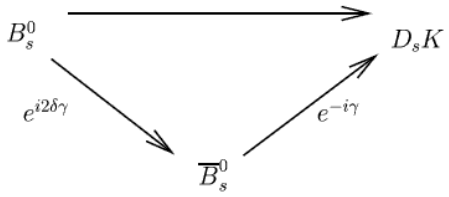

Figure 1.9: The two different decay paths and the phase differences in the $B_s^0 \to D_s^- K^+$ decay.

For the B_s^0 system the assumption $\Delta\Gamma \sim 0$, made for the B_d^0 system, is no longer valid, so the Equations 1.46 and 1.47 remains complicated as well, without any further simplification. The final measurement of γ comes out measuring both time-dependent asymmetries, $\mathcal{A}_{\mathcal{CP}}$ and $\bar{\mathcal{A}}_{\bar{\mathcal{CP}}}$, hence on a good evaluation of the B_s oscillation parameter, and is strictly depending on the value of the strong phase ,Δ_S , as well as the B_s mixing angle, $2\delta\gamma$, that will also be measured from $B_s^0 \to J/\Psi\Phi$, allowing to further constrain the angle γ.

1.5.4 $B_s^0 \to J/\Psi\Phi$,

The $B_s^0 \to J/\Psi\Phi$ decay is dominated by its tree level diagram and has no penguin pollution. The crucial point here is the separation of the two mixed CP eigenstates in its final state, and it can be performed trough an angular analysis of the decay products of the J/Ψ and Φ [11].

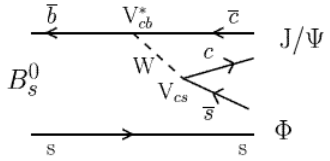

Figure 1.10: Tree-level diagrams for $B_s^0 \to J/\Psi\Phi$ decay.

Similarly to the $B_d^0 \to J/\Psi K_s^0$ decay, the overall phase of the CKM matrix elements which contribute to each vertex is zero, and the non-zero phase enters in the interference between mixing and decay, but here we need to introduce the parameter *r,* the ratio of the decay amplitudes to the CP-even and CP-odd states. Now can write η as follows:

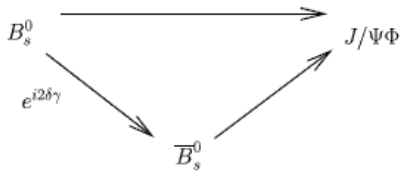

Figure 1.11: The two different decay paths and the phase difference in the $B_s^0 \to J/\Psi\Phi$ decay.

$$\eta = \frac{q}{p}\frac{\bar{A}_f}{A_f} = \frac{q}{p}(1) = \frac{1-r}{1+r}e^{2i\delta\gamma} \tag{1.58}$$

As said before, for the B_s^0 system, referring to Equation 1.46, further simplification are not allowed, so, for a good measurement of $\delta\gamma$, it will be needed a full characterization of B_s^0 mixing, measuring ΔM and $\Delta\Gamma$, that has not been possible in the B-factories yet, but will be in the next years at the LHCb experiment.

1.5.5 Global fit in the Standard Model

Here is a summary of the channels used to have the most precise determination of each element of the CKM matrix:

- $|V_{ud}|$ is measured from nuclear beta decays.
- $|V_{us}|$ comes from leptonic and semileptonic kaon, hyperon and τ decays.
- $|V_{cd}|$ can be extracted from semileptonic charm decays.
- $|V_{cs}|$can be determined from semileptonic D or leptonic D_s decays.
- $|V_{cb}|$can be obtained from exclusive and inclusive semileptonic decays of B mesons to charm.
- $|V_{ub}|$comes from inclusive $B \to X_u l\bar{\nu}$ or from exclusive $B \to \pi_u l\bar{\nu}$ decay.
- $|V_{td}|$ and $|V_{ts}|$ can be determined only from $B^0 - \bar{B}^0$ oscillations mediated by box diagrams or via loop-mediated rare K and B decays.

- $|V_{tb}|$ can be measured directly from top decays ($t \to Wb$, $t \to Wq$).

and this is the experimental status of the CKM matrix at the present moment[12]:

$$\begin{pmatrix} |V_{ud}| & |V_{us}| & |V_{ub}| \\ |V_{cd}| & |V_{cs}| & |V_{cb}| \\ |V_{td}| & |V_{ts}| & |V_{tb}| \end{pmatrix} = \begin{pmatrix} 0.97383^{+0.00024}_{-0.00023} & 0.2272^{+0.00010}_{-0.00010} & 0.00396^{+0.00009}_{-0.00009} \\ 0.2271^{+0.0010}_{-0.0010} & 0.97296^{+0.00024}_{-0.00024} & 0.04221^{+0.00010}_{-0.00080} \\ 0.00814^{+0.00032}_{-0.00064} & 0.04161^{+0.00012}_{-0.00078} & 0.999100^{+0.000034}_{-0.000004} \end{pmatrix} \tag{1.59}$$

Here are summarized the most recent values on the unitary triangle angles:

- $\alpha = 93.1^{\circ}{}^{+9.9}_{-12.5}$
- $\beta = 23.1^{\circ}{}^{+1.5}_{-1.5}$
- $\gamma = 58.2^{\circ}{}^{+6.7}_{-5.4}$

The sum of the three angles $\alpha + \beta + \gamma$, considering the uncertainties on them, is what do we expect from a triangle, and is also consistent with the Standard Model expectations.

1.6 Decay reconstruction method.

In $B^0 - \bar{B^0}$ system B mesons are produced as $b\bar{b}$ pairs. One of the two mesons decays, B_{event}, is completely reconstructed while the other, B_{tag}, is used to tag the flavor. This tagging of the selected B^0 in the decay of interest is achieved by estimating its flavor at production from the decay products of the other B meson in the event. Flavor tagging is principally based on charge correlations of daughter particles with the flavor of the decaying B_{tag}. The flavor can, for example, be determined if the other B meson decayed semi-leptonically, from the charge of the lepton. Alternatively, the tagging of the reconstructed B^0 can be carried out using its own decay products. Unfortunately, the tagging is never perfect and the observable asymmetry will be always smaller than the true asymmetry. The probability of an incorrect experimental identification is called mistag fraction. In addition, if the tag is based on the flavor of the other B meson, and it is a neutral B meson which may oscillate before decaying, this will contribute to the mistag fraction.

Let's consider $\mathcal{A}_{\mathcal{CP}_{\text{true}}}$, the real asymmetry in the system, similarly to Equation 1.45 we can define N as the number of b produced and $\bar{N}$ as the number of $\bar{b}$ produced, so that we have:

$$\mathcal{A}_{\mathcal{CP}_{\text{true}}} = \frac{\bar{N} - N}{\bar{N} + N} \tag{1.60}$$

Introducing now ω, the mistag fraction, we can express the experimental asymmetry measurement by Equation 1.61:

$$\mathcal{A}_{\mathcal{CP}_{\text{meas}}} = \frac{\bar{N}(1-\omega) + N\omega - (\bar{N}\omega + N(1-\omega))}{\bar{N} + N} = (1-2\omega)\frac{\bar{N} - N}{\bar{N} + N} \tag{1.61}$$

Calling D the dilution term, we have the following relation between $\mathcal{A}_{\mathcal{CP}_{\text{meas}}}$ and $\mathcal{A}_{\mathcal{CP}_{\text{true}}}$:

$$\mathcal{A}_{\mathcal{CP}_{\text{meas}}} = (1-2\omega)\mathcal{A}_{\mathcal{CP}_{\text{true}}} = D\mathcal{A}_{\mathcal{CP}_{\text{true}}} \tag{1.62}$$

A perfect tagging gives $D = 1$, while random tagging ($\omega = 50\%$) gives D = 0, while a negative dilution means that the flavor tagger anti-tags the b. This dilution decreases the measured oscillation amplitude to find $\sin 2\beta$ and ΔM_{B_d}. An accurate measurement of the mistag fraction is crucial to control the systematic error in the measurement of the true asymmetry, also because it has a different source, unlike resolution effects such as background or the finite proper time resolution of the detector, that will be described in the next chapter.

Chapter 2

LHCb Experiment at LHC

Introduction

The Large Hadron Collider beauty experiment (LHCb) is aimed to study CP violation and rare decays in the B-system as a consequence of proton-proton collisions. The LHCb detector will use the Large Hadron Collider[13] (LHC), a new accelerator under construction at CERN in the underground tunnel previously occupied by LEP.

There are four[1] main experiments at the LHC, ATLAS, CMS, ALICE and LHCb, located at each of the four interaction points (IP1, IP2, IP5, IP8) (Fig. 2.1), where the beams cross over to the other beam pipe and collide under a small angle.

ATLAS[14] and CMS[15] are general-purpose central detectors, their main physics goals are the search for the Higgs boson and for SUSY particles.

ALICE[16] will focus on studying the quark-gluon plasma in dedicated runs for heavy ions collisions (Pb-Pb, Ca-Ca).

LHCb[17] is centered on the study of b-quark physics, and, using the center-of-mass energy provided by LHC at a reduced (by approximately 2 order of magnitude) luminosity, it will be able to extend the scope of the existing measurements from the BaBar and Belle experiments. Indeed, while the former are only analyzing B_d and B_u decay modes, LHCb will measure a wider range of b-hadron decays, including B_s mesons and Λ_b baryons (bud). Moreover it will be able to test also the Standard Model to its limits and beyond, probing for new Physics.

[1] A fifth experiment, called TOTEM, will be installed in the same interaction point of CMS: its main goal will be to study very forward QCD processes and to measure the total cross section at LHC, which is very important for the other experiments (e.g. for absolute luminosity measurements).

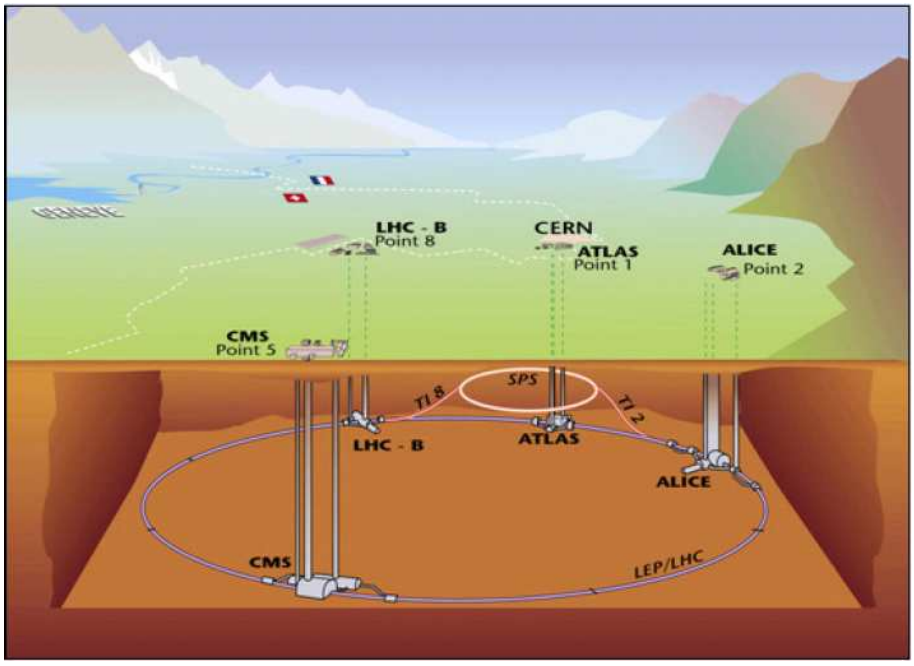

Figure 2.1: The four main experiments at LHC: ATLAS, CMS, ALICE and LHCb.

2.1 LHC and p-p physics

In the summer of 2007 the Large Hadron Collider (LHC) will start his work. LHC is a 27 km circumference high luminosity proton-proton collider with a center-of-mass energy of $\sqrt{s} = 14\ TeV$, by far the most powerful ever built. Right now it's being built in the existing LEP tunnel, from 50 m to 150 m underground.

The protons accelerating process is conducted via several steps: two counter rotating proton beams are accelerated in a LINear ACcelerator (Linac) up to 50 MeV, and then injected in two circular accelerators where they are boosted to 1 GeV (Booster) and 25 GeV (PS). After that the beams enter the Super Proton Synchrotron (SPS) where they reach the energy of 450 GeV, and finally, via two new tunnels, they are injected in the LHC and accelerated up to 7 TeV (see Figure2.2).

The beam moves around the LHC ring inside a continuous ultrahigh-vacuum pipe which pass through a large number of magnets. 1232 superconducting dipole magnets (8.34 T) bend the high momentum beam around the 27 km ring. A huge cryogenic system is required to maintain the liquid helium at the temperature of $1.9°K$, needed to keep the magnets cold. The beams will be stored at high energy for 10 to 20 hours. In 10 hours the particles will make about four hundred million revolutions around the machine, producing several

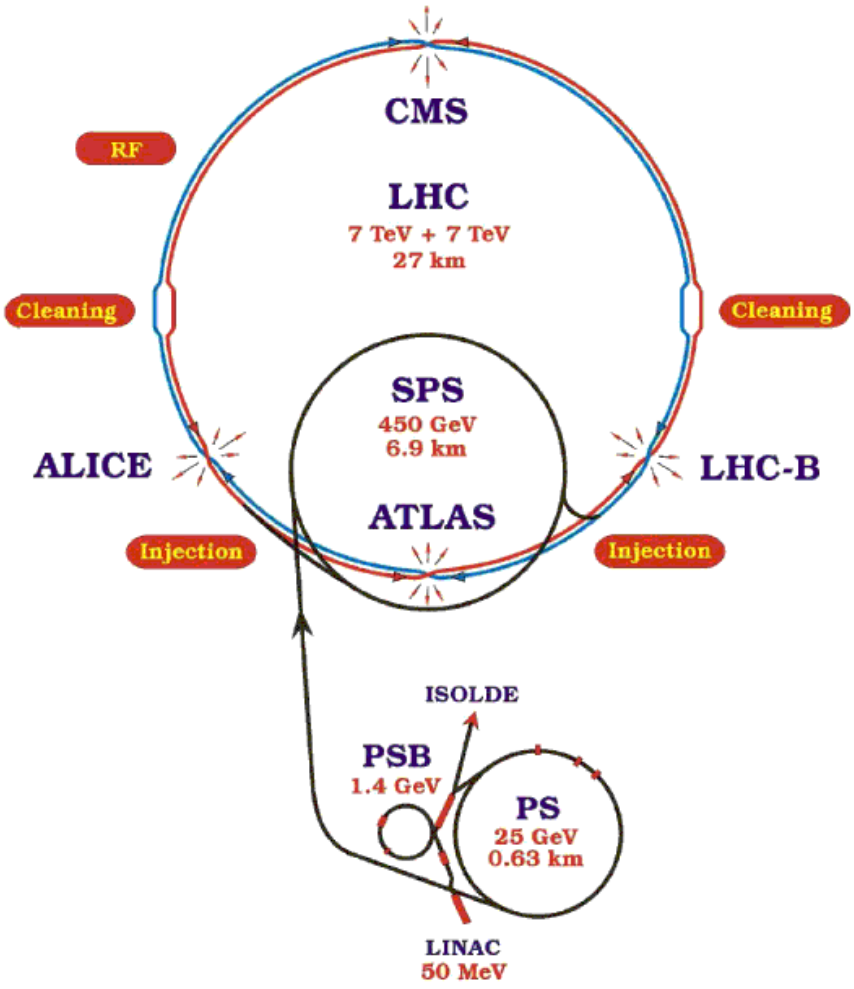

Figure 2.2: Proton accelerating path.

collisions inside the four IP's.

Two consecutive bunch crossings are separated in time by 25 *ns*, which sets the basic clock frequency for the detector electronics to 40 *MHz*. After the commissioning period, in 2007, the LHC will deliver beams for physics with a starting luminosity[2] $\mathcal{L}= 5 \cdot 10^{32} cm^{-2} s^{-1}$ to be progressively increased to its nominal value of $10^{34} cm^{-2} s^{-1}$ over the first three years of operation. The following table resumes the most relevant cross sections available at the LHC.

Cross section type	Cross section (mb)
Total (σ_{tot})	100
Inelastic (σ_{inel})	55
$c\bar{c}$ ($\sigma_{c\bar{c}}$)	3.5
$b\bar{b}$ ($\sigma_{b\bar{b}}$)	0.5
$t\bar{t}$ ($\sigma_{t\bar{t}}$)	$0.8 \cdot 10^{-6}$

Table 2.1: most relevant cross sections available at the LHC.

The inelastic cross section σ_{inel} is extrapolated using UA1, CDF and D$\emptyset$ data[18], but with large uncertainties. The total inelastic cross section defines the average number of interactions per bunch crossing:

$$N_{pp} = \frac{\mathcal{L}\sigma_{inel}}{\nu_{bc}} \tag{2.1}$$

where ν_{bc} is the nominal bunch crossing frequency (40 *MHz*).

Because of the displaced interaction point of LHCb (see Section 2.2), only the 74.3% of bunches will collide[13]. The average bunch crossing rate, therefore, will be 30 *MHz*. Figure 2.3 shows the probabilities to have n=0,..,4 *pp* interactions per bunch crossing as a function of the machine luminosity, where the inelastic *pp* cross-section is assumed to be 55 *mb*.

Compared to events with one *pp* interaction, those with multiple *pp* interactions are more difficult to be reconstructed due to the increased particle density. Therefore, the rejection of pile-up events is essential in order to maximize the number of triggered $b\bar{b}$ events[3].

[2]The machine luminosity is a fundamental parameter for the collider performance, because it determines the number of *pp* collisions at each crossing point. It includes the compactness of the beams, the magnets capability to focus the beams at the interaction point, the number of particles in the bunches and the bunch crossings rate.

[3]Some other important factors influencing the choice of the running luminosity are the radiation damage that may result, and the occupancy of the detectors.

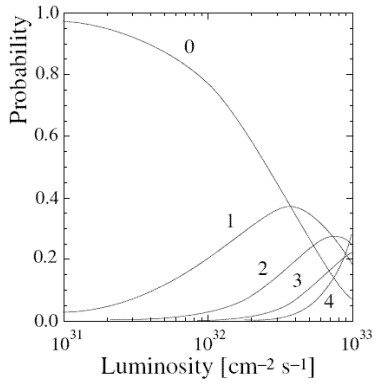

Figure 2.3: Probability for n inelastic collisions per bunch crossing as a function of luminosity.

Taking all these points into account, the average running luminosity of the LHCb experiment has been chosen to be $\mathcal{L}= 2{\cdot}10^{32} cm^{-2} s^{-1}$. At this luminosity there are interactions in 30% of the bunch crossings and the effective bunch crossing rate, with at least one pp interaction, is thus about 10 *MHz*.

The cross section $\sigma_{b\bar{b}}$ will be between 175 and 950 μb[19] depending on the value of the worse known parameters. The value of 500 μb is a mean assumed as a reference by all LHC experiments. It will be known more precisely after the start of LHC.

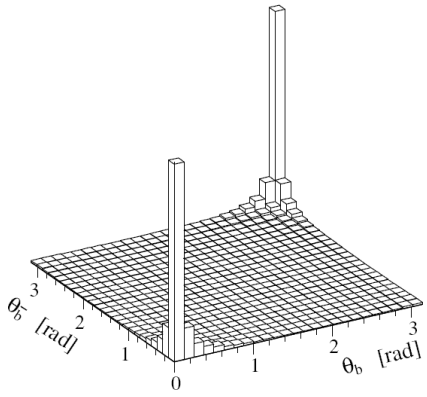

Figure 2.4: Polar angle θ of b and $\bar{b}$ hadron directions.

The dominant $b\bar{b}$ production mechanism in pp collisions is the fusion of two or more gluons radiated from the constituent quarks of the protons. This leads

to an approximately flat distribution in rapidity, and hence, an angular distribution peaked at low polar angles. The directions of the two b-hadrons are very correlated, as shown in Figure 2.4. The two peaks correspond to $b\bar{b}$ pairs flying in either directions of the beam axis. Consequently a dedicated b-physics experiment should cover low polar angles.

2.2 LHCb Detector

The LHCb detector[17], shown in 2.5, was concepted as a single-arm forward spectrometer dedicated to the study of CP violation and other rare phenomena concerning the b quarks. As told before, it is housed in the underground pit located at one of the interaction points (IP8) along the LHC ring.

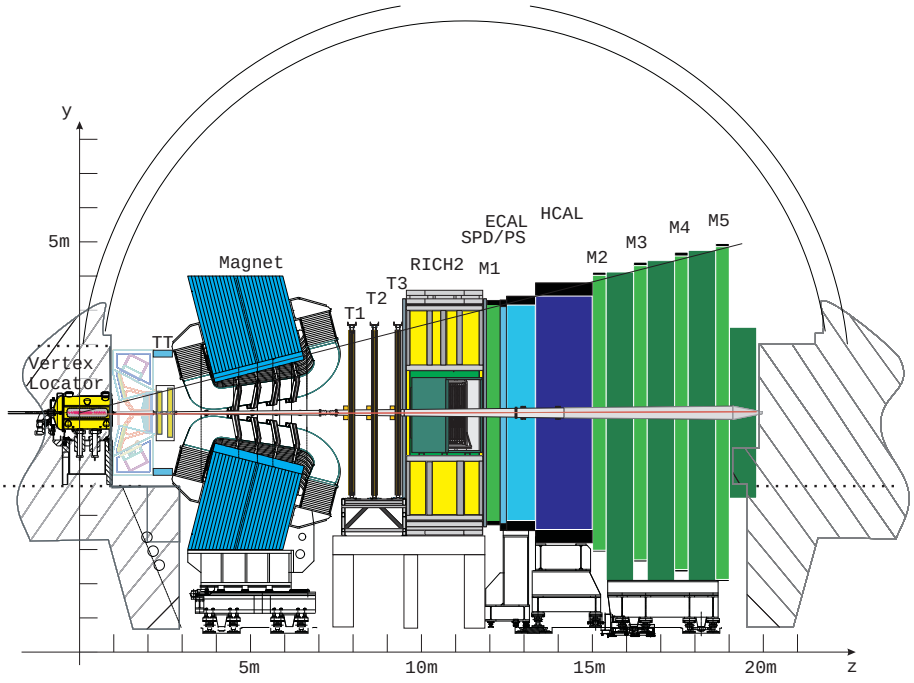

Figure 2.5: The LHCb spectrometer after the re-optimization seen from its bending plane.

To accommodate the spectrometer in the present cavern, without the need for substantial civil engineering work, the beam crossing point has been displaced from the center of the cavern by about 11 m, constraining the total length of the detector to 20 m; the overall dimensions right now are about $6{\times}5{\times}20\ m^3$. Moreover, the acceptance of the detector, defined by the aperture

of the magnet, is 300 *mrad* in the horizontal plane (i.e., the bending plane of the magnet), and 250 *mrad* in the vertical plane (non-bending plane).

A right-handed coordinate system is defined centered on the interaction point, with z along the beam axis and y pointing upwards. The detector design has gone through a number of re-optimization phases. These changes are referred to as the re-optimization[20]. Figure 2.5 shows the re-optimized design of the LHCb detector geometry; one can see, from left to right: vertex locator (VELO), upstream Ring-Imaging Cherenkov detector (RICH1), trigger tracking (TT), magnet, tracking system (T1,T2,T3), downstream Ring-Imaging Cherenkov detector (RICH2), preshower (SPD/PS), electromagnetic calorimeter (ECAL), hadron calorimeter (HCAL), muon system.

2.2.1 The Vertex Locator (VELO)

The first detector encountered after the pp-interaction is the VErtex LOcator (VELO)[21]. Its main tasks are to reconstruct the trajectories of charged tracks coming from primary vertexes, allowing to reconstruct secondary b-hadron decay vertexes (fundamental to provide an accurate measurement of their decay lifetimes), and to measure the impact parameter of particles used to tag (see section 1.6) their flavor. The VELO measurements are also a crucial input to the second level trigger (L1), which grows up the b-decay content of the data.

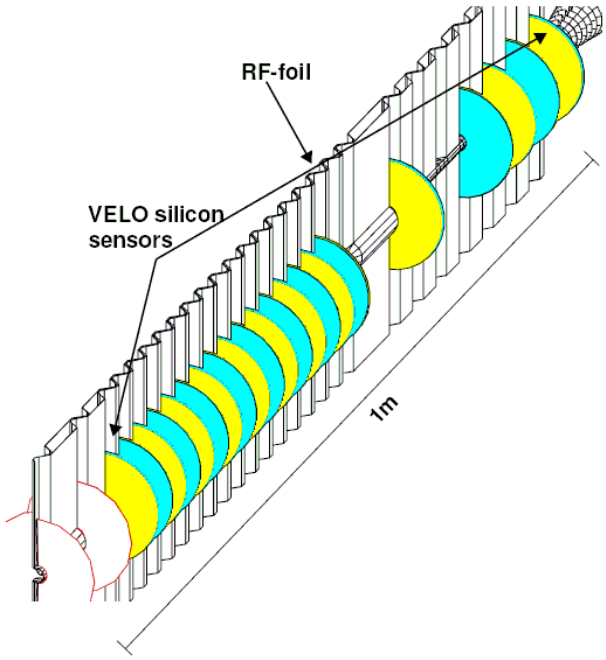

Figure 2.6: Silicon sensors layout with RF foil along the beam axis.

The VELO features a series of 21 disk-shaped silicon stations placed along the beam direction, with a $r - \phi$ segmentation geometry, consisting of two half modules: the left and the right half modules are separated during the filling of the beam. Each of the 21 circular stations is made of 2 couples of half-circles 300 μm thin silicon micro-strips, used to register the hits of the charged tracks passing through. Putting all together will allow us a track identification in the angular range of 15 $mrad$ to 390 $mrad$.

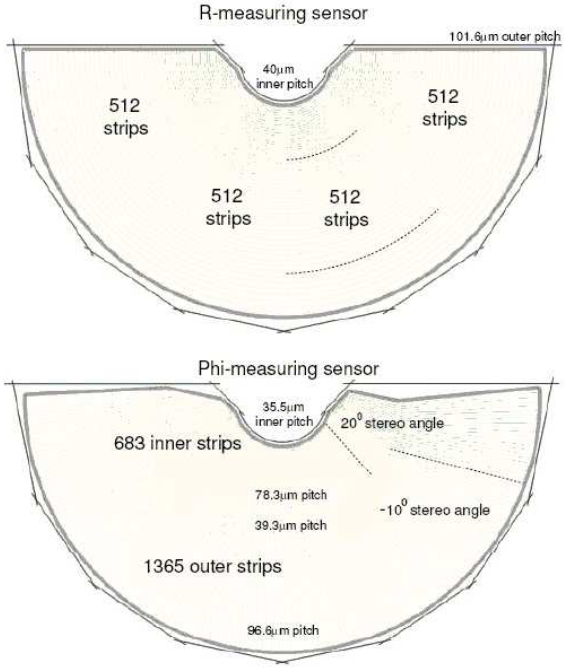

Figure 2.7: Station scheme: r and phi measuring sensors.

Each station shown in Figure 2.7 consists of one r and one ϕ measuring sensor of radius 34 mm. The strip pattern on the r-sensor has a constant radius separation with 512 strips ordered into four sectors of approximately 45°. The ϕ-sensor has straight strips with an inner zone at a 20° stereo angle while the outer zone as a stereo angle of 10°. In addition, two r-measuring sensors are placed upstream of the VELO to act as a pileup veto. They select beam crossings with only one pp-interaction by reconstructing the z-position of the interactions to determine the number of primary interactions within one bunch crossing. For an average event, the resolution on the primary vertex in the z-direction is 42 μm and 10 μm perpendicular to the beam. The precision on the decay length ranges from 220 μm.

After the exit wall of the VELO, the LHC beam is protected by a beam pipe[13] made of two conical sections. The first section is 1.3 m long with a 25 $mrad$ opening angle, while the second one is 16 m long with a 10 $mrad$ opening angle. The beam pipe is designed to minimize the creation of secondary particles, while resisting the air pressure from outside. The first part of the beam pipe is made out of the light-weighted materials beryllium (1.8 m long) and beryllium-aluminum alloy (10 m long). After $z = 13$ m, where the amount of material is not critical anymore, the beam pipe is constructed from stainless steel. The minimal radius is 2.5 cm (limited by LHC injection requirements) and the final radius of the second section is 13 cm.

2.2.2 Ring Imaging Cherenkov Detectors

Excellent $\pi - K$ separation is required in LHCb for high momentum tracks[4]. On the other hand, the identification of kaons accompanying B mesons, from tracks which typically have low momentum, is needed for the flavor tagging. This, together with good particle identification in high multiplicity decays, sets the low momentum limit in LHCb particle identification to approximately 1 GeV/c.

In order to satisfy the requirements of particle identification over a wide range of track momenta and polar angles, a Ring Imaging CHerenkov system (RICH)[22], consisting of two detectors and using three radiators with differing refractive indexes, has been chosen. The two detectors, RICH1 and RICH2, due to their sensitivity to magnetic fields, have been designed to be far as possible from the magnet, upstream (RICH1) and downstream (RICH2) it.

What the RICH does is to detect ring images formed by Cherenkov photons around the track of the particle traversing various radiators, and then to detect the photons produced, using cylindrical pixelated Hybrid Photo-diode Tubes (HPD).

2.2.2.1 RICH 1

The RICH1 detector shown in Figure 2.8, has been designed for low momentum tracks with large scattering angle requiring full angular coverage of the acceptance. The structure is therefore placed close to the interaction point to minimize the surface area. RICH1 covers the momentum range 1-60 GeV/c using two radiators. A 5 cm thick aerogel radiator with refractive index 1.03 identifies kaons above 2 GeV/c and provides a $\pi - K$ separation up to 10 GeV/c. A second larger gaseous radiator of 85 cm contains C_4F_{10} with refractive index 1.0014 and extends the $\pi - K$ separation up to 60 GeV/c. The Cherenkov photons are focused by spherical mirrors with a radius of curvature of 240 cm and are then reflected by plane mirrors towards the photo-detectors.

[4]In order to distinguish, for instance, the $B_0 \to \pi^+\pi^- >$ decay form other two-body final states in which 10% of tracks have momenta greater than 150 GeV

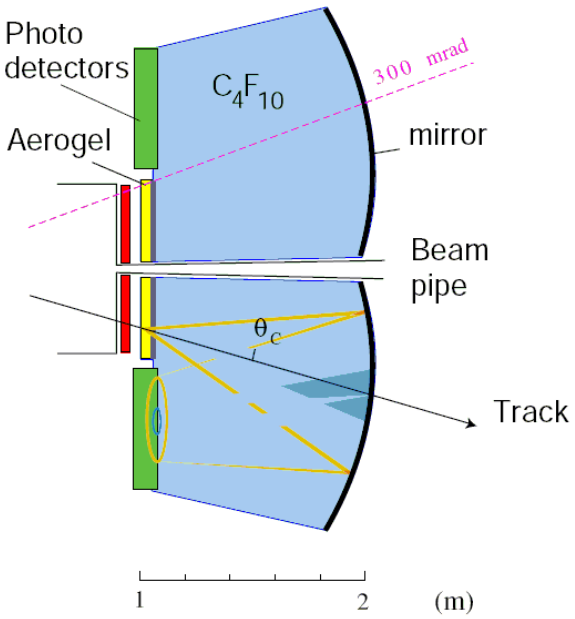

Figure 2.8: RICH1 Detector.

The RICH1 detector underwent big design changes as part of a re-optimization of the LHCb experiment[20]. As a result the RICH1 detector will now be exposed to the fringe field of the magnet to improve track separation at the trigger level. New light materials have been tested to reduce the radiation length of the mirrors. The mirrors will now be made of 2 *mm* thick beryllium. The magnetic shielding needed to be strongly re-enforced to provide sufficient protection for the photo-detectors, while, at the same time drive enough magnetic field towards the Trigger Tracker for a maximum particle separation. The task is made more complicated due to the small space available.

2.2.2.2 RICH 2

The RICH2 detector, shown in Figure 2.9, identifies high momentum particles with an outer acceptance of 120 *mrad* in the horizontal and 100 *mrad* in the vertical plane. It is placed further down-stream to allow a better separation of low angle tracks. There is a single 167 *cm* long radiator filled with gaseous CF_4 of refractive index 1.0005. As in RICH1 the Cherenkov photons are focused with spherical mirrors and deflected onto the photo-detectors with flat mirrors. The focusing mirrors are made of 42 hexagonal segments and 14 half-hexagonal segments of size 52 *cm* across the diagonal, and a radius of curvature of 860

cm. The plane mirrors are made of 40 rectangles of size 410 x380 mm^2 with a 6 mm thick glass substrate. Unlike in RICH1, where the photo-detectors are mounted vertically over and under the structure, the photo-detectors of RICH2 are placed horizontally, on the left and the right outside the acceptance of the spectrometer. While RICH1 is subject to high magnetic field constraints due to the proximity of the magnet, the RICH2 detector only sees 140 G. The soft iron housing designed can easily absorb the field. Thus the magnetic field at the plane of the photo-detectors was not a concern for RICH2.

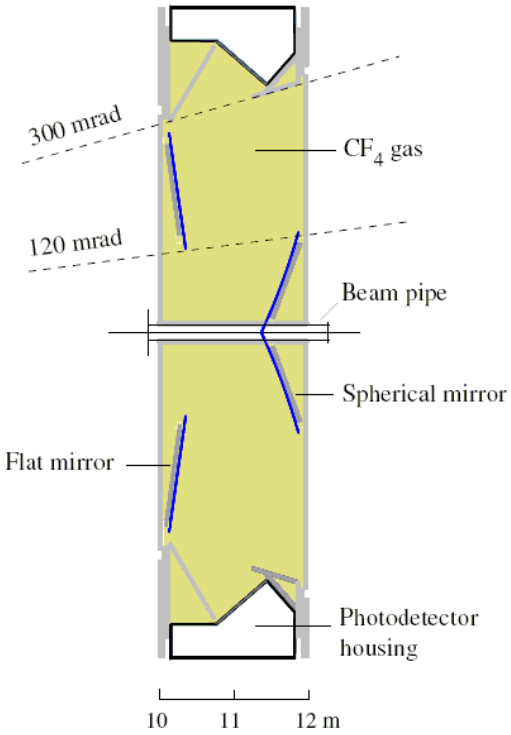

Figure 2.9: RICH2

2.2.3 Tracking System

In LHCb, charged particle trajectories, shown in Figure 2.10, are reconstructed by the Vertex detector placed at the interaction point and by the Tracking stations[24, 25]. The magnet[26] provides bending power for charged particles

to allow particle momentum measurements. The tracking stations provide measurements of track coordinates for momentum determination in the horizontal bending plane of the magnet and sufficient resolution for pattern recognition in the vertical coordinate. The system consists of four planar tracking stations grouped as a Trigger Tracker station (TT), in front of the dipole magnet, and three Tracking stations (T1-T3) placed downstream.

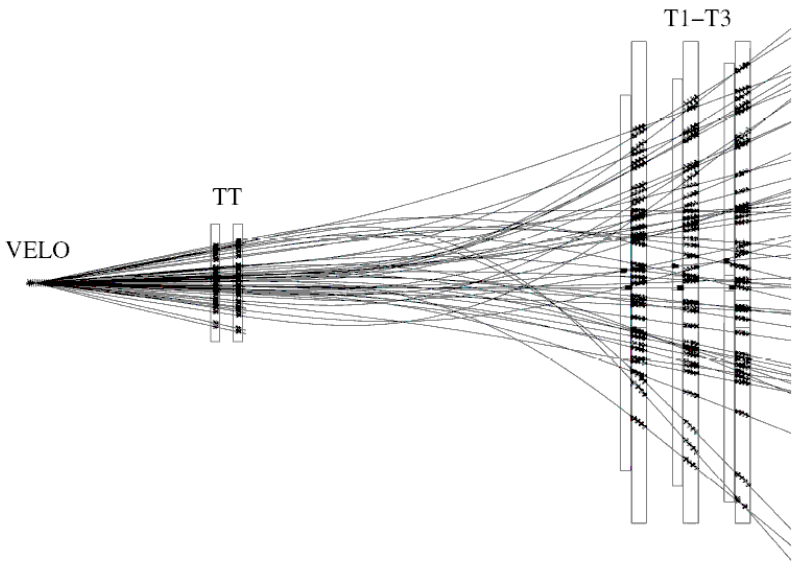

Figure 2.10: Display of the reconstructed tracks and assigned hits in a simulated event using the VErtex LOcator and the Tracking Stations.

2.2.3.1 The Trigger Tracker (TT)

The role of the Trigger Tracker is to determine transverse momentum parameters of charged tracks and to reconstruct long lived neutral particle trajectories decaying downstream of the VELO. TT may also reconstruct low-momentum particles bent out of the acceptance of the experiment before reaching tracking stations T1-T3, further downstream. As the name indicates, data from the TT is used to make the trigger decision. The presence of a low integrated magnetic field of 0.15 Tm between the VELO and the TT is sufficient to assign a rough momentum estimation (with a resolution of 20%-40%) to the tracks.

The entire TT will be equipped with silicon micro-strip detectors with a strip pitch of 198 μm and strip lengths of up to 33 cm. Each sensor is 11 cm long and 7.8 cm wide. The total surface area of TT is 83 m^2. There are four detection

layers of the two different types: the first and the fourth layer have vertical readout strip (x-layers), while the second and the third have strips rotated by a stereo angle of $+5^\circ$ and -5° respectively, in order to measure the y-coordinate and to minimize ghost tracks. The layers are grouped in pairs with the two groups 30 cm apart.

2.2.3.2 Dipole Magnet

The warm dipole magnet[26] of the LHCb experiment provides a bending power of 4 Tm for tracks originating from the primary interaction point. The design is of two trapezoidal coils bent at 45 degrees. The coils are made of 15 individual aluminum "pancakes" stacked together. The generated field is then shaped and guided by an iron yoke on which the coils are mounted. The nominal dissipation power value is 2.4 MW and the polarity of the field can be reversed to reduce systematic errors coming from a possible left-right asymmetry in the detector.

2.2.3.3 Tracking Stations

The three tracking stations T1, T2 and T3 are equidistantly positioned along the beam pipe, between the downstream face of the LHCb magnet and the entrance window of RICH2. The three stations are perpendicular to the beam axis; as the track density at fixed z approximately follows $1/r^2$, the tracking system is segmented in an Inner Tracker, located close to the beam pipe, and an outer tracker covering the remaining 98% of the area. In each tracking station we have the typical four detection layers design, with the same topology as in the TT stations. In the Inner Tracker the sensitive elements of the four layers overlap with each other and with adjacent Outer Tracker modules in both horizontal and vertical direction.

The Inner Tracker The Inner Tracker (IT) covers the innermost region of the T1, T2 and T3 stations, which receives the highest flux of charged particles. It consists of four cross-shaped station equipped with silicon sensors, placed around the beam. The silicon foils are 300 μm thick and have a 230 μm strip pitch, resulting in a resolution of approximately 70 μm. The same readout scheme as for the VELO is foreseen, except for the interface to the Level-1 trigger which is not needed by the IT. The Inner Tracker covers only 1.3% of the sensitive area, but around 20% of all charged particles go through that region.

The Outer Tracker In the T stations, the Outer Tracker (OT) covers the large region outside the acceptance of the Inner Tracker. Charged particles are detected in the OT with gas-filled straw tubes used as drift cells. They have a 5 mm diameter and a 75 μm thick wall and are arranged in modules. Each module is 34 cm wide and contains two layers of straw tubes inside a gas tight box filled with a drift gas mixture Ar (75%) CF_4(15%) CO_2(10%). A standard module is

made of 64 straws per layer, while smaller modules of 32 tubes are placed where the track density is small: above, and below the Inner Tracker acceptance. To reach an average resolution on the momentum of 0.4% the tracking precision has to be optimal in the $x - z$ magnet bending plane. Therefore most stations have two planes with wires in the vertical direction and two stereo planes with wires in the horizontal direction. The choice of the drift gas is driven by the requirement that it should provide a fast signal collection: the constraint is to collect the signal within the time of two LHC bunch crossings. The selected mixture has a maximum drift time of 32.5 ns, so, including a propagation time of the electrical signal of about 10 ns, this results in a total signal collection time slightly below 50 ns, that is the delay of two LHC bunch crossings. Thus, it can happen that two events are piled-up in the outer tracker.

2.2.4 Calorimeter System

Calorimeters are destructive detectors which identify particles by absorbing their energies and momenta in active and passive detector elements. The main purpose of the LHCb calorimeter system[27] is to identify electrons and hadrons and to provide measurements of their energy and position, which are used as input to the Level-0 trigger: they provide high transverse energy particle identification at the early L0 trigger level, when the RICH information is not yet available.

The detector structure is a compromise between a small number of readout channels and a low occupancy with a reasonable energy and position resolution. Fast binary readout has been chosen to satisfy the Level-0 trigger requirements.

The design is motivated by fast triggering requirements, so, the chosen structure consists of three elements: a single-layer Preshower (SPD-PS) detector followed by a Shashlik electromagnetic calorimeter (ECAL) and a scintillating tile hadron calorimeter (HCAL).

2.2.4.1 Scintillator Pad Detector (SPD) and PreShower detector (PS)

The Scintillator Pad Detector (SPD) identifies charged particles by means of 15 mm-thick scintillator tiles, which allow to separate photons from electrons. The light produced by a ionizing particle traversing the tiles is collected by Wavelength Shifting fibers (WLS). The re-emitted green light is guided outside the detector acceptance towards 16 channel Multianode Photomultiplier Tubes (MaPT) via clear plastic fibers.

The SPD is followed by the PreShower detector (PD) that consists of 12 mm-thick lead plane placed in front of 15 mm-thick scintillator plane. The lead plates allow electrons to interact and hence produce an extra shower before reaching the scintillator plates. As a result they have a larger energy deposit than pions, hence improving the separation.

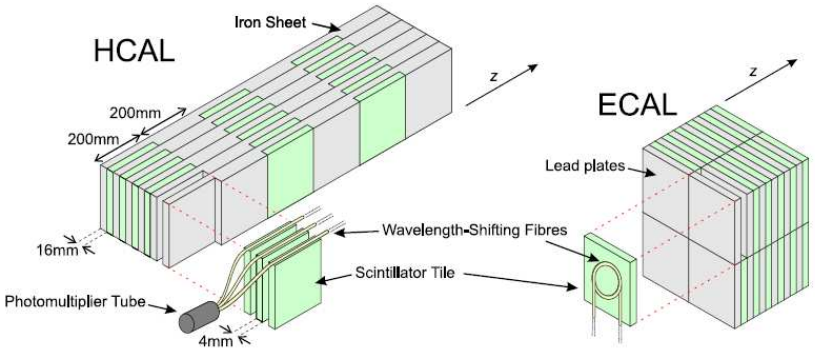

Figure 2.11: Schematic layout of the scintillator tiles and absorbers of the HCAL (left) and ECAL (right).

2.2.4.2 The Electromagnetic Calorimeter

The Electromagnetic CALorimeter (ECAL) measures the energy of the electromagnetic showers from photons and electrons. The shower's energy is sampled by detector elements with a particular geometry, studied to respond to the different track density areas, with three cell sections of decreasing resolution. The cells size are 4x4 cm^2 in the central region, 6x6 cm^2 in the middle region and 12x12 cm^2 in the outer region, with a total of 5984 cells. The cells, shown in 2.11, are alternating planes of 4 mm-thick lead sheets as absorbing material, and 2 mm-thick scintillator tiles which sample the particle showers. Its total radiation length is $25X_0$ and the used technology of a sampling scintillator/lead structure read out by plastic WLS fibers is called Shashlik. The shower energy resolution is:

$$\frac{\sigma(E)}{E} = \frac{10\%}{\sqrt{E}} \oplus 1.5\% \tag{2.2}$$

where E is expressed in GeV.

2.2.4.3 The Hadron Calorimeter

The Hadron CALorimeter (HCAL) identifies hadrons via inelastic interactions with the detector material. The products of the interaction are mainly π, which

are detected in the scintillator. The HCAL is composed by 16 mm thick iron sheets and 4 mm thick scintillating tiles (see Figure 2.11), parallel to the beam, arranged in 1468 cells, spread in a way that the HCAL cell boundaries project to the ECAL cell boundaries. In the HCAL there are only two different regions: 13x13 cm^2 and 26x26 cm^2 are the cell sizes. The light is collected at the end of the tile by wavelength shifting fibers (WLS). The energy resolution is:

$$\frac{\sigma(E)}{E} = \frac{80\%}{\sqrt{E}} \oplus 10\% \tag{2.3}$$

where E is expressed in GeV.

2.2.5 Muon System

Muons are present in many CP-sensitive B-meson decays and rare decays with new physics potential. Triggering on muons and their efficient identification is hence a fundamental requirement for LHCb. A fully detailed description on the Muon System[28] will be given in Paragraph 2.3.

2.2.6 Trigger

The trigger system[29] exploits two particular feature of B decays, differentiating them from other inelastic proton-proton interactions (minimum-bias events). Firstly, events with b-hadrons have decay products with high transverse momentum due to the relatively large B mass. Secondly b-hadron decays have a displaced secondary vertex due to the long B lifetime.

The LHCb experiment will operate at an average luminosity of $2{\cdot}10^{32} cm^{-2} s^{-1}$, where single interactions dominate, making easier the event selection and reconstruction. On the other hand, on the beam crossing rate of 40 MHz, an inelastic pp interaction happens at an average rate of 16 MHz. The ratio of the bb and minimum-bias cross section is $\sigma_{b\bar{b}}/\sigma_{inel} \approx 0.01$, and the $b\bar{b}$ production rate is therefore about 150 kHz. However, in only about 15% of the events at least one B meson will have all its decay products contained in the acceptance of the spectrometer. Furthermore, the branching ratios of B mesons used to study CP violation are typically less than 10^{-3}. These considerations leads to expect about 10^6 background events per B event of interest.

Given the limited Data AcQuisition (DAQ) and storage capabilities the LHCb trigger must be selective and efficient in extracting these events of interest. The Trigger System has to reduce the 10 MHz (effective) of visible interactions frequency to a few hundreds Hz of events to be stored for further offline analysis.

The Trigger System is organized in three trigger levels: Level-0 (L0), Level-1 (L1) and the High Level Trigger (HLT).

	Level-0	Level-1	High Level Trigger
Input rate	40 MHz	1 MHz	40 kHz
Output rate	1 MHz	40 kHz	200 Hz
Sub-detectors used	VELO, ECAL, HCAL, Muon	All but RICH and T1-T3	All
CPU usage	On detector	20%	55%

Table 2.3: Data rates, sub-detectors used and CPU usage for the different trigger levels.

2.2.6.1 The Level-0 trigger

The first level of triggering, Level-0 (L0), uses the pile-up veto counter of the VELO to reject events with multiple proton-proton interactions. Furthermore, at Level-0, the highest transverse energy photon, electron and hadron clusters in the Calorimeter are reconstructed, as well as the two muons with the highest transverse momentum in the Muon System. In the L0 there are fixed thresholds of transverse energy for each particle, thus an event is accepted by it if the event has one or more particles which exceeds these thresholds and it's not flagged as a multiple interaction.

The Level-0 trigger processing is implemented by dedicated electronics hardware mounted on the VELO, calorimeter system and muon detector. The hardware operates at the bunch crossing rate of 40 MHz and has an output of 1 MHz with a fixed latency[5] of 4 μs. The trigger decision is made by the Level-0 Decision Unit which combines each detector signature into a single trigger decision per candidate. The Level-0 Decision Unit is fully programmable, designed so that the trigger can be readjusted depending on the experimental running conditions.

Efficiencies of approximately 90%, 70% and 50% are achieved for events with muons, hadrons and photons respectively. The relative weight of each trigger can be tuned by changing the single cuts, depending on the type of physics one wants to favor. The optimization of the cuts for the precise measurements of CP-violating parameters leads to a bandwidth of 60% for the hadron trigger, 10% for the electron trigger, 10% for the photon trigger and 20% for the muon trigger.

2.2.6.2 The Level-1 trigger

At the next stage of triggering, the Level-1 (L1) trigger is designed to select events with high transverse momentum from a displaced secondary vertex. The algorithm is to split into two parts. Firstly, a cut is made on an impact parameter variable, calculated from the properties of the two tracks with the highest transverse momentum. This generic trigger algorithm is sensitive to all b-hadron

[5]The latency is the maximum time elapsed between each pp interaction and the arrival of the Level-0 trigger decision at the front-end electronics.

decays. A second set of Level-1 trigger algorithms are designed to identify the signature of specific B decays, and, if found, the action is to relax the generic trigger requirements.

The Level-1 trigger operates at the Level-0 output rate of 1 MHz and has a maximum output rate of 40 kHz, with a variable latency of up to 52.4 ms. Data from the calorimeters, the muon detector, plus tracking information from the VELO and the TT tracking detector are input to the algorithm, as well as data from the Level Decision Unit.

The transverse momentum measurement is made for each selected track by matching tracks in the VELO and the TT, and using the fringe field in front of the magnet, achieving a transverse momentum resolution of $\sim 20\%$ at 1 GeV/c and $\sim 40\%$ at 5 GeV/c.

The L1 algorithm will be implemented on a commodity processors farm, which is shared between Level-1, HLT and offline reconstruction algorithms. Using two high impact parameter tracks with the highest p_T , efficiencies between 50% and 70% are achieved.

2.2.6.3 The High Level Trigger

The third and final level trigger is called the High Level Trigger (HLT) and makes use of the all sub-detectors informations. Both the Level-1 trigger and the HLT are implemented in software, running on a farm of around 1800 CPUs in the detector counting room, with the L1 taking priority due to its limited latency needs. The HLT will have access to all the data from the LHCb detector and is separated in generic and specific HLT. The generic is designed to enhance the b content and identify events with μ and J/ψ, while the specific HLT looks for particular B meson decays. First, the generic HLT reduces the rate down to 10-15 kHz by re-running the Level-1 cuts with improved matching between the primary vertex, VELO and TT tracks, a well as further track matching to the full tracking system, including the station T1-T3. As a result, the momentum resolution is better than $\sigma_p/p = 0.6\%$. Secondly the specific HLT is run, with individual cuts defined for each decay channel. Bandwidth limits are then imposed according to the physics goals. The selected events are then written on disk at a rate of 200 Hz where an offline analysis can be applied.

2.2.7 Software Framework

The LHCb software is built within the C++ GAUDI framework[30]. It provides administrative tools such as data persistency and histogramming, as well as allowing run-time configuration via custom-format options files. The software can be divided into two parts: the simulation system, and the system for analyzing the data. When data-taking begins, the analysis software optimized on the Monte Carlo data will then be applied to the real data. In Figure 2.12 it is possible to see a raw scheme of the interactions between the most important softwares used in the LHCb Experiment.

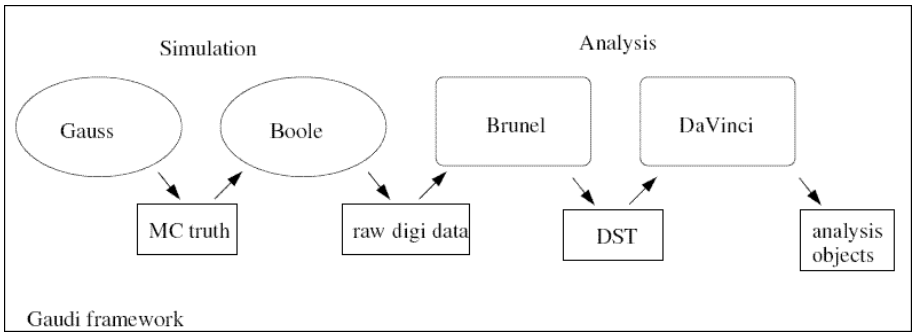

Figure 2.12: The logical structure of the LHCb software.

2.2.7.1 Simulation

Gauss

The Monte Carlo events are generated by the simulation application, *Gauss,* combining event generation and the simulation of the passage of particles through the detector. The first phase is the generation of pp collisions and the subsequent decay of b-hadrons. This is carried out using a combination of Pythia and a specialized B-decay package, EvtGen[31]. The second phase, the simulation of the physics processes that the particles undergo as they travel through the material of the LHCb detector, is based on the GEANT4 toolkit[32].

Boole

A separate application, *Boole*, simulates the response of each sub-detector to the output from Gauss producing *raw digi data* files in exactly the same format as the experimental electronics and data acquisition systems. The effect of adjacent bunch crossing in sensitive detectors is included, as its information on the resolution and imperfection of each detector measured in test beam data.

2.2.7.2 Analysis

Brunel

The essential aim of the analysis software is to recover the fundamental physics of the B decays. In the case of simulated data this means effectively inverting the simulation process. *Brunel* is the first tool in this procedure, analyzing the *raw digi data* files to reconstruct physics objects, like calorimeter clusters, tracks, or rings in the RICH detector. The output from *Brunel* is in the form of a *data summary tapes* (DST) file containing all the reconstructed objects, including the combined particle identification informations from the RICH detectors, calorimeter system and muon detector, as well as the tracks, calorimeter clusters etc.

The *Brunel* application is designed to treat *raw digi files* identically whether they originate from the simulation or real data. It also interfaces to the detector description and the condition database, describing the running conditions of the experiment, such as the alignment and calibration.

DaVinci

The DST files are input to the LHCb offline analysis application, *DaVinci*, which creates high level objects like particles and vertexes, and ultimately performs the event selection. Various DaVinci tools are provided, for example to combine particle objects into decay chains, identify signal events, and perform the flavor tagging algorithms. When run on simulated data, these tools are used for the evaluation of the physics performance of the code, since they allow access to the Monte Carlo truth information recorded at each stage of the simulation.

The output from DaVinci can take several forms. For example, it can be output to the LHCb event visualization system, *Panoramix,* output to reduced DST file containing only events which satisfy a certain selection criteria, or output n-tuple suitable for analysis using the ROOT framework[33].

2.3 Muon System

One of the most important task concerning the LHCb Experiment is the muon detection: muon particles can be found in the final states of many B-decays which are sensitive to CP violation. In particular, muons are present in the final state of the two 'gold plated' B meson decays[6] discussed in sections 1.5.2 and 1.5.4. Furthermore, the charge of muons coming from semi-leptonic b decays is used to tag the initial state flavor of the accompanying neutral B mesons. Muons are foreseen in rare B decays also, such as the flavor changing neutral current $B_s^0 \to \mu^+\mu^-$ decay. Therefore efficient muons triggering and identification are fundamental requirements for the LHCb experiment. Muon particles with high transverse momentum are a typical signature of a b-hadron decay, and the Muon System uses this properties both for muon trigger and reconstruction algorithms.

The most important task for the muon detector is to provide a high-p_T muon trigger already at the Level-0 trigger with a 95% efficiency. The effective LHCb Level-0 input rate, as told before, will be about 15 *MHz* on average, assuming a non-diffractive pp interaction cross-section of 55 mb at the nominal luminosity of $2 \cdot 10^{32} cm^{-2} s^{-1}$.

This input rate has to be reduced to 1 *MHz* within a latency of 4.0 μs. In order to achieve this goal, the Muon system has the following tasks: detect the muon particles (with a time resolution sufficient to give a 99% efficiency within a 20 ns time window), unambiguously identify the bunch crossing which generated the detected muons, and then select the muon track and measure its p_T with a resolution of 20 %.

[6] In both these two channels, $B_d^0 \to J/\Psi(\mu^+\mu^-)K_s^0$ and $B_s^0 \to J/\Psi(\mu^+\mu^-)\Phi$, there are two muons in the final state coming from the J/Ψ resonance.

The Muon System is also used for muon identification at the offline level. Efficient muon identification, with a low contamination of misidentified pions, is required both for tagging and for a clean reconstruction of B-decays with muons in the final state[7] [28].

2.3.1 Detector structure

The Muon system is constituted by five tracking stations placed along the beam axis direction. The first station, called M1, plays an important role for the muon track p_T measurement. It is placed at 12.1 m from the interaction point, in front-of the electromagnetic calorimeter, in order to reduce the effect of multiple scattering, thus improving the transverse momentum resolution of about 30% [29].

This location causes the first muon station to be exposed to a high particle rate, which reaches, in its inner part, values of about 230 kHz/cm^2 at the nominal luminosity value. The other four muon stations are located after the hadronic calorimeter, at an average position of 15.2 m (M2), 16.4 m (M3), 17.6 m (M4), 18.8 m (M5), and are interleaved with iron wall shields that, together with the calorimeters, attenuate hadrons, electrons and photons. Each wall is 80 cm of thick, and is followed by about 40 cm of space before each muon station. Another iron wall is placed after the last muon station to protect it from hadrons and muons emerging from the collider tunnel (Figure 2.13) .

Each station is divided into four rectangular regions (R1÷R4), concentric around the beam pipe axis, designed to receive approximately the same particles flux. The Muon System inner and outer angular acceptance are 20 (16) $mrad$ and 306 (258) $mrad$ in the bending (non-bending) plane respectively.

MultiWire Proportional Chambers (MWPC), which represent a well known and robust technology, have been adopted as the baseline detector, in all the regions where the expected particles rates are between 200 Hz/cm^2 and 200 kHz/cm^2 . In the innermost region of the first muon station, mostly due to the need of a 10 years radiation hardness capability, Gas Electron Multiplier (GEM) detectors[34, 35] have been adopted. The Muon System particle rate, calculated with a safety factor of two for M1 and five for the other stations, is shown in Tab. 2.4. The area of each muon station/region and the stations dimensions are also reported. The total Muon Detector area is about 435 m^2.

Because of the projectivity of the LHCb detector to the interaction point, the MWPC dimensions depend on the required x-y granularity inside each station and region of the muon system. Moreover, the LHCb MWPCs are readout differently, depending on their position in the muon system. In region R4 of stations M1-M3 the chambers have anode-wire readout through decoupling capacitors. In region R3 of stations M1-M3 and regions R1 and R2 of stations M4 and M5 cathode pads are readout. Finally in regions R1 and R2 of stations

[7] Muons reconstructed in the high precision tracking detectors with momenta down to 3 GeV/c must be correctly identified with an efficiency of about 95% while keeping the hadron misidentification rate below 1%. Efficient muon identification with low contamination is required both for tagging and the clean reconstruction of muonic final state B decays.

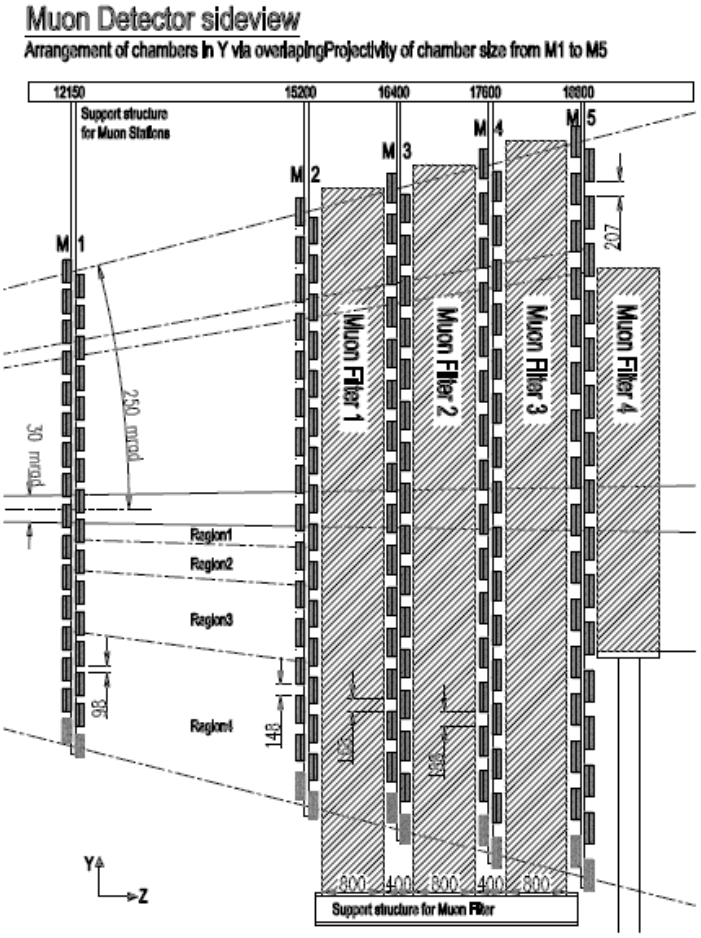

Figure 2.13: Side-view of the muon system in the y-z plane

	M1	M2	M3	M4	M5
R1	460 $\frac{kHz}{cm^2}$ 0.6 m^2	37.5 $\frac{kHz}{cm^2}$ 0.9 m^2	10 $\frac{kHz}{cm^2}$ 1 m^2	6.5 $\frac{kHz}{cm^2}$ 1.2 m^2	4.4 $\frac{kHz}{cm^2}$ 1.4 m^2
R2	186 $\frac{kHz}{cm^2}$ 2.3 m^2	26.5 $\frac{kHz}{cm^2}$ 3.6 m^2	3.3 $\frac{kHz}{cm^2}$ 4.2 m^2	2.2 $\frac{kHz}{cm^2}$ 4.8 m^2	1.8 $\frac{kHz}{cm^2}$ 5.5 m^2
R3	80 $\frac{kHz}{cm^2}$ 9.2 m^2	6.5 $\frac{kHz}{cm^2}$ 14.4 m^2	1.0 $\frac{kHz}{cm^2}$ 16.8 m^2	750 $\frac{Hz}{cm^2}$ 19.3 m^2	650 $\frac{Hz}{cm^2}$ 22.1 m^2
R4	25 $\frac{kHz}{cm^2}$ 36.9 m^2	1.2 $\frac{kHz}{cm^2}$ 57.7 m^2	415 $\frac{Hz}{cm^2}$ 67.2 m^2	250 $\frac{Hz}{cm^2}$ 77.4 m^2	225 $\frac{Hz}{cm^2}$ 88.3 m^2
area (m^2)	7.7 x 6.4	9.6 x 8.0	10.4 x 8.6	11.1 x 9.3	11.9 x 9.9

Table 2.4: The Muon System particle rate, calculated with a safety factor of two for M1 and five for the other stations. The area of each muon station/region and the stations surfaces are also reported.

M2 and M3 a combined readout of wire and cathode pads is used as a consequence of the required granularity. Anode wires are grouped into vertical strips to measure x whereas the y coordinates are provided by the granularity of the horizontal cathode pads. Wires are grouped in pads (*wire pads*) of 4 to 42 to match the required granularity. A complete summary is reported in table 2.5.

In each station, the number of physical channels per region ranges from 2112 to 9216, so the total number of physical channels in the system is 121,536. In order to reduce the number of channels to be handled by the off-chamber electronics and the trigger processor, the physical channels are mapped to logical channels [36], whose size is defined by the trigger requirements. The total number of logical channels in the Muon System is 25,920.

The spatial resolution is given by the dimension of a logical pad, whose structure across the detector represents the logical layout. Each logical pad is obtained from the crossing of one or more horizontal and vertical logical channels, whose dimensions are limited by occupancy and capacitance considerations, according to the detector technology. The logical layout describes the x and y granularity in each region of each muon station, as seen by the muon trigger and the off-line reconstruction. Given the different granularity requirements and the large variation in particle flux from the central part, close to the beam axis, to the detector border, logical pads have different dimensions in each region as shown in Figure 2.14.
Region and pad sizes scale by a factor two from one region to the next. The logical layouts in the five muon stations are projective in y to the interaction point. The x dimensions of the logical pads are determined firstly by the precision required to obtain good muon transverse momentum resolution for the Level-0 trigger. The y dimension of the logical pads are determined by the required rejection of background triggers which do not point to the interaction region. The resulting y/x ratios are 2.5 in station M1 and 5 for stations M2 and M3. Stations M4 and M5, which are used to confirm the presence of penetrating

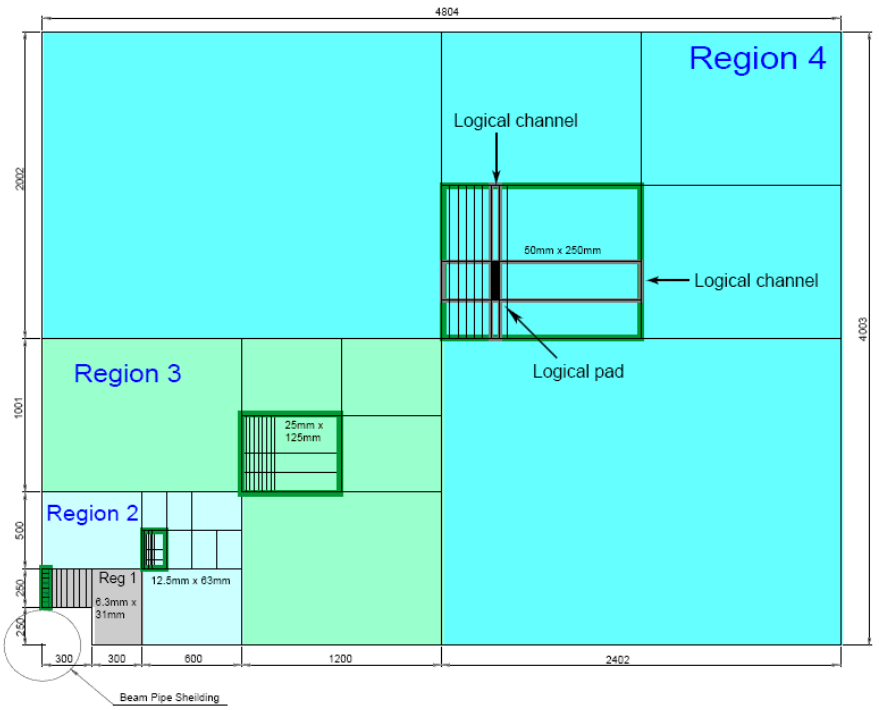

Figure 2.14: Front view of one quadrant of muon station 2, showing the dimensions of the regions. Inside each region is shown a sector, defined by the size of the horizontal and vertical strips. The intersections of the horizontal and vertical strips, corresponding to the logical channels, are logical pads. The region and channel dimensions scale by a factor two from a region to the next.

	R1	R2	R3	R4
	24 Gem	24 MWPC	48 MWPC	192 MWPC
M1				W (40)
	C (10 x 25)	C (20 x 25)	C (20 x 100)	
	12 MWPC	24 MWPC	48 MWPC	192 MWPC
M2	W (6.3)	W (12.5)		W (50)
	C (37.5 x 31.3)	C (75 x 31.3)	C (25 x 125)	
	12 MWPC	24 MWPC	48 MWPC	192 MWPC
M3	W (40.5)	W (13.5)		W (54)
	C (40.5 x 33.7)	C (162 x 33.7)	C (27 x 135)	
	12 MWPC	24 MWPC	48 MWPC	192 MWPC
M4				W (58)
	C (29 x 36)	C (58 x 72)	C (58 x 145)	
	12 MWPC	24 MWPC	48 MWPC	192 MWPC
M5				W (62)
	C (31 x 39)	C (62 x 77)	C (62 x 155)	

Table 2.5: Number and type of chamber for each station/region, readout channel used and width in mm (W=wire pads) and/or in mm^2 (C=cathode pads).

muons, have ratios of 1.25.

The L0 trigger algorithm is implemented independently for the four quadrants of the Muon System. To simplify the trigger processing and to hide the complex muon stations layout, the Muon System is subdivided into 192 towers pointing to the interaction point. The intersection between a tower and a station maps a trigger sector. The tower is the key element of the trigger processor and each one is connected to a Processing Unit (PU). Figure 2.15 summarizes the logical complex of the muon detector.

2.3.2 Level-0 muon trigger

The muon tracks selection is performed by the L0 muon trigger. It looks for muon tracks with a large transverse momentum, searching for hits defining a straight line through the five muon stations and pointing to the interaction point region. The position of a track in the first two stations allows determination of p_T as shown in Figure 2.16.

The L0 muon trigger is implemented with the four quadrants of the muon system treated independently. Track finding in each region of a quadrant is performed by 12 processing units, arranged on processing boards in groups of four for regions R1, R3 and R4, and in pairs for region R2. A processing unit collects data from the five muon stations for pads and strips forming a tower pointing towards the interaction point, and also receives informations from neighboring towers. For each logical pad hit in M3 (*track seed*), the straight line passing

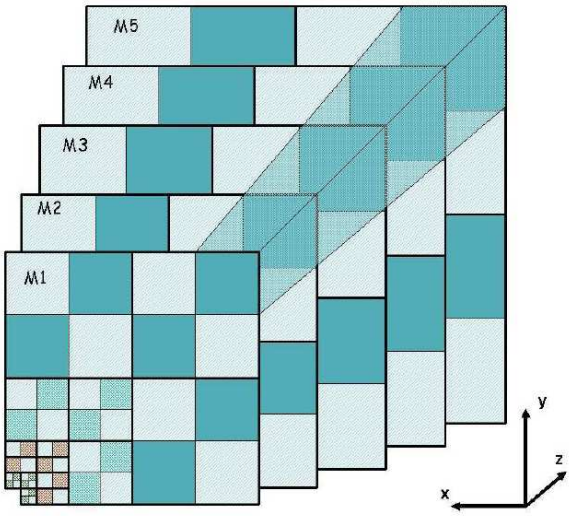

Figure 2.15: A quadrant of the Muon System showing the towers layout. The thick lines groups the towers of the same processing board.

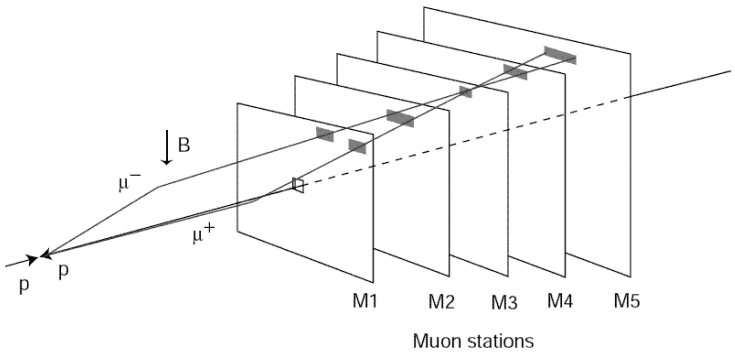

Figure 2.16: Track finding by the muon trigger.

through the hit and the interaction point is extrapolated to M2, M4 and M5. Hits are searched in these stations into search windows, called fields of interest (FOI), approximately centered on the straight-line extrapolation. The size of the FOI depends on the station considered, the distance from the beam axis, the level of background, and the minimum-bias retention required.

When at least one hit is found inside the field of interest for each of the stations M2, M4 and M5, a muon track is flagged and the pad hit in M2 closest to the extrapolation from M3 is selected for subsequent use. The track position in station M1 is determined by making a straight-line extrapolation from M3 and M2, and identifying in the M1 field of interest the pad hit closest to the extrapolation point. Once track finding is completed, an evaluation is performed for a maximum of 2 muon tracks per PU. The two muon tracks with the highest transverse momentum are selected for each quadrant of the muon system.

The heavy flavor content of triggered events is enhanced by requiring the candidate muons to have high p_T . The maximum of two muon tracks per Processing Unit can be selected, if more candidates are found, they are discarded and the PU gives an overflow. The two muon tracks of highest p_T are selected for each processor board first, and then for each Muon System quadrant. Therefore the information for up to 8 muon tracks is transmitted to the L0 Decision Unit which every 25 ns collects the information of a defined bunch crossing also from the other L0 sub-triggers (calorimeter and pile-up systems) and combines them to take the decision to acquire or not the event.

2.3.3 The Multiwire Proportional Chambers

As illustrated in table 2.5, the muon system will be equipped, except in the region R1 of the station M1, with the MultiWire Proportional Chambers (MWPCs). The final MWPC design consists in a chamber containing four sensitive 5 mm gaps (except in station M1, where each chamber contains two sensitive gaps in order to reduce the radiation length X_0), which are connected as two double gaps to two front-end channels, providing high efficiency and fast response[8].

The panels are the basis of the MWPCs mechanical structure. A panel consists of two copper clad FR4 (fire-resistant fiberglass epoxy) laminates, interleaved with a core. For the M1 panels, the core is composed by Nomex honeycomb, while for all the other panels the core consists of polyurethanic foam. Panels are interleaved by sensitive gaps, in which we have wire and pads (see Figure 2.17).

On the long sides of the wire panels, wire fixation bars are glued. They have been made according to standard printed circuit board (PCB) technology and are interconnected in groups of 12 wires. A guard wire of 100 μm diameter will be used as last wire to avoid very high fields on the wires at the chamber border. Guard traces of 0.5 mm width between the cathode pads are foreseen to minimize the cross talk.

[8] A good time resolution is needed in order to have an efficiency higher than 95% in 20 ns time window.

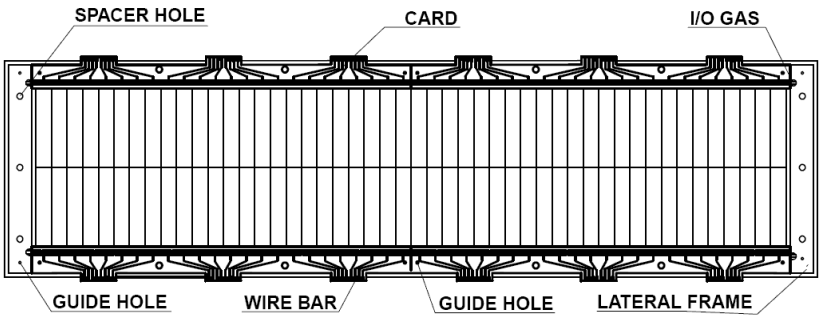

Figure 2.17: Schematic layout of an M2R3 cathode plane, wires will be fixed connecting the two wire bars (up and down).

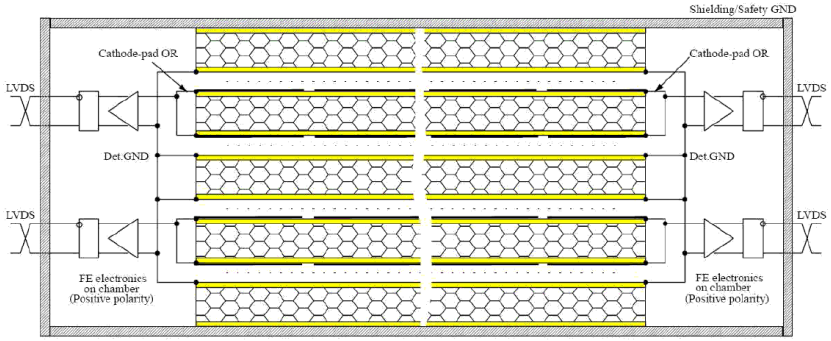

Figure 2.18: A schematic view of the cathode pad readout chain. The figure shows a horizontal section of the chamber with the wires perpendicular to the page.

The High Voltage connection is realized by interface cards which carry the loading resistors and the decoupling capacitors. The HV is distributed via an HV-bar connected to each group of wires. The same side (long side) cathode pads of the upper and lower two gaps are OR-ed in order to have two double-gap with 96 channels each one (192 FE channels in the full chamber). (See Figure 2.18)
Different choices have been made from the technical proposal until now for the gas mixture, time by time changing the CF_4 content inside the mixture. The effect of decreasing the CF_4 is a slightly broader time resolution distribution and a slight instability at high voltage. On the other hand, a high content of CF_4 is a potential factor of ageing because of the possible etching of the chamber panels (FR4 surfaces). Thus, the MWPC gas mixture has been chosen to be $Ar/CO_2/CF_4$ (40:55:5). In Figure 2.19, the behavior of the efficiency curve and the time resolution of a double gap with respect to the high voltage is shown

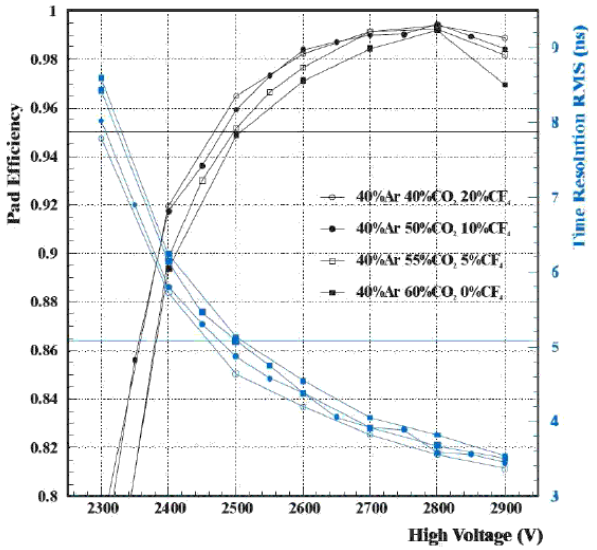

Figure 2.19: Efficiency (black) and time resolution (blue) with respect to the high voltage for four gas mixtures.

for four different gas mixtures.

A muon crossing the 5 mm MWPC gas gap will leave an average 50 electrons that drift to the wires in the electric field. The electrons and ions moving in the avalanche close to the wire induce a negative signal on the wire and a positive signal with the same shape and about half the magnitude on each of the cathodes.

The basic geometry of the MWPCs leads to an electric field of $\sim 8kV/cm$ at the operating point of 2.65 kV. As a consequence, the tolerances for detector construction are very tight, and the large electric field on the cathode might cause additional problems in the long term operation. It is well known that the cathode field can be reduced by increasing the wire spacing (*pitch*), which causes on the other hand a reduced time resolution and in turn a reduced efficiency within a 20 ns time window. Simulation studies [37] showed that the time resolution has an intrinsic limit and cannot be improved by reducing the wire spacing below 1.5 mm. This value has been therefore assumed optimal and used for the prototype studies at the time of the TDR, accepting the drawbacks caused by the large cathode field.

After several beam tests a detailed performance comparison of double-gap chambers with 1.5 mm and 2 mm wire spacing has been carried out [38]. An important result has been that a time resolution of about 4 ns at the operating point can also be obtained with 2 mm wire spacing, leading to 95% double-gap efficiency within a 20 ns time window. Figure 2.20 compares the results for both wire and cathode readout obtained with the two different wire pitches.

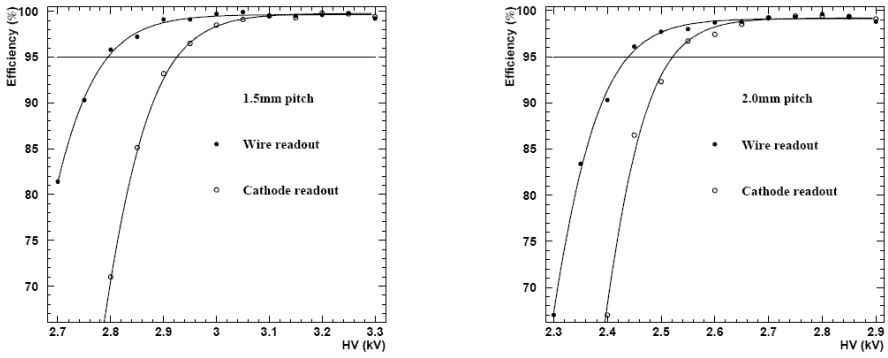

Figure 2.20: Double-gap MWPC efficiency for wire and cathode readout in a 20 ns window with 1.5 mm pitch (left) and 2.0 mm pitch (right).

It was therefore decided to adopt the official wire spacing of 2 mm for all the chambers.

The front-end electronics has been implemented in two stages; the first stage as a spark protection board (SPB) and the second as the Amplifier Shaper Discriminator (ASD) chip board. The chip board is mounted parallel to and immediately above the SPB. Each board receives the signals from 8 cathode-pads readout channels from each double gap, thus in total 24 ASD chip boards are needed to readout all the 192 FE channels for a full chamber. The SPB will be a 50×70 mm^2 two layers board containing a system of resistors and diodes for each channel designed to limit the voltage in the event of a spark or discharge. This design fully protects the readout channels up to 3.6 kV applied to the chamber. The chip board is a 50×70 mm^2 four layers PCB containing two ASD chips.

2.3.4 Electronics

The Front-End Electronics (FEE) for the Muon System is based on two custom ASIC (Application Specific Integrated Circuits) developed in a radiation-tolerant technology able to work without problems at the high particle rate on which the Muon Detector will be exposed in the next 10 years of LHCb data-taking. Before being sent to the trigger system, signals generated on chambers are processed by the FEE in order to be amplified and digitalized. This operation is done on the chambers themselves by the front-end boards. Considering that the muon system will be equipped with chambers very different in dimensions and readout system, the front-end electronics must match with a wide range of detector capacitance and must accept positive signals and negative signals as well. Moreover, in the highest rate region (i.e. the inner part of M1) the maximal total dose expected is about 1 MRad in 10 LHC years of data taking, which requires the use of radiation hard technology.

At the end, for the Muon System, the main components of the FEE are

2 chips, the CARIOCA and the DIALOG chip, connected together to give a Front-End Board (FEB), the CARDIAC board.

The CARIOCA chip

The first ASIC described is an Amplifier Shaper Discriminator (ASD) chip called CARIOCA (Cern And RIO Current-mode Amplifier) developed by the CERN and Rio de Janeiro group of LHCb using IBM 0.25 μm CMOS technology [39]. It is composed by 8 identical channels with the main task to amplify the chamber signal, before discrimination. Its most important characteristic lies in the amplifier, developed following the current-mode approach, which makes the response of the circuit faster, and in an adjustable gain allowing different detector applications.

Amplified signals go through unipolar shaping and through a non-linear baseline restoration circuit that reduces the baseline fluctuations produced by the long tail of the input signal. This signal is then presented to a discriminator circuit that, depending on threshold level set externally, produces a pulse at the output when the input charge exceeds the threshold. The discriminator output is sent to a LVDS cell and is converted to external low level signals.

The power consumption for each CARIOCA channel is about 43.3 mW (46.6 mW) for the positive (negative) amplifier. The signal peaking time in front of the discriminator is 10-15 ns, depending on the detector capacitance that varies from 20 pF to 220 pF. The input resistance of the chip is lower than 50 Ω. The average pulse width is within 50 ns. The chip noise is lower than 2 fC up to a detector capacitance of 200 pF. The sensitivity is 16 mV/fC for the positive amplifier and 14.7 mV/fC for the negative one, measured at a detector capacitance of 0 pF. For a capacitance of 220 pF there is a factor 2 less. The sensitivity variations are less than 5% of R.M.S. overall and less than 2.5% of R.M.S. for chip.

The DIALOG chip

The second front-end ASIC is DIALOG (DIagnostic time Adjustment and LOGics) [40] which provides on-chamber formation of logical channels (LCH) from physical channels (PCH) discriminated by the CARIOCA chip. The DIALOG chip is an integrated circuit developed, as the previous one, in the IBM 0.25 μm CMOS radiation tolerant technology. DIALOG reshapes the PCHs with a programmable time width and provides the fine time delay compensation, programmable PCH by PCH. Each input signals can be individually masked and monitored. DIALOG provides also the voltage threshold signals needed to the CARIOCA discriminators, and, its output signals, called LCHs, are programmable logical combinations of the PCHs input signals. All DIALOG programmable facilities are configurable by the I^2C bus interface. Following the data path, we can identify the following blocks: 16 physical channels inputs, a multiplexer selecting either the input signals or a pattern stored on the chip registers, delayers and digital shapers, the physical channels masking box and

finally the logical channel generation unit. The DIALOG chip also allows to switch between the AND and the OR feature of the input logical channels, giving therefore the possibility to treat the chamber as a double layer or a single layer, allowing future implementations still not discussed.

The CARDIAC board

In the Muon System there are 15,264 CARIOCA and 7,632 DIALOG devices. CARIOCA and DIALOG chips are connected in the same front-end board , the so called CARDIAC board (CARioca-DIAlog Card) [41]. In each CARDIAC there are two CARIOCA devices and one DIALOG. Each board can generate a maximum of eight logical channels and, depending on the local topology, eight, four or two outputs of the card are used. The digital outputs of variable pulse width can also exit from CARDIACs for special tests on the chambers and on the electronics also when not connected to the chamber. It is not on the program to use this feature during normal data taking.

The CARDIAC, is a 6 layer PCB: 2 plane layers (power and ground) and 4 connection layers. On the top layer, that lies on the outer side of the chamber, are mounted:

- one DIALOG chip,
- the power supply,
- the I^2C interface
- and the output connectors,

while on the bottom layer (inner side of the chamber) are mounted:

- two CARIOCA chips,
- the input connectors
- and the LVDS terminations (outputs of the two CARIOCAs).

Chapter 3

Quality Management Systems

Introduction

All the processes involving every single part of the detector's construction, from the material procurement till the last test before the installation, are subject to different requirements, and, to verify the satisfaction to this requirements we need a Quality Management System (QMS).

The adoption of a quality management system should be a strategic decision of an organization. The design and implementation of an organization's quality management system is influenced by varying needs, particular objectives, the products provided, the processes employed and the size and structure of the organization.

Considering the enormous variety of different products, objectives and organizations, it can be very useful to have some guidelines in the implementation of a QMS, that can help to improve, just providing some basic rules, the effectiveness of any QMS adopted.

A possible way to obtain a guideline can be to refer to an international accepted standard, as general as possible, that can be applied to all systems, considering different complexity, different number of processes involved and different requirements. At present, the most appropriate standard for this due seems to be the ISO 9001:2000 standard[42].

For what concerns the job made by Ferrara INFN LHCb Group (described in details in Chapter 4) a QMS has been implemented for the construction of more that 200 of MWPCs (product provided) for the Muon Spectrometer of the LHCb Experiment, and the 'customer' can be considered the LHCb collaboration itself of which INFN is one of the main members.

The aim of this chapter is to summarize the statements given by ISO 9001:2000 normative points, using the same logical approach and structure and then referring separately to the same different areas described into the nine ISO 9001:2000 clauses:

- Scope, General Introduction and Process Approach (sections 0, 1, 2, 3 in ISO 9001:2000)
- QMS and Documentations (4 in ISO 9001:2000)
- Management responsibility (5 in ISO 9001:2000)
- Resources Management (6 in ISO 9001:2000)
- Product Realization (7 in ISO 9001:2000)
- Measurement, analysis and improvement (8 in ISO 9001:2000)

3.1 ISO 9001:2000 and Process Approach

The work of preparing International Standards is normally carried out through ISO[1] technical committees. Each member body interested in a subject for which a technical committee has been established has the right to be represented on that committee. International organizations, governmental and non-governmental, in liaison with ISO, also take part in the work[2], so by this way we are guaranteed that this document is applicable everywhere without any restriction.

It is not the intent of this International Standard to imply uniformity in the structure of quality management systems or uniformity of documentation. The quality management system requirements specified in this International Standard are complementary to requirements for products. This International Standard can be used by internal and external parties, including certification bodies, to assess the organization's ability to meet customer, regulatory and the organization's own requirements.

The quality management principles stated in ISO 9000 have been taken into consideration during the development of this International Standard. This International Standard promotes the adoption of a process approach when developing, implementing and improving the effectiveness of a quality management system, to enhance customer satisfaction by meeting customer requirements.

For an organization to function effectively, it has to identify and manage numerous linked activities. An activity using resources, and managed in order to enable the transformation of inputs into outputs, can be considered as a process. Often the output from one process directly forms the input to the next.

The application of a system of processes within an organization, together with the identification and interactions of these processes, and their management, can be referred to as the 'process approach'.

[1] ISO (the International Organization for Standardization) is a worldwide federation of national standards bodies (ISO member bodies).

[2] ISO collaborates closely with the International Electronical Commission (IEC) on all matters of electrotechnical standardization.

An advantage of the process approach is the ongoing control that it provides over the linkage between the individual processes within the system of processes, as well as over their combination and interaction.

The methodology known as '*Plan-Do-Check-Act*' (PDCA) can be applied to all processes and can be briefly described as follows.

Plan: establish the objectives and processes necessary to deliver results in accordance with customer requirements and the organization's policies.

Do: implement the processes.

Check: monitor and measure processes and product against policies, objectives and requirements for the product and report the results.

Act: take actions to continually improve process performance.

When used within a quality management system, such an approach emphasizes the importance of understanding and meeting requirements, obtaining results of process performance and effectiveness, and continual improvement of processes based on objective measurement.

ISO 9001 specifies requirements for a quality management system that can be used for internal application by organizations, or for certification, or for contractual purposes. It focuses on the effectiveness of the quality management system in meeting customer requirements.

However, this International Standard enables an organization to align or integrate its own quality management system with related management system requirements. It is possible for an organization to adapt its existing management system(s) in order to establish a quality management system that complies with the requirements of this International Standard.

All requirements of this International Standard are generic and are intended to be applicable to all organizations, regardless of type, size and product provided.

Due to the nature of our organization and our product, some requirements of this International Standard cannot be applied, so that, these can be considered for exclusion also because claims of conformity to this International Standard it's not required in our case. Anyway, when it's claimed, these exclusions are limited to requirements within clause 7, only under particular conditions.

3.2 QMS and Documentations

The organization shall establish, document, implement and maintain a quality management system and continually improve its effectiveness. First of all to make it possible the organization shall:

- identify the processes needed for the quality management system and their application throughout the organization,
- determine the sequence and interaction of these processes,

- determine criteria and methods needed to ensure that both the operation and control of these processes are effective,
- ensure the availability of resources and information necessary to support the operation and monitoring of these processes,
- monitor, measure and analyze these processes, and
- implement actions necessary to achieve planned results and continual improvement of these processes.

These processes[3] shall be managed by the organization in accordance with the requirements of this International Standard.

Where an organization chooses to outsource any process that affects product conformity with requirements, the organization shall ensure control over such processes. Control of such outsourced processes shall be identified within the quality management system.

3.2.1 Documentation requirements

The quality management system documentation shall include documented statements of a quality policy and quality objectives, a quality manual[4], documented procedures, documents needed by the organization to ensure the control of its processes, and records of all the processes. The documentation can be in any form or type of medium.

The quality manual includes the scope of the quality management system, the documented procedures established for the quality management system, or reference to them, and a description of the interaction between the processes of the quality management system.

Documents required by the quality management system shall be controlled, and a documented procedure shall be established to define the controls needed.

Documents have to be approved for adequacy prior to issue, reviewed and updated as necessary and then re-approved. Changes and current revisions status have to be identified. Relevant versions of applicable documents have to be available at points of use and that documents shall remain legible and readily identifiable. Documents of external origin have to be identified and their distribution controlled. Obsolete documents ha to be prevented from unintended use, and if they are retained for any purpose, a suitable identification have to be provided.

Records are a special type of document and shall be controlled according special requirements. Records shall be established and maintained to provide evidence of conformity to requirements and of the effective operation of the

[3]Processes needed for the quality management system referred to above should include processes for management activities, provision of resources, product realization and measurement.

[4]The extent of the quality management system documentation can differ from one organization to another due to different factors like the size of organization, the complexity of processes and their interactions, or the competence of personnel.

quality management system. Records shall remain legible, readily identifiable and retrievable. A documented procedure shall be established to define the controls needed for the identification, storage, protection, retrieval, retention time and disposition of records.

3.3 Management responsibility

In a small production center, like in any organization, a responsible (a single person, an organization, or a group of persons) have to be identified as 'Top management'. In our case it can be identified as our team leader, while the other people working on the project can be considered overall as the organization. Top management shall provide evidence of its commitment to the development and implementation of the quality management system and continually improving its effectiveness by:

- communicating to the organization the importance of meeting customer[5] as well as statutory and regulatory requirements,
- establishing the quality policy,
- ensuring that quality objectives are established, conducting management reviews, and ensuring the availability of resources.

Top management shall ensure that the quality policy is appropriate to the purpose of the organization, includes a commitment to comply with requirements and continually improve the effectiveness of the quality management system, provides a framework for establishing and reviewing quality objectives, is communicated and understood within the organization,and is reviewed for continuing suitability.

The quality objectives, including those needed to meet requirements for product, have to be established at relevant functions and levels within the organization. The quality objectives shall be measurable and consistent with the quality policy.

Top management shall ensure that the planning of the quality management system is carried out in order to meet the quality objectives, and the integrity of the quality management system have to be maintained when changes to the quality management system are planned and implemented.

Top management shall ensure that responsibilities and authorities are defined and communicated within the organization. In particular shall be appointed a member of management[6] who, irrespective of other responsibilities, shall have responsibility[7] and authority that includes:

[5] Customer requirements have to be well determined without any ambiguity or uncertainty.

[6] Top management itself is a valid choice too.

[7] The responsibility of a management representative can include liaison with external parties on matters relating to the quality management system.

- ensuring that processes needed for the quality management system are established, implemented and maintained,
- reporting to top management on the performance of the quality management system and any need for improvement, and
- ensuring the promotion of awareness of customer requirements throughout the organization.

Appropriate communication processes have to be established within the organization and that communication takes place regarding the effectiveness of the quality management system.

Top management shall review the organization's quality management system[8], at planned intervals, to ensure its continuing suitability, adequacy and effectiveness. This review shall include assessing opportunities for improvement and the need for changes to the quality management system, including the quality policy and quality objectives. The input to management review shall include information on:

- results of audits[9],
- customer feedback,
- process performance and product conformity,
- status of preventive and corrective actions,
- follow-up actions from previous management reviews,
- changes that could affect the quality management system, and
- recommendations for improvement.

The output from the management review shall include any decisions and actions related to:

- improvement of the effectiveness of the quality management system and its processes,
- improvement of product related to customer requirements, and
- resource needs.

[8]Records from management reviews shall be maintained.

[9]The term 'audit', coming from latin language, could mean 'inspecting verification' or 'evaluation' and it is applied to describe an analysis of the processes investigated related to the satisfaction of fixed requirements.

3.4 Resource management

The organization shall determine and provide the resources needed to implement and maintain the quality management system and continually improve its effectiveness, and to enhance customer satisfaction by meeting customer requirements.

The word resources is intended in the most general way, so resource can indicate people working for the organization, competence, awareness and training, infrastructure and work environment.

Personnel performing work affecting product quality shall be competent on the basis of appropriate education, training, skills and experience. The organization shall determine the necessary competence for personnel performing work affecting product quality and provide training or take other actions to satisfy these needs[10]. It is also fundamental to ensure that its personnel are aware of the relevance and importance of their activities and how they contribute to the achievement of the quality objectives, and then have to be maintained appropriate records of education, training, skills and experience of the personnel involved in the QMS.

The organization shall determine, provide and maintain the infrastructure needed to achieve conformity to product requirements. Infrastructure includes, as applicable

- buildings, workspace and associated utilities,
- process equipment (both hardware and software), and
- supporting services (such as transport or communication).

The organization shall moreover determine and manage the work environment needed to achieve conformity to product requirements.

3.5 Product realization

3.5.1 Planning

The organization shall plan and develop the processes needed for product realization. Planning of product realization shall be consistent with the requirements of the other processes of the quality management system. In planning product realization, the organization shall determine:

- the need to establish processes, documents, and provide resources specific to the product;
- required verification, validation, monitoring, inspection and test activities specific to the product and the criteria for product acceptance;

[10] when done it shall evaluate the effectiveness of the actions taken.

- records needed to provide evidence that the realization processes and resulting product meet requirements.

The output of this planning shall be in a form suitable for the organization's method of operations.

3.5.2 Product requirements

The organization shall determine requirements specified by the customer, including the requirements for delivery and post-delivery activities; requirements not stated by the customer but necessary for specified or intended use, where known; statutory and regulatory requirements related to the product, and any additional requirements determined by the organization.

The organization shall review the requirements related to the product. This review shall be conducted prior to the organization's commitment to supply a product to the customer (e.g. acceptance of contracts or orders, acceptance of changes to contracts or orders) and shall ensure that:

- product requirements are defined,
- contract or order requirements differing from those previously expressed are resolved, and
- the organization has the ability to meet the defined requirements.

Records of the results of the review and actions arising from the review shall be maintained. Where the customer provides no documented statement of requirement, the customer requirements shall be confirmed by the organization before acceptance. Where product requirements are changed, the organization shall ensure that relevant documents are amended and that relevant personnel are made aware of the changed requirements.

The organization shall determine and implement effective arrangements for communicating with customers in relation to product information, time needed for delivery, and customer feedback, including customer complaints.

3.5.3 Design and development

Design and development of product involves only few organizations, and in our case is not applicable because design has been planned by the customer (LHCb collaboration), and development is not object of our QMS. Anyway, the logical structure of statements for this single process follows the usual one, applied also for the product realization in general, chronologically, from the beginning we have:

- Design and development planning
- Design and development inputs

- Design and development outputs
- Design and development review
- Design and development verification
- Design and development validation
- Control of design and development changes

3.5.4 Material Purchasing (supply)

The organization shall ensure that purchased (acquired) product conforms to specified requirements. The type and extent of control applied to the supplier and the acquired product shall be dependent upon the effect of the acquired product on subsequent product realization or the final product. In our case different materials come from different INFN sites (e.g. panels from Potenza, side and closing bars from LNF etc.), these particular products are not 'purchased' by our organization, but provided by the collaboration; nevertheless there's a large number of materials purchased by our organization. Both categories are considered equally as Purchased Material.

3.5.5 Supplying informations

The organization shall evaluate and select suppliers based on their ability to supply product in accordance with the organization's requirements. Criteria for selection, evaluation and re-evaluation shall be established. Records of the results of evaluations and any necessary actions arising from the evaluation shall be maintained.

Purchasing information shall describe the product to be purchased, including where appropriate

- requirements for approval of product, procedures, processes and equipment,
- requirements for qualification of personnel, and
- quality management system requirements.

The organization shall ensure the adequacy of specified purchase requirements prior to their communication to the supplier.

3.5.6 Verification of purchased product

The organization shall establish and implement the inspection or other activities necessary for ensuring that purchased product meets specified purchase requirements.

Where the organization or its customer intends to perform verification at the supplier's premises, the organization shall state the intended verification arrangements and method of product release in the purchasing information.

3.5.7 Production and service provision

The organization shall plan and carry out production and service provision under controlled conditions. Controlled conditions shall include, as applicable:

- the availability of information that describes the characteristics of the product,
- the availability of work instructions, as necessary,
- the use of suitable equipment,
- the availability and use of monitoring and measuring devices,
- the implementation of monitoring and measurement, and
- the implementation of release, delivery and post-delivery activities.

The organization shall validate any processes for production and service provision where the resulting output cannot be verified by subsequent monitoring or measurement. This includes any processes where deficiencies become apparent only after the product is in use or the service has been delivered.

3.5.8 Identification and traceability

Where appropriate, the organization shall identify the product by suitable means throughout product realization.

- The organization shall identify the product status with respect to monitoring and measurement requirements.
- Where traceability is a requirement, the organization shall control and record the unique identification of the product.

3.5.9 Preservation of product and customer property

The organization shall exercise care with customer property while it is under the organization's control or being used by the organization. The organization shall identify, verify, protect and safeguard customer property[11] provided for use or incorporation into the product. If any customer property is lost, damaged or otherwise found to be unsuitable for use, this shall be reported to the customer and records maintained.

The organization shall preserve the conformity of product during internal processing and delivery to the intended destination. This preservation shall include identification, handling, packaging, storage and protection. Preservation shall also apply to the constituent parts of a product.

[11] Customer property can include intellectual property.

3.5.10 Control of monitoring and measuring devices

The organization shall determine the monitoring and measurement to be undertaken and the monitoring and measuring devices needed to provide evidence of conformity of product to determined requirements.

Ensuite the organization shall establish processes to ensure that monitoring and measurement can be carried out and are carried out in a manner that is consistent with the monitoring and measurement requirements.

Where necessary to ensure valid results, measuring equipment shall

- be calibrated or verified at specified intervals, or prior to use, against measurement standards traceable to international or national measurement standards; where no such standards exist, the basis used for calibration or verification shall be recorded;
- be adjusted or re-adjusted as necessary;
- be identified to enable the calibration status to be determined;
- be safeguarded from adjustments that would invalidate the measurement result;
- be protected from damage and deterioration during handling, maintenance and storage.

In addition, the organization shall assess and record the validity of the previous measuring results when the equipment is found not to conform to requirements. The organization shall take appropriate action on the equipment and any product affected. Records of the results of calibration and verification shall be maintained.

When used in the monitoring and measurement of specified requirements, the ability of computer software to satisfy the intended application shall be confirmed. This shall be undertaken prior to initial use and reconfirmed as necessary.

3.6 Measurement, analysis and improvement

The organization shall plan and implement the monitoring, measurement, analysis and improvement processes needed to demonstrate conformity of the product, to ensure conformity of the quality management system, and to continually improve the effectiveness of the quality management system. This shall include determination of applicable methods, including statistical techniques, and the extent of their use.

As one of the measurements of the performance of the quality management system, the organization shall monitor information relating to customer perception as to whether the organization has met customer requirements. The methods for obtaining and using this information shall be determined.

3.6.1 Internal inspections

The organization shall conduct internal audits (see 3.3) at planned intervals to determine whether the quality management system conforms to the planned arrangements established by the organization, and is effectively implemented and maintained.

An audit program shall be planned, taking into consideration the status and importance of the processes and areas to be audited, as well as the results of previous audits. The audit criteria, scope, frequency and methods shall be defined. Selection of auditors and conduct of audits shall ensure objectivity and impartiality of the audit process[12].

The responsibilities and requirements for planning and conducting audits, and for reporting results and maintaining records shall be defined in a documented procedure.

The management responsible for the area being audited shall ensure that actions are taken without undue delay to eliminate detected nonconformities and their causes. Follow-up activities shall include the verification of the actions taken and the reporting of verification results.

3.6.2 Monitoring and measurement of processes and products

The organization shall apply suitable methods for monitoring and, where applicable, measurement of the quality management system processes. These methods shall demonstrate the ability of the processes to achieve planned results. When planned results are not achieved, correction and corrective action shall be taken, as appropriate, to ensure conformity of the product.

The organization shall monitor and measure the characteristics of the product to verify that product requirements have been met. This shall be carried out at appropriate stages of the product realization process in accordance with the planned arrangements.

Evidence of conformity with the acceptance criteria shall be maintained. Records shall indicate the person(s) authorizing release of product at each stage.

Product release and service delivery shall not proceed until the planned arrangements have been satisfactorily completed, unless otherwise approved by a relevant authority and, where applicable, by the customer.

3.6.3 Control of nonconforming product

The organization shall ensure that product which does not conform to product requirements is identified and controlled to prevent its unintended use or delivery. The controls and related responsibilities and authorities for dealing with nonconforming product shall be defined in a documented procedure.

The organization shall deal with nonconforming product by one or more of the following ways:

[12] Auditors shall not audit their own work.

- by taking action to eliminate the detected nonconformity;
- by authorizing its use, release or acceptance under concession by a relevant authority and, where applicable, by the customer;
- by taking action to preclude its original intended use or application.

Records of the nature of nonconformities and any subsequent actions taken, including concessions obtained, shall be maintained.

When nonconforming product is corrected it shall be subject to re-verification to demonstrate conformity to the requirements.

When nonconforming product is detected after delivery or use has started, the organization shall take action appropriate to the effects, or potential effects, of the nonconformity.

3.6.4 Analysis of data

The organization shall determine, collect and analyze appropriate data to demonstrate the suitability and effectiveness of the quality management system and to evaluate where continual improvement of the effectiveness of the quality management system can be made. This shall include data generated as a result of monitoring and measurement and from other relevant sources.

The analysis of data shall provide information relating to

- post-delivery customer requirement satisfaction,
- conformity to product requirements,
- characteristics and trends of processes and products including opportunities for preventive action, and
- suppliers and supplied material.

The organization shall continually improve the effectiveness of the quality management system through the use of the quality policy, quality objectives, audit results, analysis of data, corrective and preventive actions and management review.

3.6.5 Corrective and Preventive actions

The organization shall take action to eliminate the cause of nonconformities in order to prevent recurrence. Corrective actions shall be appropriate to the effects of the nonconformities encountered.

A procedure shall be established to define requirements for

- reviewing nonconformities (including customer complaints),
- determining the causes of nonconformities,
- evaluating the need for action to ensure that nonconformities do not recur,

- determining and implementing action needed,
- records of the results of action taken, and
- reviewing corrective action taken.

The organization shall also determine actions to eliminate the causes of potential nonconformities in order to prevent their occurrence. Preventive actions shall be appropriate to the effects of the potential problems.

A procedure shall be established to define requirements for

- determining potential nonconformities and their causes,
- evaluating the need for action to prevent occurrence of nonconformities,
- determining and implementing action needed,
- records of results of action taken (see 4.2.4), and
- reviewing preventive action taken.

Chapter 4

MWPC production in Ferrara

Introduction

Due to the different granularities required in each region of the Muon System (see section 2.3.1), 20 different chamber typologies have been designed. The responsibility for the construction of the 1368 multiwire proportional chambers needed involves six different production sites:
one in Switzerland:

- CERN (24 M1R2, 12 M2R1, 24 M2R2, 12 M3R1, 24 M3R2, 12 M4R1, 12 M5R1);

three in Italy:

- Ferrara (54 M1R4, 48 M2R3, 24 M4R2, 48 M4R3, 24 M5R2),
- Firenze (68 M1R4, 146 M5R4) and
- LNF (48 M1R3, 70 M1R4, 48 M3R3, 48 M5R3, 46 M5R4);

and two in Russia:

- PNPI I (152 M2R4, 192 M3R4) and
- PNPI II (40 M2R4, 192 M4R4).

For each typology it's planned to produce a 10% of spare chambers that leads the total amount to approximately 1500 MWPCs.

The production of those chambers undergoes different stages, from panel construction to chamber dressing, involving usually more than one site. Subject of this chapter is to describe all the procedures performed in Ferrara site, from the pre-production tests (performed on 'naked' panels with only the HVbars glued on them) to the post-production tests (probing the MWPCs satisfaction of requirements before the delivery to LNF for chamber 'dressing').

4.1 Pre-production Tests

The panels are the basis of the chamber mechanical structure. The requirement on the flatness of $\pm 50 \mu m$ is of critical importance for gas gain uniformity and consequently for the width of the operational plateau. As explained in section 2.3, a panel consists of two copper clad FR4 (fire-resistant fiberglass epoxy) laminates interleaved with a core. For what concerns the chambers produced in Ferrara we have two different solutions:

- panels based on honeycomb (M1R4) and
- polyurethane foam (M2R3, M4R2, M4R3, M5R2).

From the point of view of flatness, the honeycomb offers the best results, however, the panels based on polyurethane foam are cheaper and faster to build.

In the first solution FR4-laminates (or where applicable, printed circuit boards, called PCBs) of 1.6 mm thickness with $\approx 30 \mu m$ copper[1] interleaved with 7 mm honeycomb are the baseline panel for the chamber construction.

In the second solution the panels are composed of two sheets of FR4 (like in the other solution, but with 2 different thickness, 0.8 mm and 1.6 mm, for different typologies of MWPC) filled with a rigid polyurethane foam. The polyurethane foam is the result of a chemical reaction between two components: the polyol and the isocyanate. The liquid polyurethane components are injected in a mold between the two FR4 sheets, with a low pressure injector that provides a final density of 400-600 kg/m^3.

The panel construction is provided by an external manufacturer[2], and the panel flatness is measured by the manufacturer with a specific device provided by Roma2 LHCb group. Only the components with a flatness within $\pm 50 \mu m$ are accepted and then sent to Potenza, at Università della Basilicata, where 2 HV bars are glued on a single cathode surface for each panel (except for the ground panels, also called covers, where no HV bars are present), and where the flatness is checked and re-measured.

4.1.1 Panel planarity, cleaning and visual inspections

When they arrive in Ferrara, all the panels are equipped with specific 'travelers' (*Normative Reference on section 3.2.1*) provided by the operators who made the gluing on of the HV bars and checked the flatness of the panels in Potenza. The first step made in Ferrara site is to check those travelers, looking for all informations available (also with special remarks) about the quality of the panels going to be used in the chamber construction.

After a first documentation check, all the panels are individually checked for evident surface imperfections, like big scratches, bumps or depressions that can affect the proper working of an assembled chamber (*NR 3.5.4, 3.5.6*) . When an

[1] Over the copper, only for the cathodes, a thin gold film is then deposed, to prevent the cathode surfaces from oxidation.

[2] GA INTERNORMAL s.r.l. polyurethane transformations.

evident surface problem is found the panel is sent back to Potenza, or to LNF to be recovered (when possible) and it's not allowed to go to the subsequent production stage (*NR 3.5.8, 3.6.3*).

After successful achieved the visual inspection, 20 % of the panels[3] are tested for their electrical components on the HV bars, in particular dumping resistors of $22 \pm 1\Omega$ are checked, and if defect, the whole batch has to be checked and where needed the bad resistor is replaced with a good one (*NR 3.6.3*).

When the preliminary tests doesn't show any particular problem, the panel has to be prepared for the production procedures inside the cleanroom (see section 4.2). The preparation consists of different steps: first of all, excess of glue, and surface imperfections on the HV bars are removed, then, gas inlet/outlet holes are checked and eventually removed from undesired obstacles and then the cathode surface cleaning with acetone and ethanol is performed.

4.1.2 HV bar Height

Another fundamental test before the panel preparation is the HV bar height test, made on the 15-20% of received panels (*NR 3.5.4, 3.5.6).*

For the proper working of the following construction procedures (e.g. wiring, gluing) it's needed that all the HV bars have a well fixed height (referring to the cathode). The optimal height is 2.400 *mm,* an higher value (above all if higher than 2.500 *mm*) will cause the wire touching the HV bar during the wiring causing a wire displacement from the desired position, while a lower value (typically lower than 2.250 *mm*) will cause problems during the gluing procedure.

This test is performed on a specific micro-metric measuring machine inside a dedicated room (*NR 3.3, 3.4*) in use at the Ferrara INFN section, using a large granite table, and an automatic coordinate measuring machine with an high precision[4] head probe, Poli SKY type (see figure 4.1). A simple program allows the determination of the z coordinate (height) on the table plane when a trained authorized operator (*NR 3.4*) enters the x-y plane desired coordinates[5].

Testing panels have to be carefully positioned on a pre-defined position on the table. When the measurement starts, a fixed (depending on the length of the panel) number of height values is taken over the full length of each HV bar of the panel and the same number of height values is taken along the cathode for each corresponding x (length) coordinate. The distance between two consecutive points is 1 *cm*. The difference between each value on the HV bar and its corresponding on the cathode (with y coordinate shifted by 1.5 *cm*) gives us the estimated HV bar height.

A program written in C language makes automatically a graph and a plot for the HV bar height measured and all the data are saved and recorded in a database (*NR 3.2.1*). In figure 4.2 and 4.3 there are two samples of a measured

[3] this is a re-test, because all the components are equally testes in Potenza.

[4] Measurement precision is about $\pm 1\mu m$.

[5] In our case a set of x-y coordinates, previously determined considering the type of panel in measure, is entered automatically by loading a script file.

Figure 4.1: HV bar height measurement room. Measurement precision for the Poli SKY machine is $\pm 1 \mu m$.

panel. The 'HV bar Large' has the external electronic components, while the 'HV bar Small' hasn't.

4.2 Production

After all the preliminary tests and preliminary operations, only when a panel satisfied the needed requirements (*NR 3.5.4, 3.5.6*), it's moved into the cleanroom, where the real MWPC construction starts.

The choice (*NR 3.3, 3.5.2*) to adopt an ISO 4 class[6] cleanroom was mandatory due to the need to reduce much as possible the dust, and any other microscopic particle able to come inside the final MWPCs, that can affect their proper working once assembled. The cleanroom in use in our site, has in total three modules, a 'dressingroom' where people can dress and undress the specific outfit needed (hair and shoes coverings, smocks), an ISO 5 class cleanroom identified as 'grayroom', where the panels and other components (side bars, closing bars etc.) are cleaned before entering the ISO 4 cleanroom, and the proper cleanroom where environmental conditions are strictly and continuously under control. The dressing room communicate with both greyroom and cleanroom, and a placard outside the entrance door informs anyone is going to move into any of the rooms about the outfit needed, without which they are not allowed to move in (*NR 3.3, 3.4, 3.5.7*).

Inside the clean room (as shown in fig. 4.4) we have different facilities:

- A WGS (wiring, gluing, soldering) machine for the specified operations
- An assembling table
- A test table
- A multi-use table

All the procedures are controlled via two PCs located inside the cleanroom, net-connected also with the computer in the grey room (used for the database and for some specific data analysis) and with the PC outside the clean room structure (used for the post-production tests). An electronic[7] 'traveler', shared between all the computers mentioned above, follows (*NR 3.2.1, 3.5.8*) all the procedures concerning any single panel, from preliminary tests and cleaning until final assembling, recording also data, time, and operator(s) for each single operation performed on that panel, and test results with special remarks on problems eventually occurred (*NR 3.6.3*).

[6]The ISO cleanroom standards indicate the maximum number of allowable particles, with diameter equal to $0.1\mu m$, per cubic meter. This number is expressed by power of 10 (e.g. ISO class 4 indicates 10^4allowed $0.1\mu m$ particles per cubic meter.

[7]Means a file in *.doc format, readable with Microsoft Write.

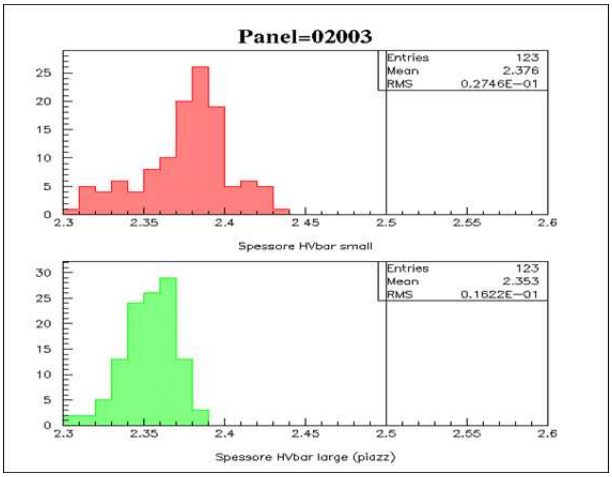

Figure 4.2: Histogram of heights measured for the HV bar Small (up) and for the HV bar Large (down) expressed in *mm* for the panel number 2001. Statistical data are also reported for both HV bars in the right-up side.

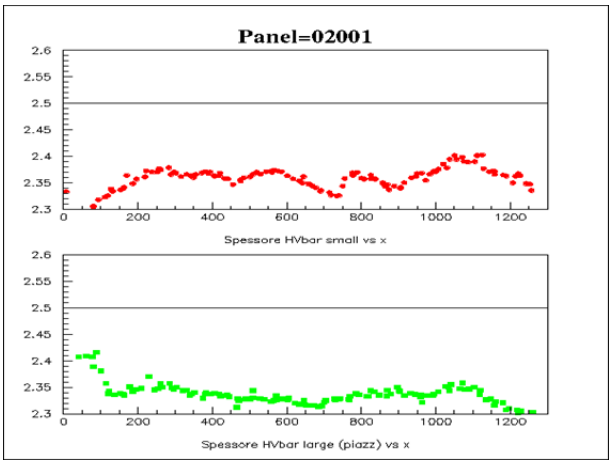

Figure 4.3: Plot of heights vs x coordinate (length) for the HV bar Small (up) and for the HV bar Large (down) expressed in *mm* for the panel number 2001.

Figure 4.4: The cleanroom: assembling table (left) and WGS facility (right) in background, test table (left) and multi-use table (right) in foreground.

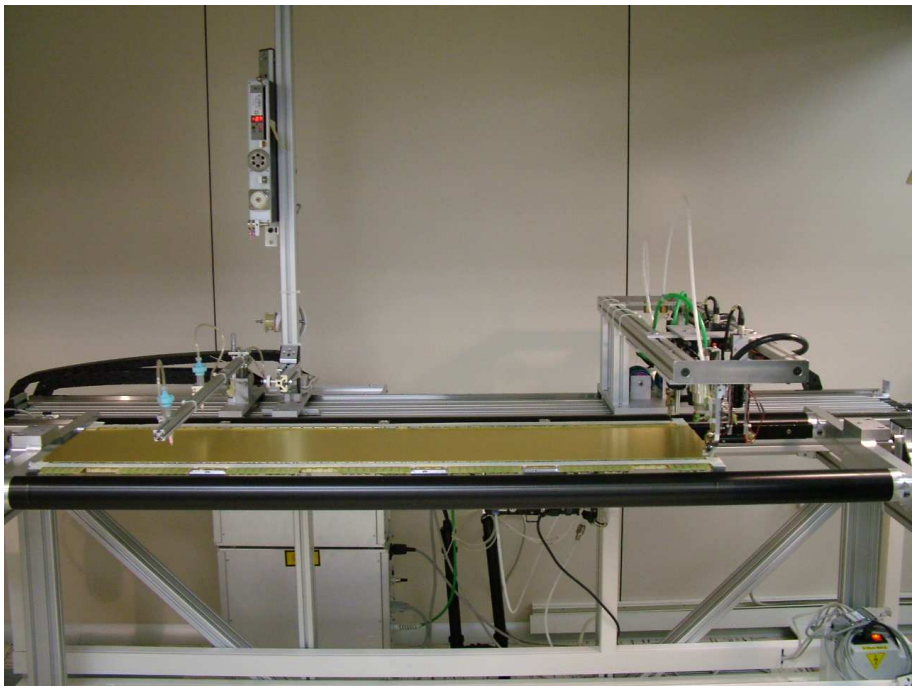

Figure 4.5: The WGS table: a multi-use facility for wiring, gluing, soldering and testing.

4.2.1 Wiring

The total number of wires in the chambers under consideration for the whole experiment, sums up to about 2.5×10^6, with a total wire length of about 1200 *km*. Therefore, much effort has been expended on each production site to develop an efficient and reliable scheme of winding and attaching wires (*NR 3.5.3*). Gold-plated tungsten 30 μm diameter wires provided by LUMA at the nominal tension of 70 g (see section 4.2.5) have been chosen for the MWPCs. A 100 μm diameter guard wire will be used as last (and first) wire to avoid very high fields on the wires at the chamber border.

Once positioned the panels on the WGS machine (see figure 4.5), the first operation is to align them on the wiring rotating frame. Both frame's sides have equally spaced grooves used as guidelines for the wiring operation. To be sure about the correct alignment we refer to the first and last (on both HV bars) soldering traces over the panel: a 'gauge' wire is positioned inside 2 couples of predetermined grooves and then the operator checks the correct position to the traces by naked eyes.

Before starting the wiring we have to be sure about correct semi-gap height over the whole panel (*NR 3.5.6*). This operation is performed using a rectified steel bar (with micron precision) and a calibrated wedge. The bar is positioned

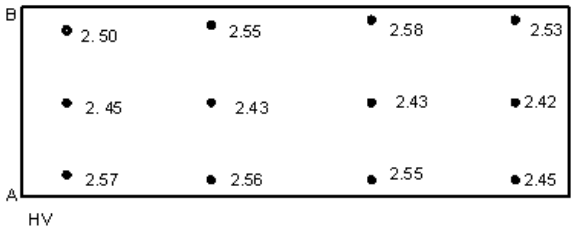

Figure 4.6: Sample of a semi-gap height measure, values are expressed in mm, letters A and B indicate the side of the panel.

between predetermined positions across the two grooved sides of the frame, while the wedge slides under it over the panel surface stopping on a precise position. This position is the measured height on that point, the correct value can be determined referring to the calibration lines over the wedge[8] (*NR 3.5.10*), and then the values are registered on the panel's traveler (*NR 3.2.1*). A set of measure consists of 4 or 6 columns of points (depending on the length of that kind of panel) with 3 points on each column.

Due to the defective flatness of the panels or to an imperfect positioning on the frame, sometimes happens that the measured height is out of the required specification of $2.5 \times 10^3 \pm 100\mu m$. Using the calibrated screws where the panel is fixed on the frame (near the points of measure) is possible to adjust the semi-gap height obtaining values inside the specifications, the new values overwrite the previous on the traveler and, when needed, a special remark on the flatness quality of that panels is written. In figure 4.6 is shown a sample of semi-gap height for an M5R2 panel as reported on its traveler.

The described procedure has been introduced only in the middle of 2005, as an improvement of the semi-gap height measurement. Previously this measure was performed using a 'probe' wire instead of the rectified bar, and a set of Johnson gauges with different thickness sliding under the wire; height corrections were made using spacers up or down the panel's holders on the frame. The old procedures were extremely time wasting and also the measurement precision was largely affected by errors, mechanical corrections have been planned and then executed (*NR 3.6.2, 3.6.5*) , and the procedure manual inside the cleanroom has been updated (*NR 3.2.1*).

When we are sure about the correct positioning of the panel on the frame the wiring procedure starts. The tungsten wire is positioned inside the starting groove and then fixed on the frame by mean of paper-tape. The frame, controlled via PC, starts rotating while an electronic tensioner[9] moves along the rotation

[8]The wedge calibration has been performed using the 'Poli SKY' machine (see section 4.1.2) and all the measures given are registered in a specifical documentation available inside the clean room (*NR 3.2.1*).

[9]Marsilli TEP wire tightener.

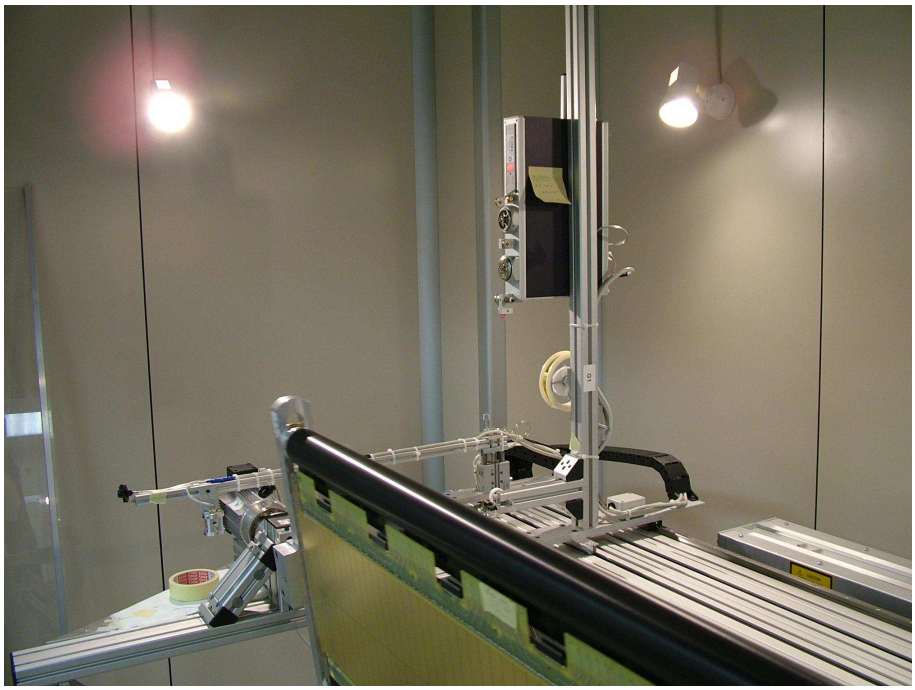

Figure 4.7: Wiring procedure, the frame rotates while the wire is positioned inside the correct grooves.

axis positioning the wire inside all the corresponding grooves over the frame (see fig 4.7).

The nominal wire tension of 70 g is provided by the electronic tensioner using a programmable system of frictions electromagnetically induced, while an additional friction has been adopted besides the wire tightener to reduce the risk of wire break[10]. An overloading alarm prevents from wire breaking, and a digital display shows the real-time tension with a precision of $\pm 0.1g$.

The adopted system of co-ordinate axes ensures a simultaneous correct wire positioning for 2 panels[11] positioned on the two opposite sides of the frame, called side A and side B. Rotation speed can be modified in real-time and do not affect the positioning quality, anyway to reduce the wire-breaking risk and to maintain the overall tension spread under the deviation standard limit of $\pm 3.5g$ (that guarantees a uniform tension distribution along the panel), the maximum recommended (*NR 3.6.5*) value is around 12-14 rpm.

[10] Due to the rotation and to the particular shape of the frame (flat, far from the circular, most stable configuration)

[11] For the M4R2 tipe due to their reduced length has been possible to wire 4 panels at the same time.

4.2.2 WPM (Wire Pitch Measurement)

After the wiring of the whole panel the stepping motor is stopped, the frame is positioned horizontally, and the Marsilli is sent back to the home position. A third independent motorized axis moves along the rotation axis but starting from the opposite position regarding to the Marsilli (fig. 4.5). Here a video cameras system (*NR 3.3*) sensitive to the infra-red spectrum allows the wire pitch measurement on the wires.

The system uses two video cameras to capture images of groups of 4 wires coming from the two lateral sides of the panels (near the HV bars) opportunely illuminated by 4 infra-red LEDs. A dedicated LabView program provides an on-line analysis on the captures, separating different contributions in reason of their contrast. By this way, maintaining the same distance between the cameras and the groups of wires and iterating the process, we have the full pitch distribution on all consecutive wires.

This test is fully automatic, the only manual operation is the initial alignment of both cameras on the guard wire (*NR 3.5.10*) , while all the following operations and also the acquisitions are programmed. At the end of the data acquisition, using the dedicated offline analysis tool, all the needed informations about out of specifications wires are available.

For this test required specifications are:

- 95% of the wires at $2\,mm \pm 50\mu m$
- 100% of the wires at $2\,mm \pm 100\mu m$

when one or more wires are found outside these specifications, they are localized and then moved manually to the correct position before the gluing (*NR 3.6.5*). A common reason for a displaced wire can be some dust inside a groove or an HV bar surface imperfection that touches the wire not allowing the correct positioning. By the way, from the WPM point of view, only few panels showed serious problems and the on-line software allowed to solve these problems quickly.

Here in figure 4.8 is shown a typical capture from the WPM, these captures are analyzed via PC and the results are shown separately with an on-line software (PC screenshot on figure 4.9). At the and of the test those data are re-analyzed with an offline software which provides the plots is figure 4.10. Plots are successively saved into the database with the values of mean and RMS that are also registered on the panel's traveler (*NR 3.2.1*).

4.2.3 Panel gluing

Wires are glued to the wire fixation bars (HV bar) before soldering. This procedure guarantees that the wires are kept in place with a fixed height with respect

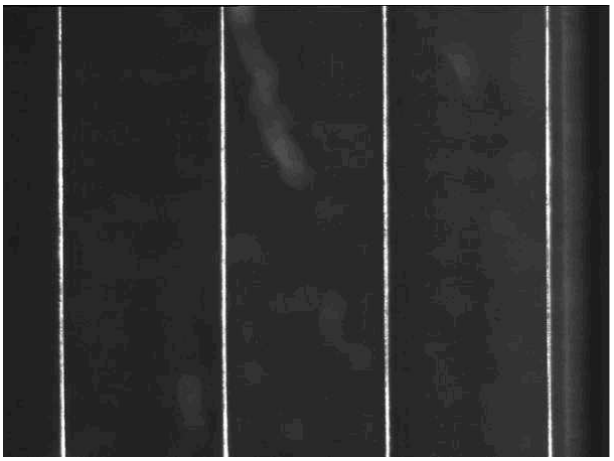

Figure 4.8: A typical infra-red capture in the WPM.

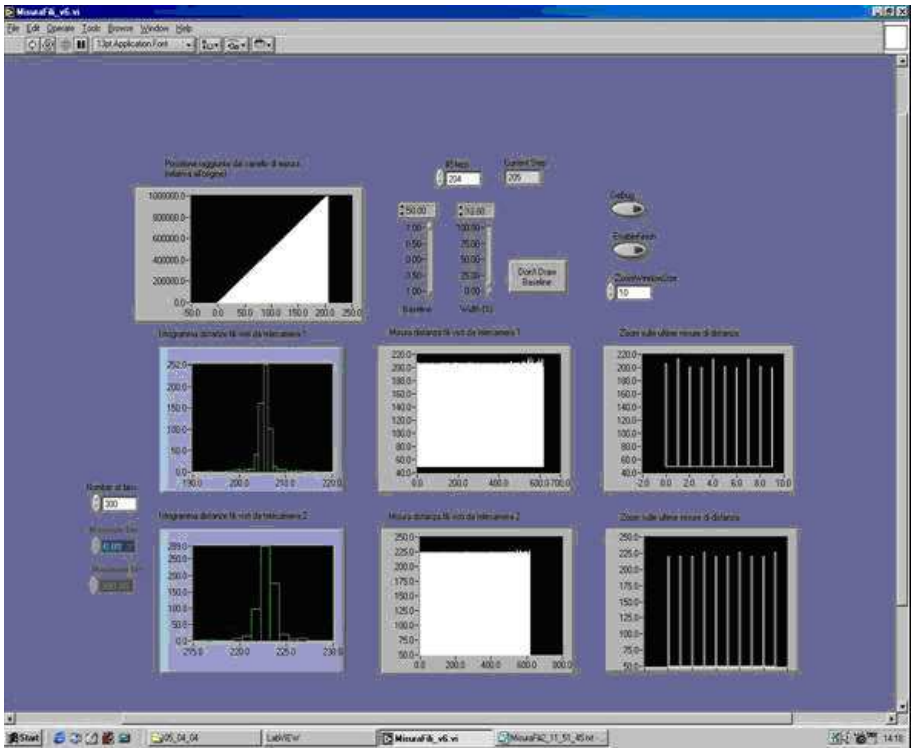

Figure 4.9: On-line software for the WPM. We can monitorize on-line: a)the group of wires in measure, b)the histogram of measured pitch (camera 1 and camera 2), c)all the pitches measured at that moment (c1 and c2), d)the last 10 measured pitch (c1 and c2).

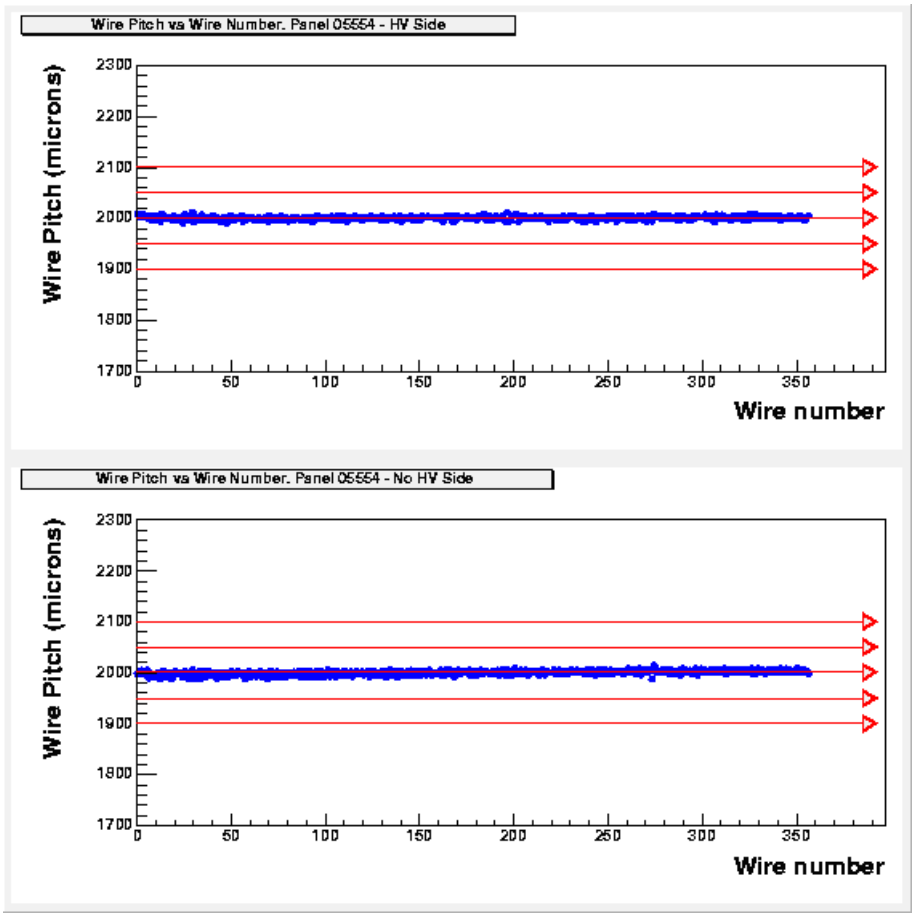

Figure 4.10: Offline analysis plots for both the cameras, red lines indicate the ideal pitch (center) and the two couples of test thresholds for the 95% and the 100% of the wires.

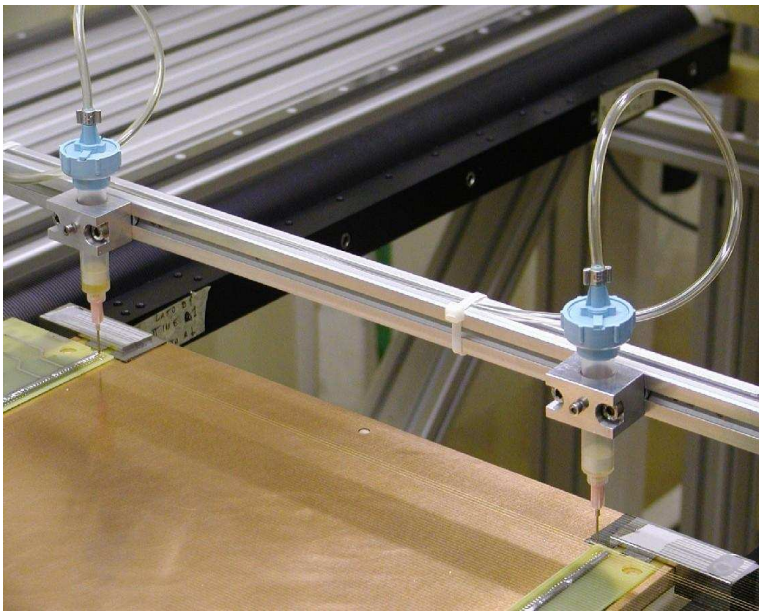

Figure 4.11: Gluing procedure: the glue, coming out from the syringes to the HV bar glue grooves, fixes all wires on the panel.

to the cathode plane. The gluing also keeps the wire tension to its nominal value (*NR 3.6.2*). The chosen glue is the transparent epoxy Adekit A145 which takes 16 hours to fully polymerize at room temperature.

As shown in figure 4.11, the gluing is provided using two 6 *cc* syringes with variable amount of glue inside, depending on the kind of panels to be glued on the frame at that moment. A system of vacuum and compressed air, manually adjustable, ensures the correct glue flux through the syringes. The nominal pressure in use is 3 *bar*, but usually this value has to be modified in reason of the current glue fluidity and consequently considering the instantaneous flux of glue during the gluing procedure. Two manometers are located on the WGS facility, and two pressure controllers can control the flux of the two syringes separately[12] (*NR 3.3*).

The two syringes are hold ed on an horizontal bar connected to the same motorized axis used for the wiring procedure, motion speed and gluing ON/OFF switch are controlled via PC. Two 20 W lamps behind the syringes are turned on 60 seconds before the gluing fluidifying the glue inside the syringes, and then they remain ON during all the gluing procedure aiding to accelerate the polymerization process (*NR 3.6.2*).

The gluing procedure takes from 10 to 15 minutes, at least two trained

[12]Initially only a controller and a manometer were used, but subsequently, in order to improve the quality of the gluing process, a second controller (with manometer, and vacuum controller) has been implemented. (3.7.1)

operators (*NR 3.4*) are needed (the first controlling the procedure via PC, and a second checking the gluing quality on the WGS table in real-time and adjusting the flowing pressure if needed). The glue flows outside the syringes into a specific groove on the wire fixation bar, at the end of this process the glue switch is set to OFF, the motorized axis is sent back to 'home' position and the lamps are turned OFF. A visual check of the gluing quality is performed by both operators and, if needed somewhere along the panel, some more glue can be added manually.

Due to the excessive amount of time needed for the glue fully polymerization, a system of two heating bands has been implemented (*NR 3.6.2, 3.6.5*). Those particular bands are screwed on the frame along the glue line over both the wire fixation bars. The distance between the bands and the glue is approximately 0.5 *cm,* the temperature can be set using a controller on the WGS table, and the heating is provided in a two-step way, initially with a 20 minutes $40°C$ session and then with a $80°C$ 30 minutes session. During the first 20 minutes the heating effect on the glue is checked continuously to avoid an excessive glue flowing that could reach the soldering traces; after that time the glue stops flowing and starts hardening, then, after 30 more minutes, it's enough hard to rotate by 180° the frame (still heating from below at a typical $30°C$ temperature), and the gluing process on the other panel begins.

All the crucial informations about gluing and heating time, operators involved and problems eventually occurred are registered on the panel traveler (*NR 3.2.1*).

4.2.4 Soldering process

After the second heating session is completed the frame could be rotated by 180° more, the up heating bands are removed and the first 'glued' panel is now ready for the wire soldering process. One of the cleanest soldering methods is the use of a laser beam. Due to the large number of soldering involved in the construction of LHCb MWPCs, the use of an automated and reliable method is mandatory (*NR 3.3, 3.5.1, 3.5.3*).

An automatic soldering station provides the tin distribution over the soldering traces behind the glue (Figure 4.12) while a diode pumped laser beam solder it to the wires. The two light source used are two 805 *nm* diode pumped lasers at the 55% of their maximal power (25 W) (*NR 3.5.10*). The setup consists of the same stepping motor used for the WPM with the same cameras, the laser is mounted together with a solder dispenser system (see Figure 4.13) and the whole procedure is controlled via PC.

Due to the large power used for the laser beams and its consequent biological risk, during the whole soldering process no operators have to be present inside the WGS facility, black curtains are used to 'optically' isolate this particular process from the rest of the clean room while an interlock system prevents from starting the soldering with an incorrect optical isolation (*NR 3.3, 3.4*).

The tin in use is a special alloy provided by Almit (280°C working point) with low flux content. The global time for a complete soldering takes from 40 to 70

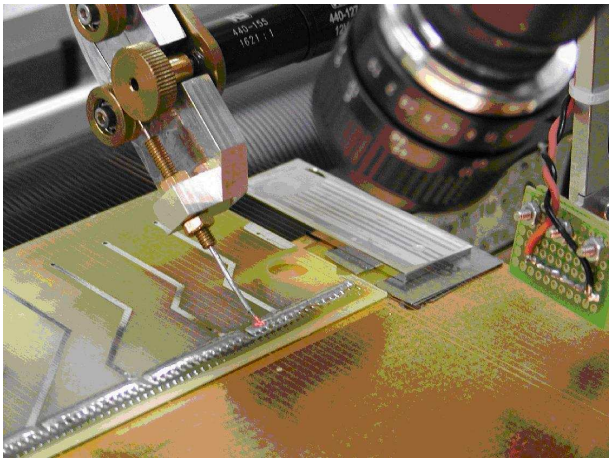

Figure 4.12: Soldering: the tin distributor and the laser beam guide light.

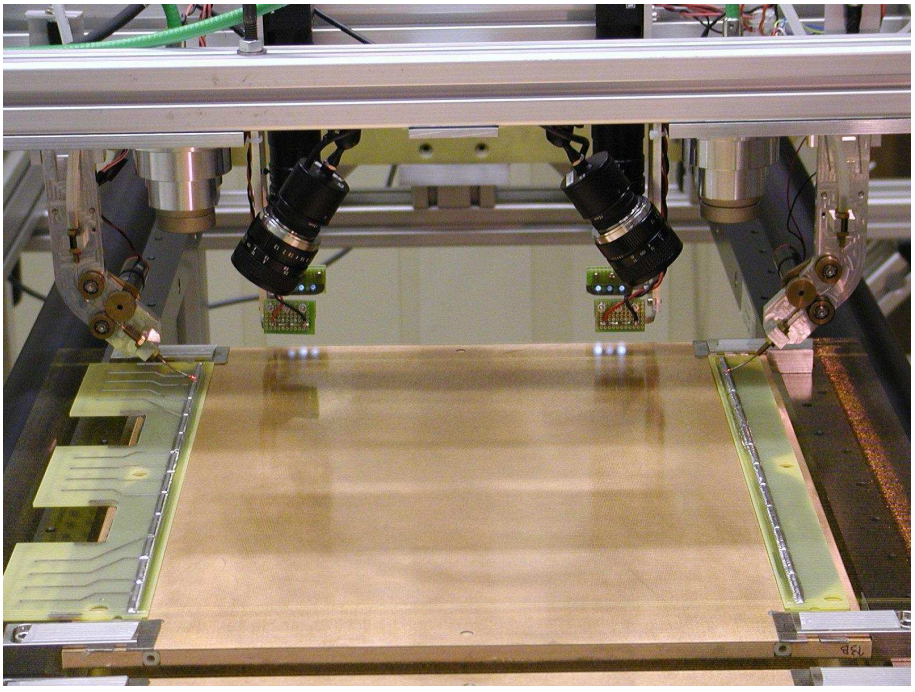

Figure 4.13: The soldering system: tin distributors, cameras and lasers.

minutes and the positioning of the tin distributor to each soldering trace is fully automatic (pre-programmed via PC) and varies for different panels typologies.

Operators are allowed to work inside the WGS facility to set the correct positioning of the tin dispensers on the first traces (*NR 3.5.10*): once positioned the step motor at the soldering starting point, a diode light guide provides a reference point (the laser light is switched OFF); a plexiglas cover protects the active surface of the panel from undesired tin splashes and, after closing the black curtains, the automatic soldering can start.

A Visual Basic program registers the starting point and calculate the correct position for switching ON and OFF the laser beams, motion speed and tin quantity dispensation are programmable but usually not modified during the soldering process. Real time images coming from the cameras positioned on the support above the tin dispensers are shown on the PC screen allowing a constant monitorization of this process. An emergency (*NR 3.3, 3.4*) shut down button allows to stop the soldering procedure anytime for any reason, and, after the needed corrections or checking are made, the process can be easily restarted from the following soldering trace.

Solderings quality is in general very good, but sometimes they needs to be refined manually. This operation is made still on the WGS frame, to ensure that the correct wire tension is still present (*NR 3.6.3, 3.6.5*). After this operation the panel is ready, and the frame is rotated by 180° to perform the soldering process on the second panel. Then, when the second soldering process is completed, wires are cut with specific scissors behind the soldering traces (with the plexiglas cover still present on the active zone), panels are unscrewed from the frame and ready to be removed.

Soldering start and finish time, soldering refining and related operators are registered on the panel's traveler (*NR 3.2.1.*).

4.2.5 WTM

Measurements made during the design period of the MWPCs[43] for the LHCb experiment showed, as can be seen in Figure 4.14, a linear dependence of the elongation on the weight applied up to 140 g. At the baseline wire spacing of 2 mm and with nominal HV of 2.65 kV, the wires become electro-statically unstable if there tension is below 30 g[43]. With these considerations the chosen baseline wire tension and its spread is $70 \pm 20g$.

Considering the very large amount of MWPCs, and then of wires to test, an automatic method that can perform fast and precise wire tension measurements was mandatory (*NR 3.3, 3.5.3*). The system, developed[44] by Ferrara, Florence and Tor Vergata INFN and CERN LHCb groups, is based on commercial components and does not require any electrical connection to the wires or electric or magnetic fields: the wire fundamental frequency is excited by a very short mechanical hit and the induced vibration is detected by a laser based optical system.

The mechanical hit is provided by a simple mylar strip hammer with a vibration induced by a commercial push type DC-pulsed latching solenoid. A

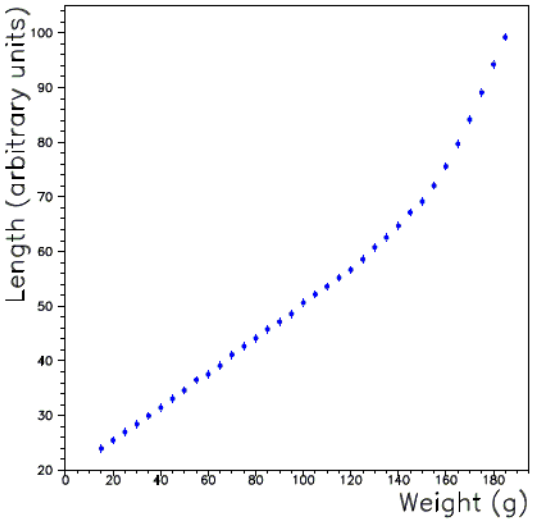

Figure 4.14: Wire elongation as a function of the Weight (g).

light beam, generated by a 3 mW, 635 nm laser diode, is directed onto the wire, parallel to the wire length. The beam, reflected by the wire surface, forms a ring image on a plane perpendicular to the wire itself. The light is collected by a photo-diode through a focusing lens: the wire vibration is detected by the corresponding light intensity modulation on the photo-diode.

The angle between the beam and the wire plane is approximately 30° (see figure 4.15) in order to avoid the 'noise' light coming from the cathode surface. The signal from the photo-diode is amplified by a simple Hi-Fi amplifier and then digitized in a 16 bit format using a standard PC sound-card. The wire fundamental frequency can be then found by applying a standard Fast Fourier Transform (FFT) algorithm to the recorded signal and a subsequent peak search algorithm.

By knowing the wire length l, the wire fundamental oscillation frequency f_0, and the wire linear density μ, it is possible to calculate the wire tension T, using the following formula:

$$T = 4\mu l^2 f_0^2 \tag{4.1}$$

The test is completely automatic, the laser-photo-diode-hammer system is mounted on a stepping motor controlled support, and the normal setup allows the simultaneous wire tension measurement on two panels. The precision of this test, as shown on its calibration[44] (*NR 3.5.10*) , is better than 0.5%, and the average time of measure takes 3-4 seconds for each wire.

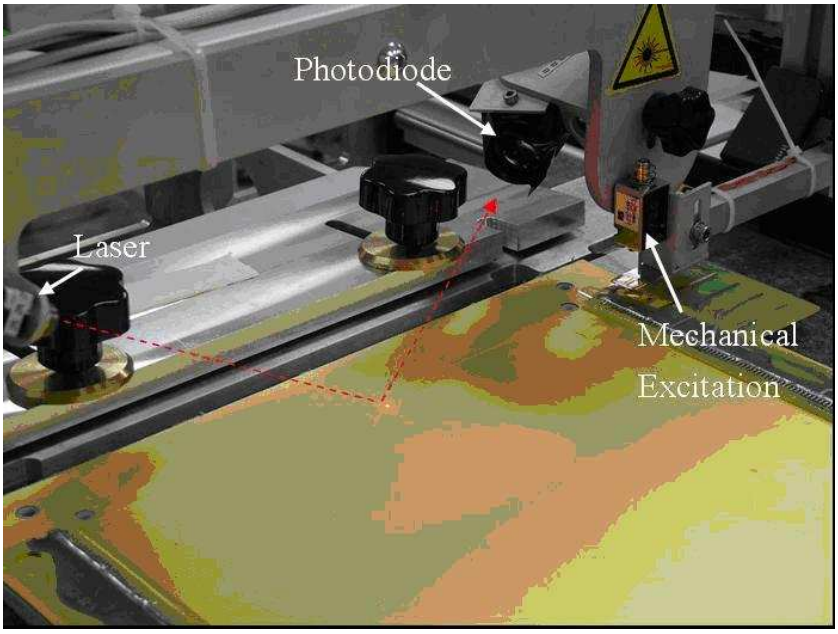

Figure 4.15: The WTM system: a laser beam reflected by the mechanical excited wire surface is collected through a focusing lens by a photo-diode.

The WTM test starts after the correct alignment of the laser spots[13] on the first wire of both panels, a spreadsheet file is written after the first measure and subsequently updated adding each new measure until the last wire is measured. At the end of this measurement the mechanical support is sent back to home position and, running the offline analysis software we have all information about average wire tension, RMS, and wires out of specifications for both panels. Figure 4.16 shows a typical plot for a WTM measurement and a summary histogram with all statistical informations. As usual for each procedure, informations about average tension and RMS, and special remarks about out of specification wires are reported on the panel's traveler (*NR 3.2.1*).

Wires behind the lower limit of 50 g are removed and then replaced manually (*NR 3.4*), wires over the upper limit of 90 g are generally admitted until the 100 g limit. A slightly higher tension is considered not critical for the MWPCs operation and the large amount of time needed for each wire replacing led us to adopt this additional condition (*NR 3.6.2, 3.6.3, 3.6.5*).

4.2.6 Preliminary HV Conditioning & HV Test

Immediately after the WTM, the panels are prepared (see details in section 4.2.7.1) for the last test inside the cleanroom: the dark current (also called

[13] the alignment has to be correct on the first sensitive wire of both panels in measure

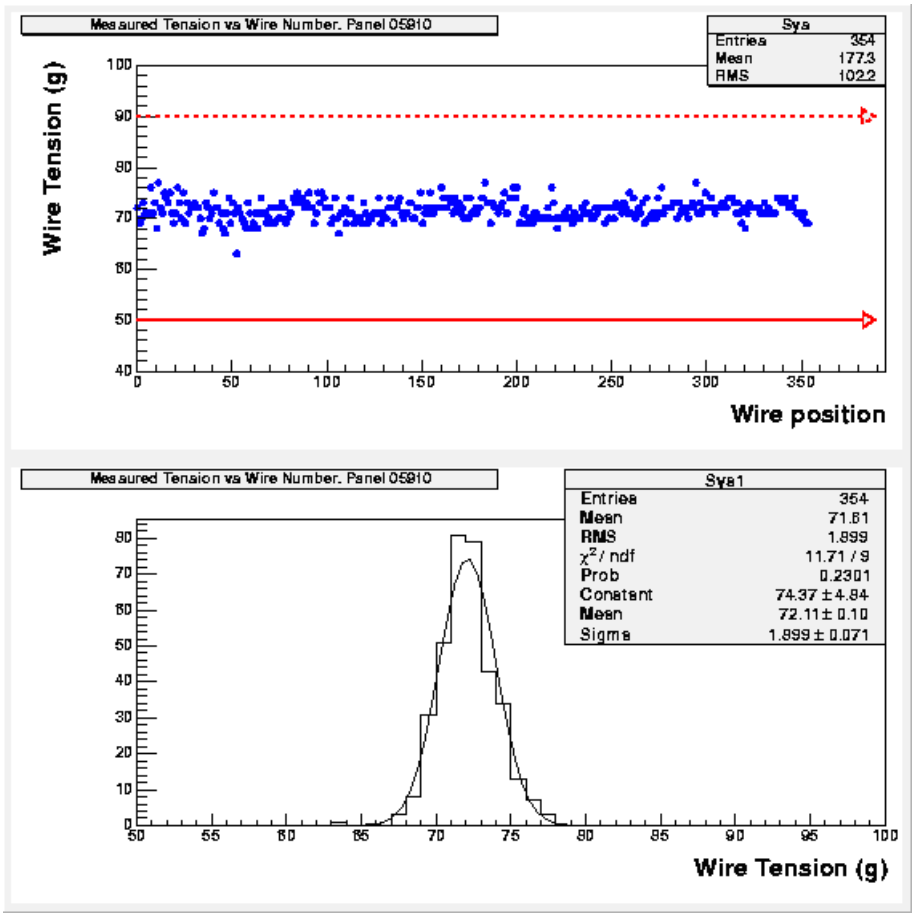

Figure 4.16: WTM analysis: a summary plot (up) indicate the wire tension measured for each wire and the crucial statistical informations, a wire tension histogram (down) shows the wire tension distribution on the considered panel giving a large and detailed statistical report.

HV) 'in air' test. A system of two CAEN N126 HV power suppliers allows the simultaneous test of 8 panels, 2 on the same table used for the WTM, and 6 on a dedicated shelf behind the assembling table (*NR 3.3*).

All the panels in measure are covered with a ground panel and connected to the HV distributor ground using specific connectors. The HV is applied to the wires with the same kind of connectors, connections between ground panel and panel in measure is ensured by metallic spacers used also in the chamber assembling. Side bars and closing bars are temporary positioned between panel and ground panel to ensure the correct distance between cathodes and wires (*NR 3.6.2*).

The nominal HV during this test is set to 2000 V[14], and the specifications require a dark current lower than 10 nA at the nominal HV. The values of 10 nA should guarantee the good operation of the panel, but there are several conditions that may cause an higher current absorption. Dust, wire imperfections or anything between wires and cathodes may cause discharges or abnormal current drawings. For this reason the nominal HV value is reached step by step providing a preliminary HV conditioning of the panel, and a quick panel cleaning with dry air flux is provided after each step if something anomalous is detected (*NR 3.6.3, 3.6.5*).

Some reverse polarization cycles have been implemented in order to help the HV conditioning, this procedure has been used on assembled chambers to solve high current absorption problems and will be described with more details on section 4.3.2.1.

Measured currents and environmental conditions are registered on the panel's traveler (*NR 3.2.1*).

4.2.7 Assembling

To proceed to the final chamber assembling, five panels should be ready: four single sided wired panels (L1, L2, L3, L4) and one ground panel (L5). All the panels are already equipped with lateral side bars, and wire fixation bars while closing bars have to be fixed. Appropriate gas inlets/outlets are designed for each gap (see fig. 4.17) and gas connectors are glued at the end of the assembling. Cylindrical precision spacers are inserted in their appropriate holes around the chamber and the panels are assembled making use of jigs at the four corners. For the final chamber closing the five panels are kept together with screws. The leak tightness is obtained by gluing the five panels together with black epoxy glue.

[14]This value has been decided in order to avoid any discharge or any possible damage that may occur to the wires or cathode during an 'in air' test.

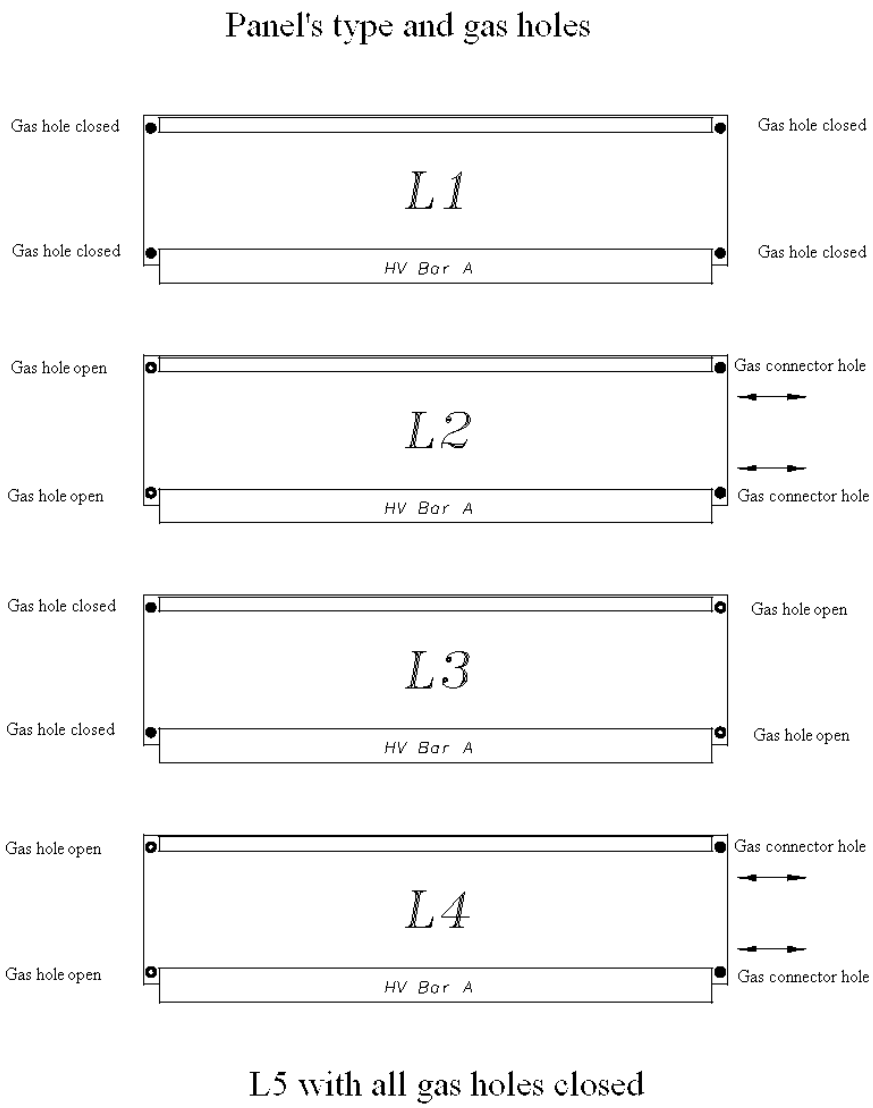

Figure 4.17: Panel types and gas holes distribution for the final assembling.

4.2.7.1 Panels preparation

Once removed from the WGS table, all the panels are subject to different operations, following the scheduled tests, until the chamber assembling on the assembling facility. Most of these operations are performed on the multi-use table mentioned in section 4.2, but some of them are performed on the WTM and HV table in order to minimize the time loss during the whole production (*NR 3.5.1, 3.6.2*).

After the WTM test, panels are moved to the multi-use table, and here, excesses of wire behind the solderings are removed using specific cutters. Due to the effective dangerousness of this operation, the active area of all panels is covered with a plexiglas sheet and a vacuum generator is used to remove small wire pieces that could come inside the active area causing discharges or malfunctions of the final chamber (*NR 3.6.3, 3.6.5*).

After this very important procedure, a mylar adhesive film is used to isolate the external signal traces over the large HV bars. These traces after the final assembling will be outside the chamber and a better isolation will ensure their proper operation on the MWPCs, reducing the risk of external current drawings. HV cables are then soldered on the HV bars as indicated on the MWPC design and the panels are now ready for the HV test in air.

When the HV test is finished (usually at the end of the working day) side bars are glued on the good panels using the black Adekit 140 epoxy glue. Putting the glue into the appropriate grooves over the side bar and at the corners of the HV bars the panel is ready, using some reference jigs the side bar is positioned over the panel where a continuative mechanical pressure provided by grip handles, as shown in figure 4.18, ensures the perfect adhesion.

After 12-14 hours the mechanical pressure can be removed, excess of glue are removed from the corners and the panel undergoes a quick HV test that guarantees nothing changed after last procedure. Now the panel is almost ready for assembling, a temporary shelf (*NR 3.5.8*) hosts all the constructed (and still not assembled) panels. When they are required for the assembling, an operator checks visually each panel and cleans it using first of all a vacuum generator on the active area and then a soft microfiber dust cloth drenched with isopropanol on the unwired side of the cathode.

All of these operations are registered with data, time and operator(s) on the panel's traveler (3.5.1) and the panel is marked as ready for assembling (*NR 3.2.1, 3.5.8*).

4.2.7.2 Chamber Assembling

After the correct panels cleaning the chamber assembling starts. An L1 type panel is placed over the assembling table inside the marked area for the components gluing (see figure 4.19). Side bars are already glued on the panel and they are used as reference for the closing bar length check. After this test an automatic program is used to put the Adekit 140 epoxy glue along the HV bars, 5 mm behind the solderings. Closing bars are then pressed over the glue and

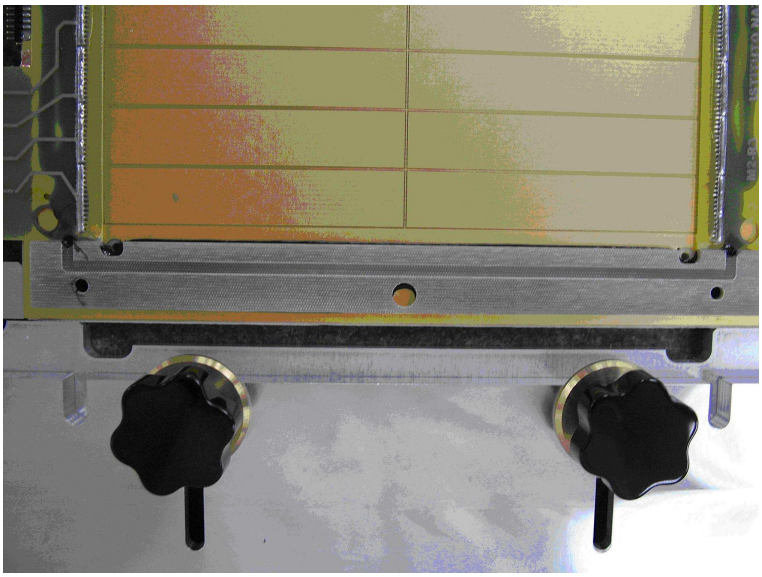

Figure 4.18: Grip handles for the side bar gluing: moved over the lateral bar (here released) they ensure a continuative uniform mechanical pressure.

carefully pushed by hand (*NR 3.4*). Precision spacers are then positioned inside their proper holes along side and closing bars and on the external border of the panel. Few seconds later, the same program used before, allows the glue dispensation along the path (a 2 *mm* deep groove) over the side and the closing bars.

A two axes stepping motor system is used to move a 30 *cc* syringe full of glue over the panel, the gluing speed can be controlled via PC, and a system of compressed air and vacuum controls the glue flux outside the syringe into the glue groove. The air pressure can Be monitored using a pressure controller positioned below the assembling table, and can be modified in real-time by one of the two operators needed for this procedure (*NR 3.3, 3.4*).

After this operation an L2 type panel is positioned over the ready L1 using some reference jigs at its corners, then, a continuous pressure is ensured by the tooling in figure ..., that, using a system of 100 screwed forks, guarantees a uniform mechanical pressure over 32 points at the borders of each assembled panel.

To complete the MWPC assembling this procedure is repeated 3 times (1 time in the case of M1R4) and the last panel assembled is the cover (ground) panel. On the last panel the mechanical pressure is ensured by a system of lead blocks and a steel plate additionally to the screwed fork in order to guarantee the optimal pressure on the whole chamber for a correct glue adhesion (*NR 3.6.2, 3.6.5*).

When finished 4 gas connectors are glued into their proper holes and the

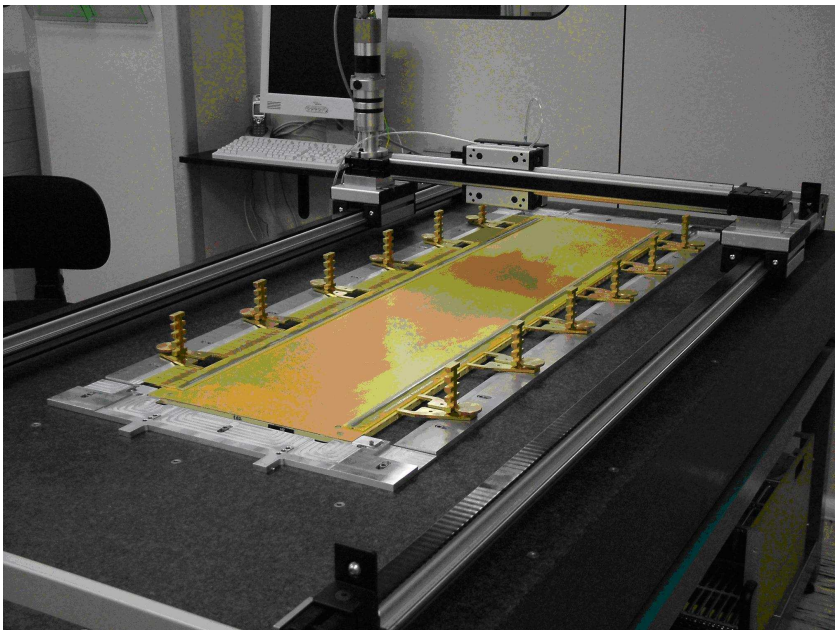

Figure 4.19: Assembling table: a two axes stepping motor system for closing bar and panel gluing.

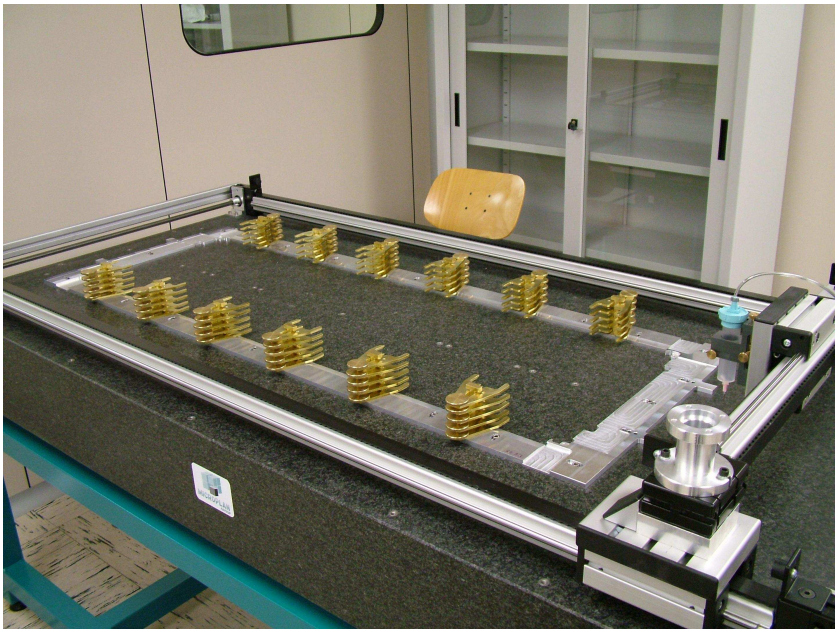

Figure 4.20: Assembling table: mechanical pressure tooling.

chamber is now assembled. Adekit 140 epoxy glue takes approximately 24 hour to fully polymerize at the clean room temperature, before that time the chambers are not removed from the assembling table.

For the M1R4 chambers the assembling rate is approximately 1 chamber/day so, the fully polymerization time cannot be covered. In order to avoid this problem a plexiglas heating box has been implemented (*NR 3.6.2, 3.6.5*). This box can be simply positioned over chamber and assembling tooling while an air heater guarantees a continuous hot air flux inside the whole box. The air temperature is forced continuously between 30°C and 40°C and monitored using a thermocouple. This particular procedure allows to reduce the polymerization time by 30%-50%.

The complete chamber assembling takes about 180 minutes (120 minutes in the case of M1R4) and at least two operators (*NR 3.4*). All the operations are performed using protecting gloves in order to prevent hand contacts with the Adekit 140 glue but also to prevent the active areas of the panels from a bare hand contact after the cleaning (*NR 3.3, 3.6.2, 3.6.5*).

From the chamber assembling beginning a new kind of traveler[15] (the chamber traveler) is used, reporting all critical informations about the panels going to be assembled in that specific chamber, date and time of any operation and operators involved (*NR 3.2.1*). This traveler will follow the chamber in all its future tests, and is shared, like the panel's traveler, between computers inside and outside the cleanroom (*NR 3.5.8*).

4.3 Post-production test

After glue polymerization the chamber is removed from the assembling table, external spacers are removed, chamber corners are screwed and gas connections[16] are implemented to isolate the chamber from open air. The assembled chamber can be then moved outside the cleanroom where three specific stations (*NR 3.3*) are used for the three post-production tests:

- Gas tightness
- Current leak scan
- Gas gain uniformity test

4.3.1 Gas Tightness

The first information needed about the quality of an assembled chamber is the gas tightness. An insufficient gas tightness may cause an inhomogeneous gas composition inside the chamber leading to its consequent malfunction, or an excessive undesired gas loss leading to the consequent economical damage to the final experiment.

[15] An electronic file in the same format of the panel traveler.
[16] Made of plastic rylsan tubes joined by typical gas fillets.

In the Ferrara LHCb site there are two separate gas distribution systems for the post-production tests, the first one, that uses the simpler and cheaper nitrogen molecular gas, is connected to the gas tightness test facility, while the second, that uses the final well known gas mixture $Ar/CO_2/CF_4$ (40:55:5), is connected to the HV conditioning station and to the gas gain uniformity test station.

The nitrogen gas passes through a 3 stages system, from the bottle valve (stage 1) at 200 *bar,* the pressure reduces to 1.5 *bar* at the stage 2 and then, through a bubbling system (stage 3) set to 5 *mbar* over-pressure (referred to the environmental pressure) it goes directly to the in-test chamber.

The test station consist of a reference chamber (of the same type of the chamber under test), a differential pressure digital manometer Thommen HM28 connected to the PC via RS-232 and an on-line software appropriately realized in LabView 6.1 for the data acquisition (*NR 3.3*).

The reference chamber has been externally sealed with Adekit 140 glue to ensure its perfect tightness, and periodically checked (*NR 3.5.10*) to ensure the reliability of this test. The choice to use a perfectly sealed chamber instead of any equivalent volume with a different shape has been taken due to the mechanical deformation of the chambers, when the 5 *mbar* overpressure is applied. Those deformations are not easily predictable and strongly dependents from environmental pressure and temperature. To ensure the correct reliability of the test, a waiting time of at least 60 minutes[17] before the test beginning has been established, and both chambers (reference and testing) are placed on the same table, one next to the other, in order to minimize any temperature inhomogeneity between them (*NR 3.3, 3.4, 3.6.2*).

During the waiting time both chambers are under nitrogen flux, both with inlet and outlet open. When the test starts the chambers are connected together with the gas outlet closed, then a bubbler ensures the 5 *mbar* overpressure for both chambers. Subsequently the gas outlet is closed, isolating each chamber from the other and from the gas system, while the digital manometer, connected between the two chambers, starts sending informations about their relative pressure (see figure 4.21).

The instrument precision is ± 0.01 *mbar.* Data are registered on a spreadsheet file at programmable intervals from 10 second to 24 hours, but the usual acquisition width is 1 hour with an acquisition every 5 minutes. When the acquisition ends, registered values are copied on an excel file and then plotted looking for any discontinuity or unexplained values. If nothing irregular is found, the same values are registered on the chamber's traveler and the chamber is ready to be connected to the gas mixture distribution system (*NR 3.2.1, 3.5.8*).

Due to any unfound structural imperfection on a panel or to any error during the assembling process it can happen that some chamber exceeds the specified limit of 2.00 *mbar* leak in 1 hour. In those cases chambers are recovered using some conformal coating[18] externally to the chambers along the suspected leaking

[17] In order to reach a sufficient thermodynamic equilibrium.

[18] Conformal coating material is usually applied to electronic circuitry to act as protection

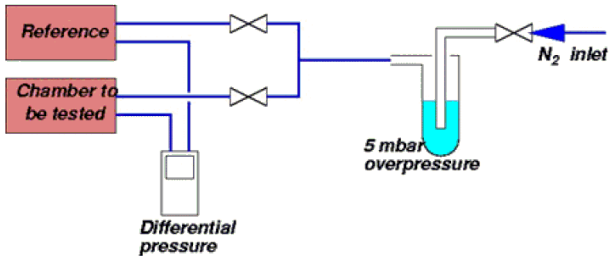

Figure 4.21: Gas tightness test system.

area. The leak search is performed trying to inject compressed air from outside the chamber into any possible leaking point and looking for pressure raisings on the digital manometer still connected to the chamber. When one or more leaks are found the incriminated area(s) are recovered, and, after 1 day spent waiting the conformal coating hardening, they are retested. The test restarts and the new measured values overwrite the previous on the traveler while a special remark about the recovering procedure made is registered (*NR 3.2.1*).

4.3.2 HV Test

Once the chamber passed the gas tightness test, it's ready to be connected to the gas system. Also this second system has different pressure stages, from the very high value (stage 1) on the bottles (usually varying for each kind of gas), to 1.5 *bar* on stage 2, through a Bronkhorst mass flow meter (stage 3) to the mixer and then to the chambers through a flux controlling valve (stage 4).

The number of simultaneously fluxing chambers is 8 in parallel for the HV test plus 2 or 3 in series for the gas gain uniformity test (made in dedicated room), and there's an additional gas line with premixed gas, used independently from the other line.

The chambers voltage is provided by two N470 CAEN modules, one in positive (regular) polarity and the second one in negative (reverse) polarity, each one with 4 working channels. Current values are monitored using the SELF (Servizi Elettronici Laboratori Frascati) I-meter with 16 working channels and its dedicated software Opera (*NR 3.3*, *3.5.9*).

During the HV conditioning and the current leak scan the chambers are located on a dedicated 4 floors station (see figure 4.22) on which the final gas distributors are fixed, next to two crates hosting the N470 modules and the I-meter. Each chamber is supplied by a single N470 channel, while 4 channels of the I-meter read separately the absorbed current on each gap from the under

against moisture, dust, chemicals, and temperature extremes that if uncoated (non-protected) could result in a complete failure of the electronic system.

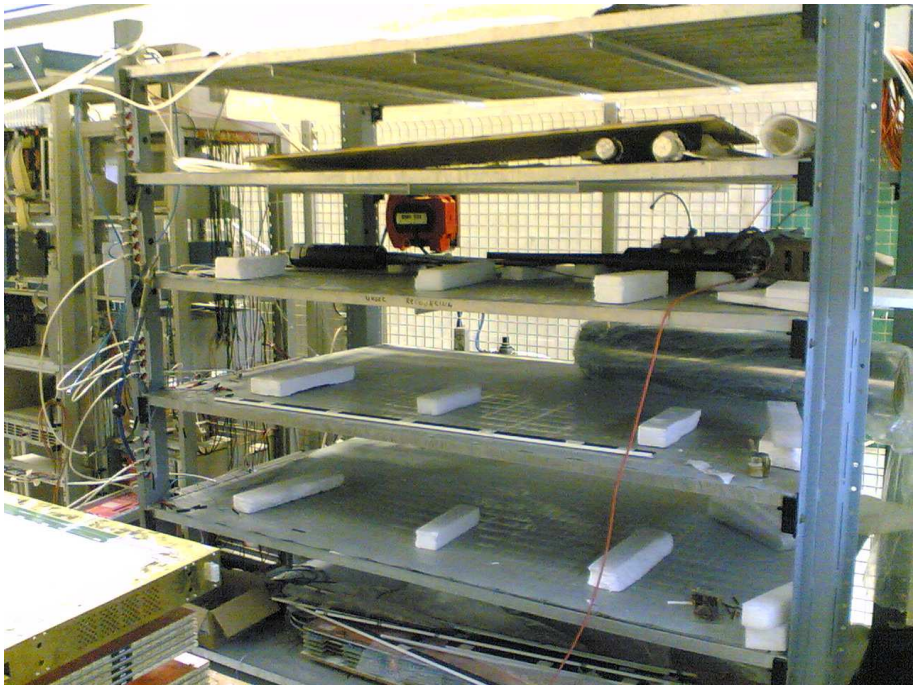

Figure 4.22: HV test station: up to 8 chambers in test at the same moment.

test chamber.

4.3.2.1 HV conditioning (direct and reverse polarity)

The first critical informations about the true reliability of a MWPC in operational conditions is given by the HV conditioning.

At least 3 changes of volume with the proper gas mixture are mandatory, then the voltage applied between cathode and wires is increased manually step by step starting from zero (0V, 500V, 1000V, 1500V, 2000V, 2250V, 2500V, 2650V, 2750V, 2800V, 2850V) until 200V over the operational tension, while absorbed current on each gap can be monitored on real-time using the opera software (see figure 4.23). The current absorption limit is set to $1\mu A$ (*NR 3.3, 3.4*).

Usually the chambers under conditioning don't show particular problems until 2600V, but after that value measured dark currents start becoming unstable, sometimes very high (over 300-400 nA on a single gap) current are registered, and higher tension values are not reachable quickly.

Dust inside the chamber, wire imperfections, small tips may cause those unexpected noise. After few minutes the measured current tends to decrease

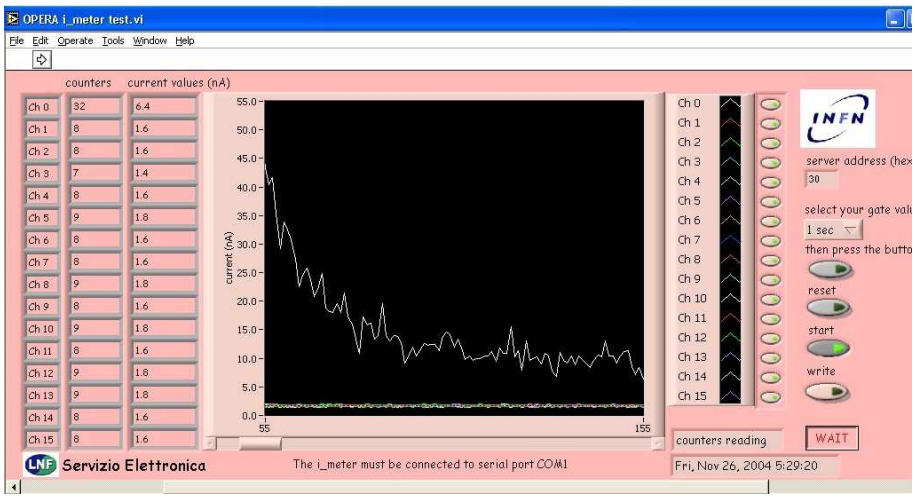

Figure 4.23: Opera software: 16 gaps can be monitored simultaneously, different colors indicates different channels, current is shown in nA, refresh time is 2 s.

and the voltage can be increased, but the problem usually re-appears at the following step and the time needed to recover it starts to be not negligible.

A very clever way to avoid this problem is to apply a reverse polarity, using the wires as cathodes and the proper cathodic plate as anode (*NR 3.6.5*). The principle is to smooth the wire surface (very sensitive to any imperfection into the gas multiplication regime) bombing it with heavy ions instead of light electrons.

The procedure is similar to the HV conditioning with regular polarity, the voltage limit has been set by the LHCb collaboration to -2350V to avoid any damage to the wires, tension steps are slightly different (0V, -1000V, -1500V, -2000V, -2100V, -2150V, -2200V, -2250V, -2300V, -2350V) and it's not needed to reach the upper limit for a complete reverse training. Also here the current absorption limit is set to $1\mu A$ (*NR 3.3, 3.5.3, 3.6.5*).

Usually in reverse polarity what we observe is an unstable current after -2000V/-2100V, with measured currents around 100 nA decreasing with variable time. The time for a complete reverse training takes from 60-90 minutes (most cases) to more than 24 hours (only on rare cases with serious problems). During the short time trainings all the lower tension steps are reached easily, and most part of the time is spent between -2250V/-2300V waiting for a current stabilization while wire surface is smoothed using an enough intense electric field. Long time trainings are usually performed at safer conditions, applied tension rarely exceeds -2200V for long periods (more than 3/4 hours) and sometimes higher voltage values are not reachable at all.

4.3.2.2 Current Leak scan

At the end of the reverse training the chamber is ready for the current leak scan. The principle for this measurement is the same that for the HV conditioning (fixed voltage steps, waiting for current stabilization) but each information is registered on an excel file using a file for each chamber. Screen captures from the acquisition software (Opera), time needed to stabilize the current, environmental informations and any kind of special remark are registered on this file (*NR 3.2.1*).

Any information about the history of the chamber can be very useful during the long road of different test until the final installation on LHCb detector, so all of these files are saved in a specific database for any needs (*NR 3.5.8*).

Specifications for this test require a dark current below 100 nA at 2850V. The value of 100 nA is taken considering the whole chamber, so, each gap contribution is considered and their sum is confronted to the reference value. The choice to test the chambers at a so high tension has been taken considering the estimated working life of those chambers. They have to be operational for at least 10 years, and, any initially negligible imperfection or any hidden problem could become easily a serious unsolvable problem few months or some years later. Testing the chambers 200V over the operational tension will seriously improve their quality amplificating any hidden problem that can be, by this way, investigated before the final installation (*NR 3.3, 3.5.3, 3.6.5*).

Opera writes a spreadsheet file updated every 2 seconds, the I-meter sensitivity is 0.1 nA, and the measure at 2850V is taken after a 30 minutes waiting time for current stabilization. The final considered value takes the sum of average measured dark current on each gap over 1 minute of acquisition time. This final value is registered on the chamber's traveler with the current environmental informations (temperature, pressure, relative humidity).

When a chamber does not satisfy the required specifications is usually subject to an additional reverse training cycle and more carefully investigated, each information is registered on the chamber's traveler as special remarks (*NR 3.2.1, 3.5.8, 3.5.10, 3.6.3, 3.6.5*).

4.3.3 Gas Gain Uniformity test

Before the shipping to LNF, where the external electronic components and the Faraday cages will be mounted, the produced chambers must be inspected for uniformity in their response with respect to the others chambers. The gas gain uniformity of each double-gap is evaluated on the strength of the following criteria (need to be valid in the 95% of the total area):

$$\text{class A:} \qquad \frac{< G >}{\sqrt{2}} \leq G(x,y) \leq \sqrt{2} < G > \tag{4.2}$$

$$\text{class B:} \qquad \frac{< G >}{\sqrt{3}} \leq G(x,y) \leq \sqrt{3} < G > \tag{4.3}$$

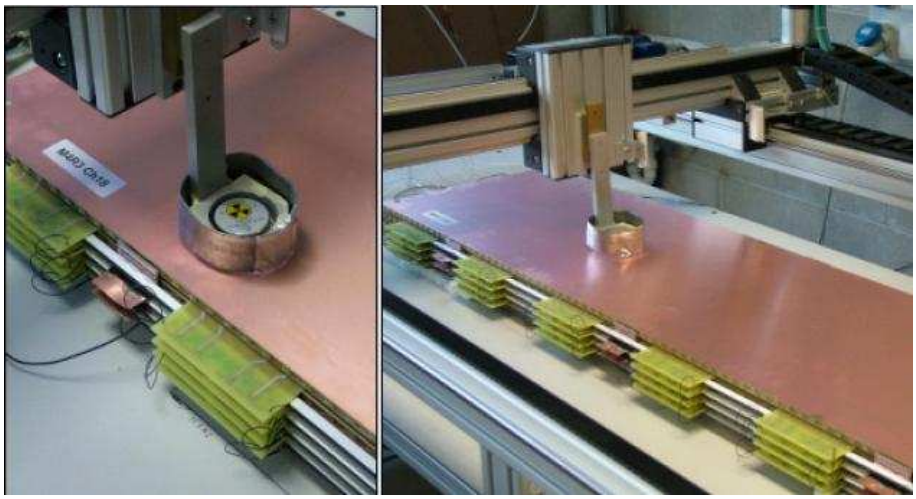

Figure 4.24: The source moves over the fixed points on the chamber, distance from chamber surface is 5 *mm*.

class C: all the other cases

where *G(x,y)* is the gas gain of a gap in the *(x,y)* position and $<G>$ is the average gas gain over all the gaps of the same type. The requirement is that the full chamber is classed as AA or AB (good). The range of the above criteria corresponds to a voltage range equal to $\Delta V = \pm 53V$ (class A) and $\Delta V = \pm 84V$ (class B). The requirement ensures that all the chambers exhibit a similar gain response and therefore will be operated well inside the region of full efficiency.

Since the gas gain is proportional to the current drawn by the gap, the gas gain uniformity is normally measured making use of a radioactive source and monitoring the current drawn by the chamber. The current drawn by each gap is monitored while the lead case containing the source is moved along the surface of the chamber. These measurements allow to check the gain uniformity within each gap and to compare different chambers among them.

The radioactive source used for this test in the Ferrara site is a ^{90}Sr source emitting 0.546 keV β^- electrons, with an estimated activity[19] of 19 Mbq (see figure 4.24).

The system consists in a table for the housing of 2 or 3 chambers (depending on their length) above which two motors move the lead case containing the

[19]The last measured activity (N_0) for the testing source was 33 Mbq during the year 1983, by knowing the half-life time ($T_{\frac{1}{2}}$= 28.8y) for the ^{90}Sr is it possible to use the well know expression $N = N_0 e^{-(0.693t/T_{\frac{1}{2}})}$ to estimate the current activity (N). 19 Mbq is the estimated value for the year 2006.

Figure 4.25: The gas gain uniformity test table: motorized system (green arrow), and HV supplying system (red arrow)

source along the x and the y direction, while a CAEN SY546 HV distributor with 8 CAEN A548 twelve channels modules supplies the HV for the chambers (see figure 4.25).

A dedicated gas line provides a maximum flux of 3 l/h and three changes of volume for each chamber are mandatory before connecting the chambers to the HV system (*NR 3.3, 3.4, 3.6.5*).

A custom LabView software controls the x-y motion via RS-485, allowing to position the source over many different points across the chamber surface. The same LabView software controls the CAEN A547 module controller via RS-232. Measured currents, tensions and channel status information can be read (or modified) via PC (see figure 4.26).

This particular 'training program' is used to reach the testing tension of 2750V and to verify the correct conditions inside the chamber to start the automatic test. Each gap corresponds to a specific channel, and the starting conditions require all measured currents below 10 nA with the source out of the table.

A dedicated LabView software monitorizes temperature, pressure, and relative humidity inside the testing room (see figure 4.27). A RS-232 port connects the PC to a Thommen HM30 digital meter, and all the environmental data are

Figure 4.26: Training Program: nominal voltage, current limit and channel status can be modified while monitored current and voltage can be read on-line using this program.

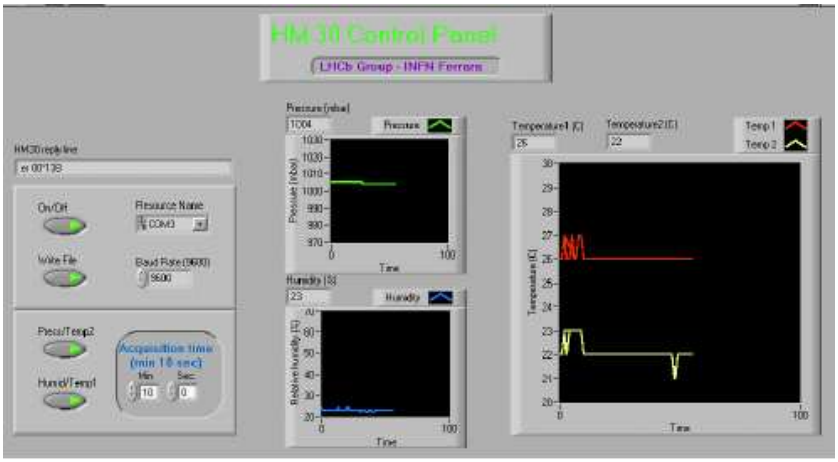

Figure 4.27: Environmental monitoring software: 2 temperature gauges, 1 pressure gauge and a relative humidity gauge located in different points within the test room are used to monitorize the environmental parameters.

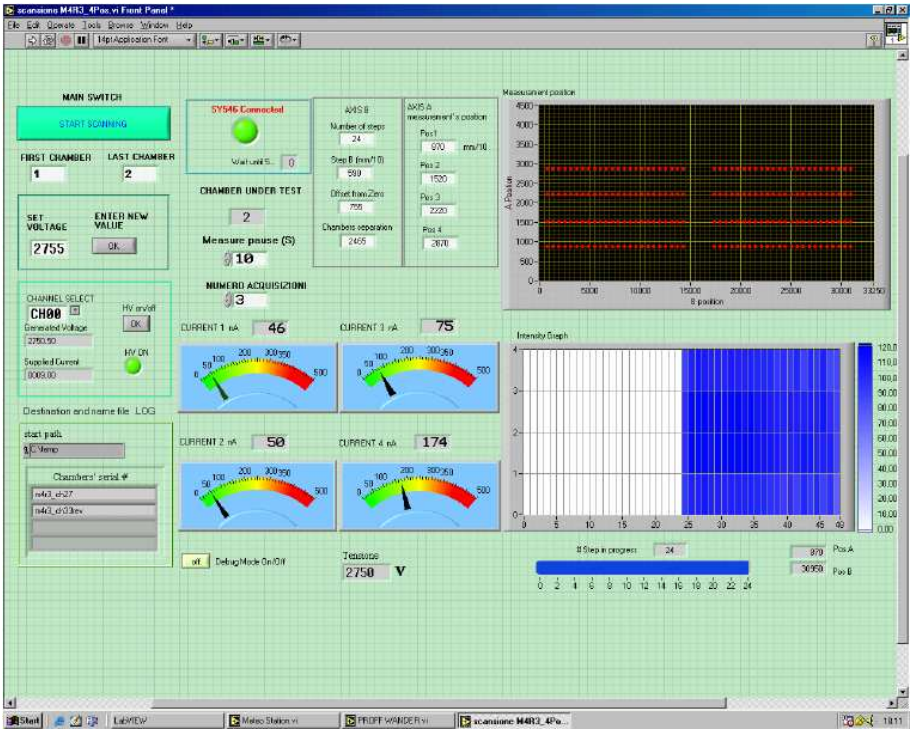

Figure 4.28: Automatic gas gain uniformity test program: measured currents, chamber position and HV supplying informations are available on-line, while number of acquisition per point and waiting time between two consecutive measurements are easily adjustable.

registered electronically on a spreadsheet file and manually on a logbook (*NR 3.2.1, 3.3, 3.6.2*).

When the chamber is ready the training program is closed and the automatic program (see figure 4.28) starts. Information about type, id number and position of the chamber on the table must be entered by the operator, the source can be placed on its lead case with a 5 *mm* distance from chamber surface facing the first[20] gap, and the measurement starts (*NR 3.4*).

First of all a dark current measurement is performed, then, the program, connected to the four chamber gaps, records the current absorbed value for each gap. Four measurements equally distributed along the wire are performed for each line and a set of 12 or 24 lines (depending on the chamber type) completes the full test for a chamber.

The automatic test is performed subsequently also on the reverse side of the chambers (with the first gap facing the table and the fourth facing the source). Measured currents for each test are reported on spreadsheet file and then copied

[20]Conventionally the first gap indicates the gap between L1 and L2 panels.

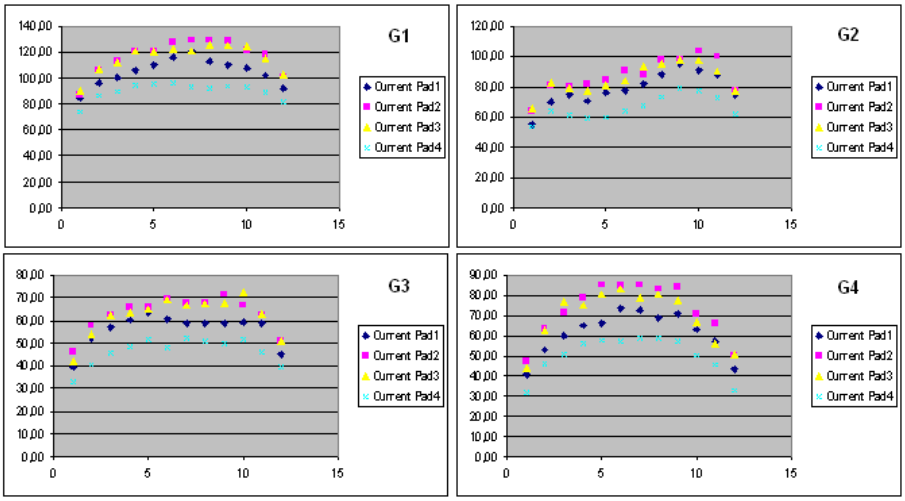

Figure 4.29: Sample of a gas gain uniformity measurement: each plot indicates data from a single gap (G1,G2,G3,G4). Measured average current (nA) vs line number point (12 or 24 in total) and different colors for different points along the same wire measured show the full grid of points for a chamber.

to an excel file where they are re-arranged in a different shape. Regular (also called 'top') and reverse test informations are joined in the same excel chamber file, a single sheet is used for each gap considered, 4 columns of 12 or 24 points are considered separately and plotted together evidencing abnormal gas gain points over the chamber (see figure 4.29). Reverse test results from the analogous gap (the fourth, first referring to the source) are analyzed on the same sheet and results compared to show any possible asymmetry on the chamber (see figure 4.30).

If nothing indicating serious problems is found this file is saved in a dedicated database, and, when a sufficient number of chamber is tested (more than 10), all the data are processed together to establish the chamber class (*NR 3.2.1, 3.4, 3.5.8*).

Due to the imperfect collimation of the source[21] a 'border gap effect[22]' has to be corrected. A full normalization is given taking the average measured value on each single point and considering the found value as correction factor for that point. By dividing each point registered during the test for its proper correction factor all data are normalized to the unity. The final considered value is the bi-gap normalized point: the average between analogous points on first and second gap for the first bi-gap, average between analogous points on third and fourth

[21] The choice to have a large solid angle emission was mandatory due to the reduced intensity of the source, a better collimated source implies an insufficient intensity and relatively excessive background for the test.

[22] Measured current values on the more external points are considerably lower compared to those near the center of the active area.

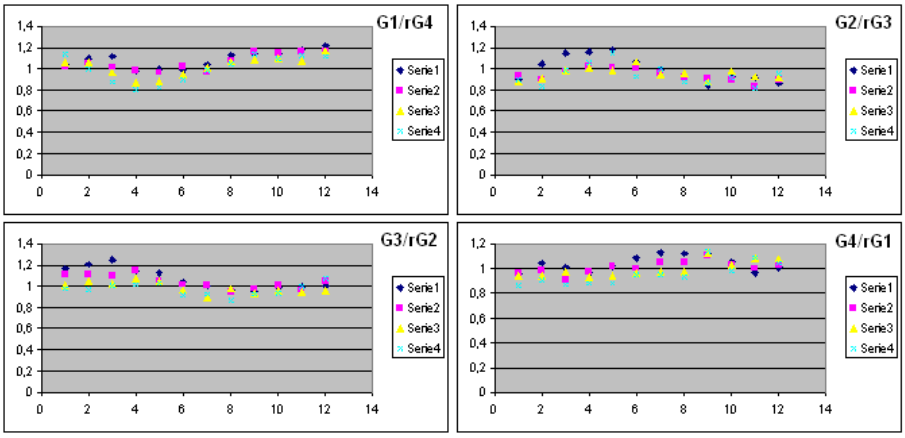

Figure 4.30: Top/reverse ratio: here are shown ratios between spatially corresponding points measured currents in top and reverse gas gain test. Ratio vs line number point and different colors for the 4 different points along the same wire can show asymmetries on the considered chamber. G(1,2,3,4) are the current values on each gap for top test, rG(1,2,3,4) for the reverse test.

gap for the second bi-gap.

A typical result of final analysis of the measurement is shown in figure 4.31 for M4R3 chambers. For any chamber the shown value is the average of all bi-gap normalized points, and the error bars are showing minimum and maximum normalized registered values. Referring to criteria reported in equations 4.2 and 4.3 is now possible to class each double-gap tested. The only data considered for the final classification are coming from the 'top' test; data coming from the 'reverse' test are analyzed in parallel as a confirmation of the obtained values, used (together with top data) to establish the reliability of each single test and to check the real symmetry of response over the chamber (*NR 3.6.2, 3.6.3, 3.6.5*).

AA, AB and BA class chambers are considered good chambers, BB class chambers are eligible to be used as 'spare' chambers, and AC,CA,BC,CB and CC class chambers have to be investigated for the occurred problems and eventually recovered (where possible) and then re-tested. Chambers showing large difference between top and reverse tests and not satisfying final check requirements are re-tested. The final chamber classification is then registered on the on-line database and the chamber is now ready for the shipping to LNF for the final dressing and the electronic tests (*NR 3.2.1, 3.5.8*).

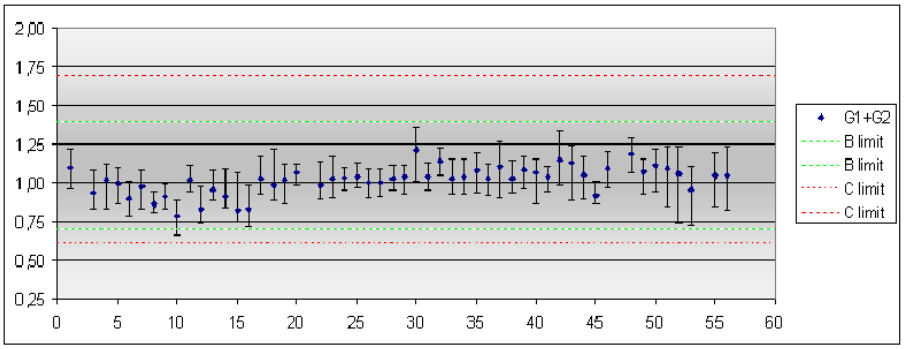

Figure 4.31: Sample of chamber classification (only one bi-gap here). Normalized gas gain vs chamber number. Average value is shown by blue spots, maximum and minimum measured value are shown by 'error' bars, green and red lines show the class (A,B,C) borders.

Chapter 5

GIF tests, production and quality control results

Introduction

To ensure the correct working of the produced MWPCs and to have a significant feedback about production quality all the data are analyzed. Production rate, test results, and the most significant informations about all the chambers produced under Ferrara LHCb INFN group responsibility are summarized on this section.

In addition to the tests performed on site, with a view to create background conditions similar to those existing in the experiment during the operation of the LHC machine, our group executed a different set of measures at CERN on a limited number of MWPCs. Ageing tests and gain curves at high particle rate have shown anomalous electrical emissions on the cathode surfaces of some chambers, leading to investigate deeply this problem. The Gamma Irradiation Facility at CERN has been used to test 12 chambers (48 gaps) produced in Ferrara, during the period between june 2005 and march 2006, test setup and final results are presented section 5.1.

5.1 Gamma Irradiation Facility tests

The Gamma Irradiation Facility (GIF) [45] is a test area in which high-energy particle detectors are exposed to a particle beam in the presence of a strong background flux of photons, simulating the conditions that these detectors will suffer in their future operating environment at the Large Hadron Collider. The GIF is situated at the downstream end of the X5 test beam. The zone is surrounded by a 8 m high and 80 cm thick concrete wall. Access is possible through three entry points, namely two access doors for personnel and one large gate for material. A crane allows to install heavy equipment into the area. A

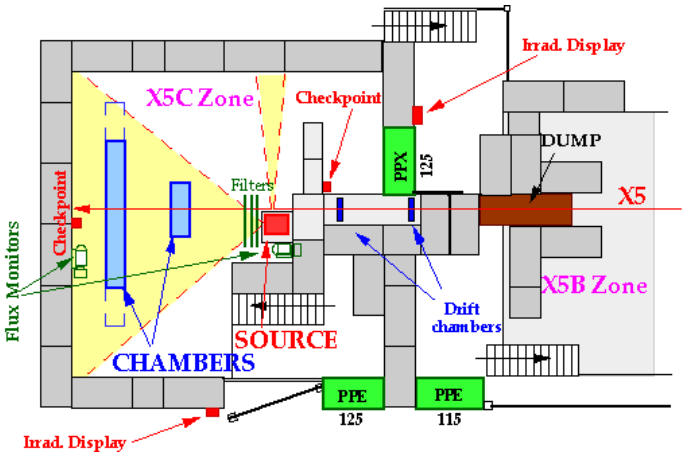

Figure 5.1: The layout of the Gamma Irradiation Facility (GIF)

schematic layout of the GIF zone is shown in figure 5.1.

The photons are produced by a strong radioactive source (irradiator). It is installed in the upstream part of the zone, 5 m away from its downstream end, and housed inside a lead container, which includes a precisely shaped collimator, designed to permit irradiation of a 6x6m^2 area at 5 m distance from the source. A filter system, composed of four 1 mm thick lead discs of different diameters fixed at the exit face of the collimator, serves to render the outcoming flux more uniform in the vertical plane. At 4 m distance from the source the flux on the axis is $1.8 \cdot 10^5 \gamma\, cm^{-2} s^{-1}$.

A second irradiation area has been foreseen at 90° to the main axis. This area is defined by a separate collimator, which allows to irradiate detectors with a high flux over a smaller area, e.g. crystal calorimeters. It can be activated or isolated by means of a separate shutter. If opened, this channel provides a flux of $6 \cdot 10^6 \gamma\, cm^{-2} s^{-1}$ at 1 m distance from the source. The two facilities can thus operate separately or in parallel.

The Gamma irradiator is housed in a rectangular container, 400 mm each side and 900 mm high. The active element is a radioactive ^{137}Cs source of strength 740 Gbq. This isotope was preferred above ^{60}Co because of its longer half-life of 30 years and hence less variation of the photon flux over the years of use of this facility. Also its lower photon energy (662 keV/c) leads to a twice higher conversion efficiency in the detectors tested.

The source is protected by a lead shield of 140 mm thickness. The lead is contained in a 5 mm thick steel envelope. The principal collimator hole provides a conical aperture of 74 steradians solid angle. This provides a photon flux in a volume of 5 m maximum length along the axis. A pneumatic system allows to move the source upwards into its irradiation position or to leave it in its lower, shielded, position. In case of pressure drop, the source falls naturally, by its own weight, in its protecting container.

Up to some 10^4 muons per SPS cycle from the X5 beam enter the Gamma Irradiation Facility and are tagged by scintillators and a system of two Delay Wire Chambers. The efficiency and/or resolution of detectors can thus be tested as a function of the background photon flux. Also radiation resistance measurements with and without beam are now performed on a routine basis by the big LHC collaborations.

5.1.1 Experimental setup and performed test

Once at the GIF, two chambers are tested simultaneously, with a distance from 0.6 m to 1.5 m from the irradiator. A dedicated gas system provides the usual operational gas mixture for the chambers, and, after the needed changes of volume, the MWPCs are conditioned.

The system for measuring currents and voltages during MWPC conditioning is based on the multi-channel CAEN HV power supply and Opera I-meter connected to PC through the serial ports, as in Ferrara. Usually the negative voltage is installed on 4 gaps in parallel, but if needed, each gap can be supplied separately. At the end of wire conditioning at negative voltage the test at positive voltage is performed. The resulting dark currents, as well as the currents from the radioactive source at predefined HV are measured and recorded for documentation on an excel file.

Cathode quality tests and cathode surface conditioning, if needed, is performed using the Gamma Irradiation Facility in order to have many positive ions on the cathode surface. As known, the ion bombardment is used for treatment of surfaces. In order to have ions, electrons ionize the gas creating new electron-ion pairs. On GIF it is possible to have many positive ions and to provide treatment of wire and cathode surfaces separately applying negative or positive HV to the wires respectively.

What has been observed in some chambers, indicated as PP chambers, constructed using panels made with a different cathode plating method[1], is a building-up effect on the measured currents when the source was switched on, starting self-sustained currents still present when the source was switched off. So, the currents in some gaps become to increase at some moment, then exactly the same remaining currents (micro-Amperès) are well seen in the diagram when the source was switched off. This phenomenon is well reproducible. In figure 5.2 can be seen a sample screenshots from Opera about a normal operating chamber and a chamber affected by those anomalous electric emissions: after the source switching (OFF) all the currents should come to the zero level but it doesn't happen on 3 channels (3 gaps) in the first chamber.

Right now is not well understood why those emission are presents. Thin film field (Malter-like) emission in case of insulators attached to the electrode is one

[1]The difference was in the cathode plating: a small number of cathodes have been constructed during the initial 'training' construction period using a chemical deposition method (those panels are usually indicated as PP, pre-production, panels) and due to the lack of panels shipping they have been used on some M5R2 type MWPCs. All the other cathodes were made using an electroplating method.

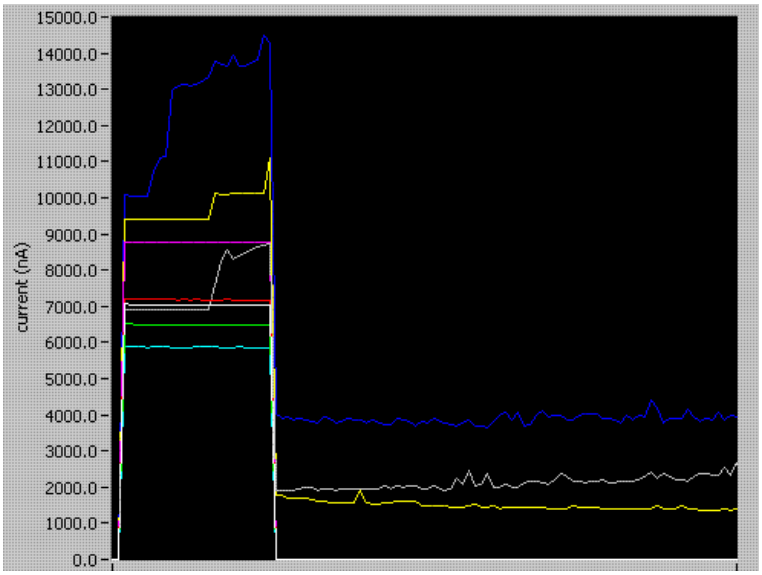

Figure 5.2: Measured Currents vs time at 2300 V, building-up effect before source switching, then after the switch off self-sustained currents are still presents. Blue, yellow, purple and gray lines indicate the four gaps in the first chamber (respect to the source); red, white, green and ice-blue the four gaps in the second chamber.

of the proposed models. Indeed chemical gold plating produce a more porous cathode surface compared to the electroplating, while the cleaning method was the same for all kind of panels.

This type of emission from metal, proposed during joined tests by A. Kashchuk from CERN LHCb group, occurs if a porous insulator covers the surface of metal. The film is charged by positive ions (building-up effect), and at some charge the potential energy will be enough high for tunneling of electrons through the potential barrier. Primary electrons emitted by the metal are accelerated by the field on their way and initiate individual avalanches, thus producing a much larger secondary electron current. This effect is very similar to the 'Malter effect', sometimes found as cathode emission in aged wire chambers, first described by Malter in 1936[46].

As observed in our tests, the emission can start for different gaps at different voltages, but ever below the operational voltage. The test is a simple gas gain curve at very high particle rate, switching on and off the source at each predefined voltage. All the gaps are supplied separately and the emission starting voltage doesn't depend on the distance from the source.

When emissions are found on a gap, the tension on that gap is not raised anymore and the gap is marked as defective. The test continues on the other gaps until anomalous emissions are found, the limit voltage is fixed at 2.75 kV, where currents between 100 and 200 μA are registered on each gap, for safety reasons. If the limit voltage is reached without any parasitic emission the gap (or the chamber if happened for all gaps) is marked as good.

It has been found experimentally, that the emission is partially self-suppressed if the chamber continuously operates on GIF rather long time, also a negative training helps to reduce those parasitic emissions but is not possible to fully suppress them. Anyway after our test is well clear which chambers are affected by this problem, that occurred only on a limited number of Chambers. For the 'defective' PP chambers has to be decided what to do, those emissions have been observed only at high particle rate, while the incriminated chambers will work at much lower rates (see table 2.4 and section 5.1.2), those MWPCs will be probably used as spare chambers.

5.1.2 Test results

During the period from june 2005 until march 2006 a total of 12 chambers have been tested at GIF:

- 6 M5R2 (01, 02, 15, 16, 18, 27)
- 5 M4R2 (06, 12, 20, 24, 26)
- 1 M2R3 (54)

four of them (M5R2 15,16,18,27) were marked as PP chambers (with chemical gold plating), here in Figure 5.3 is reported, for each chamber, the starting voltage of emission on each gap, the self-sustained current measured at that

CH ID number (gap)	Start (V)	Start (I)	Max (V)	Max (I)	Test result
M5R2C01 (1)	-	-	2750 V	2-3 nA	OK
M5R2C01 (2)	-	-	2750 V	2-3 nA	OK
M5R2C01 (3)	-	-	2750 V	2-3 nA	OK
M5R2C01 (4)	-	-	2750 V	2-3 nA	OK
M5R2C02 (1)	-	-	2750 V	2-3 nA	OK
M5R2C02 (2)	-	-	2750 V	2-3 nA	OK
M5R2C02 (3)	-	-	2750 V	2-3 nA	OK
M5R2C02 (4)	-	-	2750 V	2-3 nA	OK
M5R2C15 (1)	1950 V	230 nA	2300 V	25 μA	Failed
M5R2C15 (2)	2150 V	3 μA	2300 V	9 μA	Failed
M5R2C15 (3)	2400 V	8 μA	2400 V	8 μA	Failed
M5R2C15 (4)	2300 V	6 μA	2300 V	6 μA	Failed
M5R2C16 (1)	2000 V	12 μA	2200 V	52 μA	Failed
M5R2C16 (2)	2000 V	17 μA	2200 V	77 μA	Failed
M5R2C16 (3)	-	-	2750 V	2-3 nA	OK
M5R2C16 (4)	-	-	2750 V	2-3 nA	OK
M5R2C18 (1)	2300 V	3 μA	2650 V	40 μA	Failed
M5R2C18 (2)	2400 V	2 μA	2750 V	14 μA	Failed
M5R2C18 (3)	2000 V	14 μA	2200 V	56 μA	Failed
M5R2C18 (4)	2000 V	5 μA	2200 V	33 μA	Failed
M5R2C27 (1)	-	-	2750 V	2-3 nA	OK
M5R2C27 (2)	2400 V	0.8μA	2400 V	0.8μA	Failed
M5R2C27 (3)	2100 V	5 μA	2150 V	8 μA	Failed
M5R2C27 (4)	2400 V	2 μA	2400 V	2 μA	Failed
M4R2C06 (1)	-	-	2750 V	2-3 nA	OK
M4R2C06 (2)	-	-	2750 V	2-3 nA	OK
M4R2C06 (3)	-	-	2750 V	2-3 nA	OK
M4R2C06 (4)	-	-	2750 V	2-3 nA	OK
M4R2C12 (1)	-	-	2750 V	2-3 nA	OK
M4R2C12 (2)	-	-	2750 V	2-3 nA	OK
M4R2C12 (3)	-	-	2750 V	2-3 nA	OK
M4R2C12 (4)	-	-	2750 V	2-3 nA	OK
M4R2C20 (1)	-	-	2750 V	2-3 nA	OK
M4R2C20 (2)	-	-	2750 V	2-3 nA	OK
M4R2C20 (3)	-	-	2750 V	2-3 nA	OK
M4R2C20 (4)	-	-	2750 V	2-3 nA	OK
M4R2C24 (1)	-	-	2750 V	2-3 nA	OK
M4R2C24 (2)	-	-	2750 V	2-3 nA	OK
M4R2C24 (3)	-	-	2750 V	2-3 nA	OK
M4R2C24 (4)	-	-	2750 V	2-3 nA	OK
M4R2C26 (1)	-	-	2750 V	2-3 nA	OK
M4R2C26 (2)	-	-	2750 V	2-3 nA	OK
M4R2C26 (3)	-	-	2750 V	2-3 nA	OK
M4R2C26 (4)	-	-	2750 V	2-3 nA	OK
M2R3C54 (1)	-	-	2750 V	7-8 nA	OK
M2R3C54 (2)	-	-	2750 V	7-8 nA	OK
M2R3C54 (3)	-	-	2750 V	7-8 nA	OK
M2R3C54 (4)	-	-	2750 V	7-8 nA	OK

Figure 5.3: Summary table about the GIF tests at CERN. Here are indicated: Chamber ID number, starting voltage of emission, self-sustained current measured at starting voltage of emission, maximum reached voltage, measured current with the source off at maximum reached voltage, and test result.

value, the maximum reached voltage and its corresponding measured current with the source off.

Results from this test showed that:

- all the chambers constructed using PP panels are affected by anomalous electric emissions
- 81% (13 over 16) of the gaps made from PP panels showed anomalous electric emissions
- 0% (0 over 32) of the gaps made using gold electroplating method showed anomalous electric emissions
- self-sustained currents start from different voltage values and increase increasing the voltage
- different kinds of chambers showed the same test results.

By these considerations we can conclude that the anomalous electric emission problem is only related to the plating procedure. 7 more chambers (1 M2R3, 2 M4R3, 4 M1R4) have been tested in a different facility at high particle rate and didn't show any anomalous emission.

5.2 Production summary

Starting from 01/06/2004 until 31/01/2007 a total of 246 chambers have been constructed. Different chamber typologies alternated during the whole period starting from the first M2R3 (C000) and ending with the last M2R3 (C066) assembled in january 2007.

Ideally, the production can be separated in two different periods: a first 'regular production' period, in which the production center worked continuously constructing the planned number of chambers (ended on 12/07/2006), and a second 'extraordinary production' period, in which spare chambers and additional chambers needed have been assembled. The following plots (divided by typology of chambers) refer only to the 'regular period' while the final summary plot considers all the chambers produced until 31/01/2007.

Production breaks are due to unexpected lack of material caused by different problems between the panel manufacturer and the responsible site for the HV bar gluing. On all plots is also reported the average production rate during the regular production, while in the summary is also reported an 'overall average production rate' calculated considering also the 'extraordinary period'.

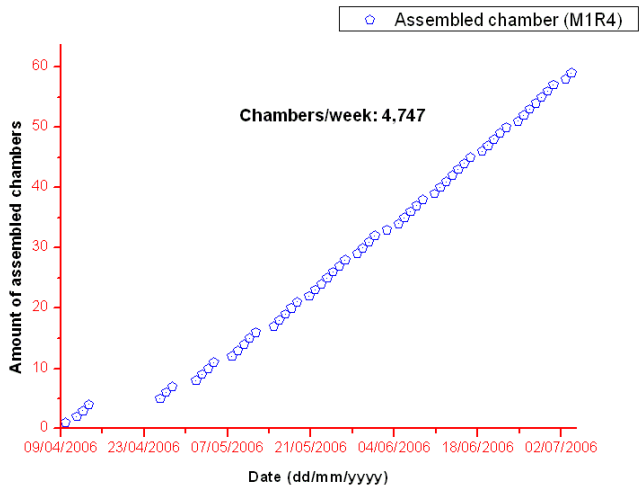

Figure 5.4: Amount of assembled chambers vs date for M1R4 chambers.

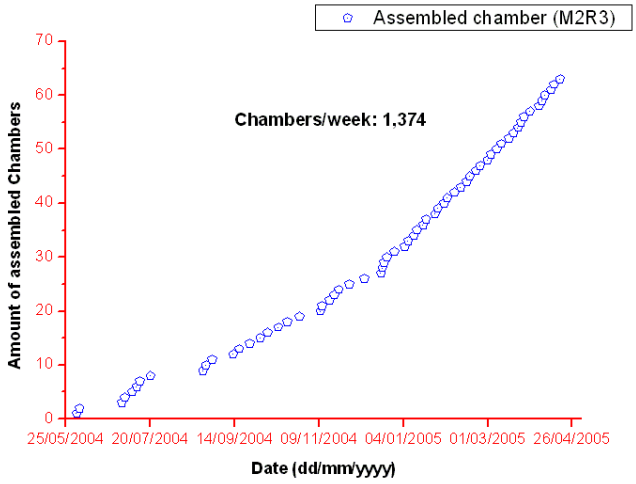

Figure 5.5: Amount of assembled chambers vs date for M2R3 chambers.

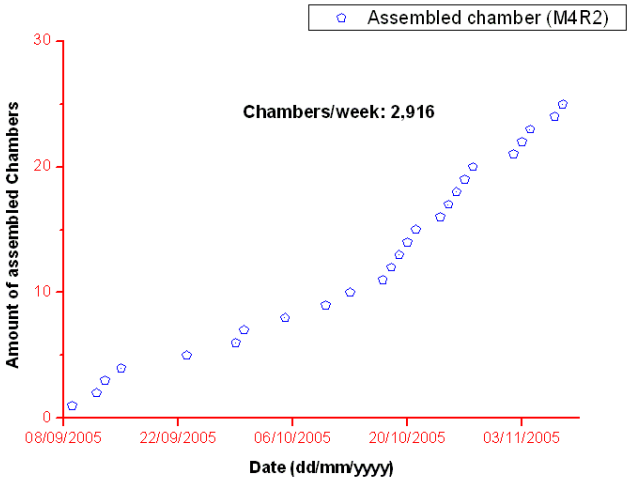

Figure 5.6: Amount of assembled chambers vs date for M4R2 chambers.

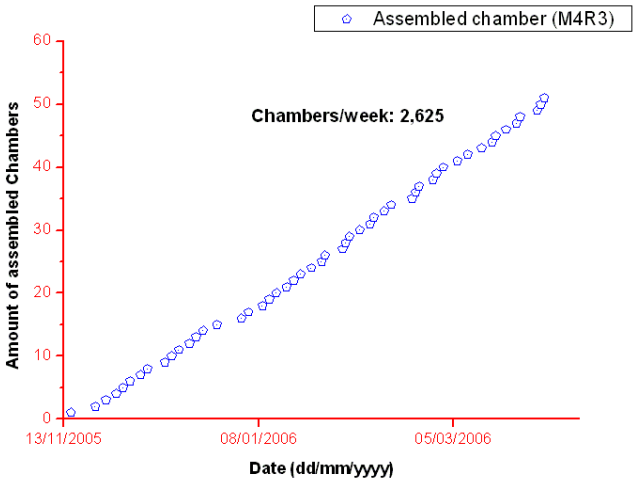

Figure 5.7: Amount of assembled chambers vs date for M4R3 chambers.

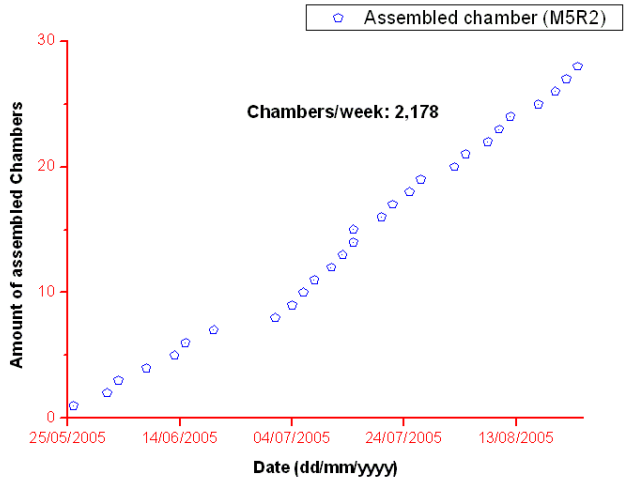

Figure 5.8: Amount of assembled chambers vs date for M5R2 chambers.

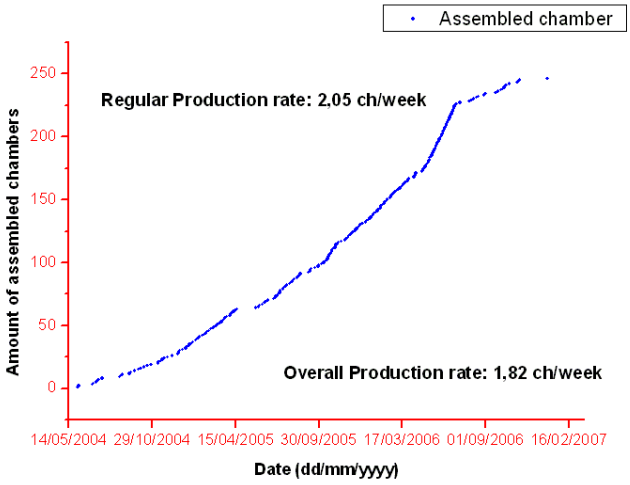

Figure 5.9: Amount of assembled chambers vs date for ALL chambers.

5.3 Pre-production test results

As described in section 4.1.2, preliminary tests are performed only on a small part[2] (typically between 20-40%) of the whole amount of panels received in our production center. This part can be smaller or larger depending from the ratio of rejected panels. Here are presented all the HV bar height tests, of which i personally was responsible for testing and data analysis, divided by typology of chambers, on the following number of panels:

- M1R4: 45 panels (37% of the total number of measurable panels)
- M2R3: 125 panels (43%)
- M4R2: 41 panels (34%)
- M4R3: 48 panels (21%)
- M5R2: 44 panels (29%)

5.3.1 HV bar height measurement results

For each kind of panels are presented height distributions for small (green color) and large (red color) HV bars, average height on each measure point represented with its standard deviation, and total (blue color) height distribution (small and large HV bars together). Height distributions for small, large and both HV bars are also presented at the end as summary of HV bar height test.

M1R4 Over a total of 45 measured panels 3 have been rejected for excessive height on the large HV bar. Here are summarized statistical informations:

- Average height (standard deviation) on HV bar small: 2.411 mm (0.039 mm)
- Average height (standard deviation) on HV bar large: 2.376 mm (0.055 mm)
- Overall average height (standard deviation) on HV bar: 2.393 mm (0.051 mm)

[2]Only after a starting 'training' period on a much larger amount of panels for M2R3 chambers.

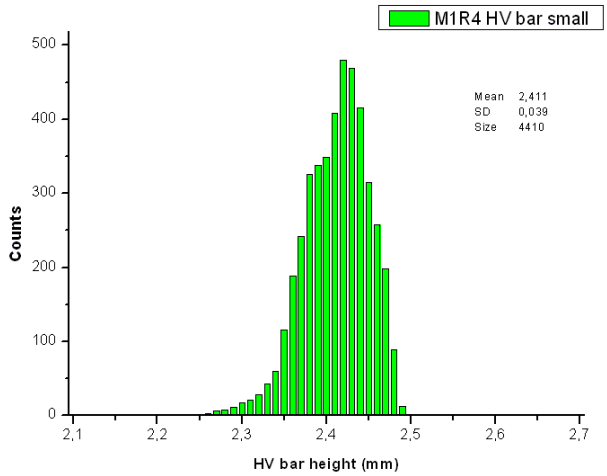

Figure 5.10: HV bar small height distribution for M1R4 panels.

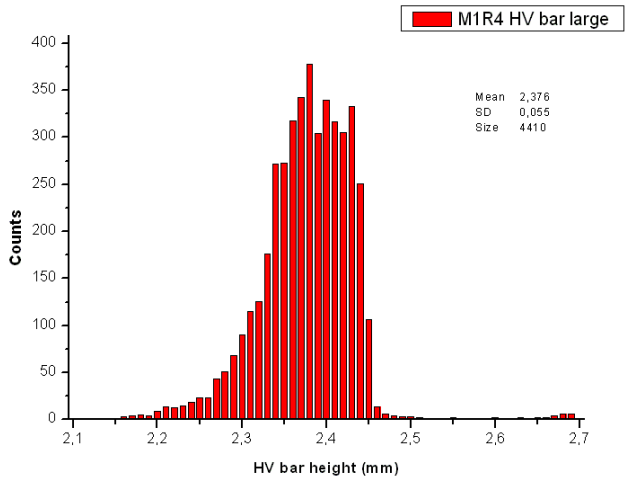

Figure 5.11: HV bar large height distribution for M1R4 panels.

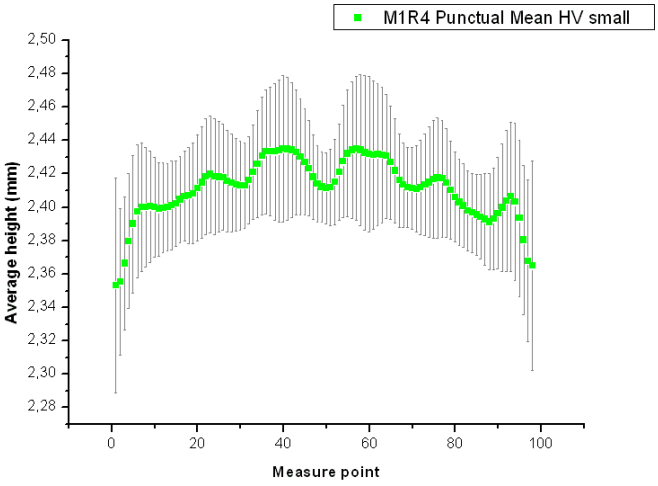

Figure 5.12: HV bar small average height (mm) vs measure point for M1R4 panels.

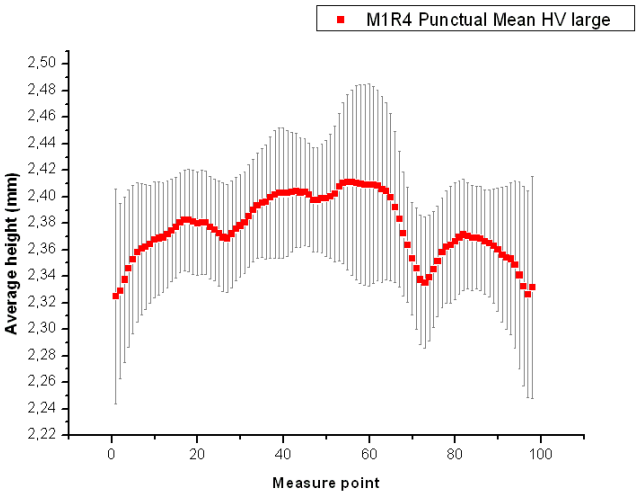

Figure 5.13: HV bar large average height (mm) vs measure point for M1R4 panels.

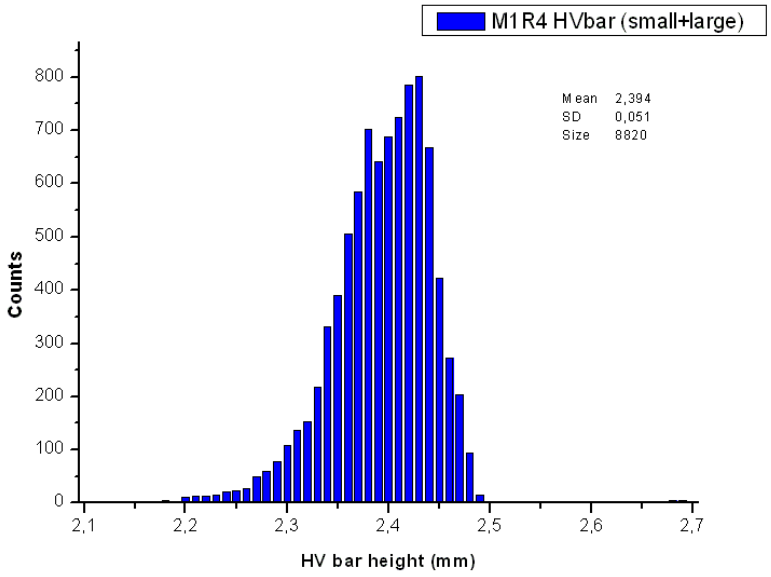

Figure 5.14: HV bar height distribution for M1R4 panels.

M2R3 Over a total of 125 measured panels 13 have been rejected for excessive height on the large (11) and small (2) HV bar . Here are summarized statistical informations:

- Average height (standard deviation) on HV bar small: 2.379 mm (0.050mm)
- Average height (standard deviation) on HV bar large: 2.392 mm (0.050 mm)
- Overall average height (standard deviation) on HV bar: 2.385 mm (0.046 mm)

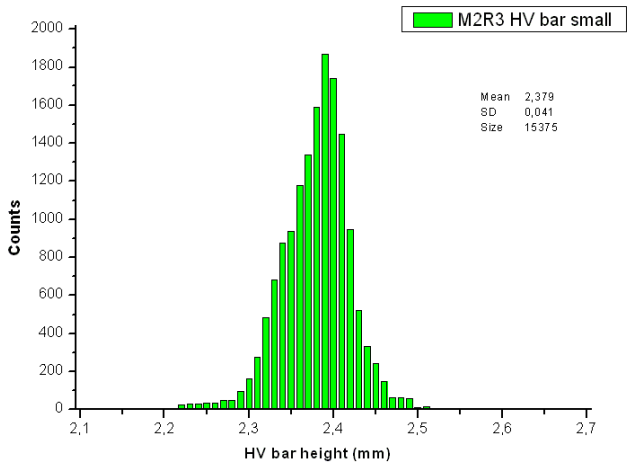

Figure 5.15: HV bar small height distribution for M2R3 panels.

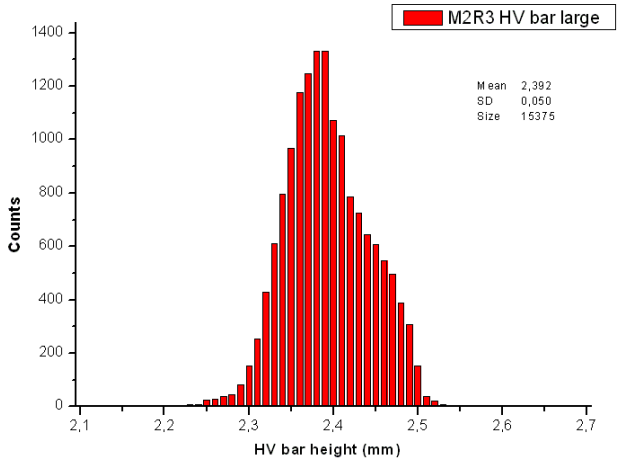

Figure 5.16: HV bar large height distribution for M2R3 panels.

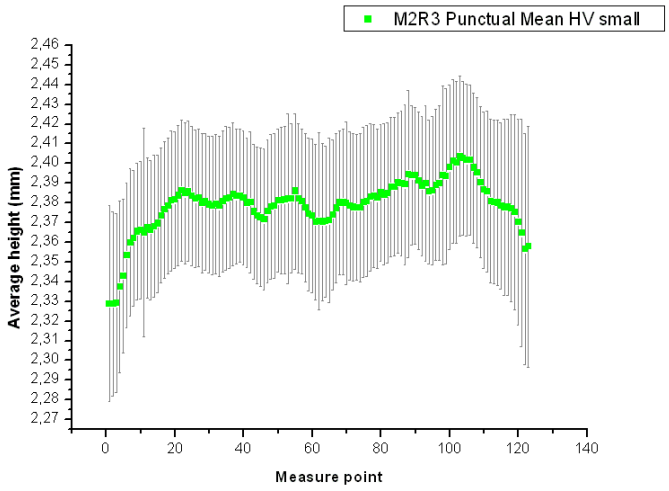

Figure 5.17: HV bar small average height (mm) vs measure point for M2R3 panels.

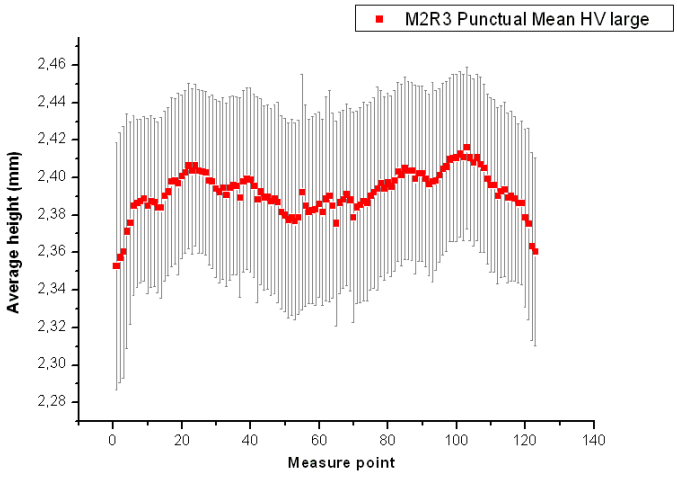

Figure 5.18: HV bar large average height (mm) vs measure point for M2R3 panels.

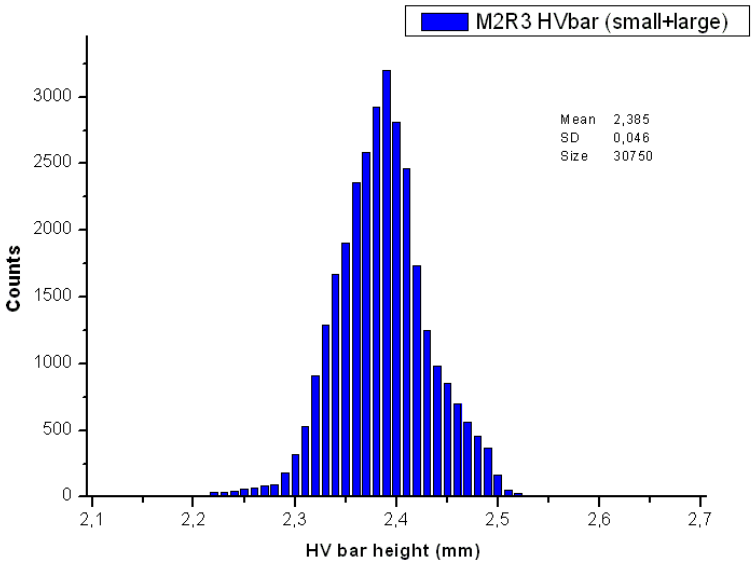

Figure 5.19: HV bar height distribution for M2R3 panels.

M4R2 Over a total of 41 measured panels 1 has been rejected for excessive height on the large HV bar. Here are summarized statistical informations:

- Average height (standard deviation) on HV bar small: 2.323 mm (0.038 mm)
- Average height (standard deviation) on HV bar large: 2.404 mm (0.042 mm)
- Overall average height (standard deviation) on HV bar: 2.363 mm (0.057 mm)

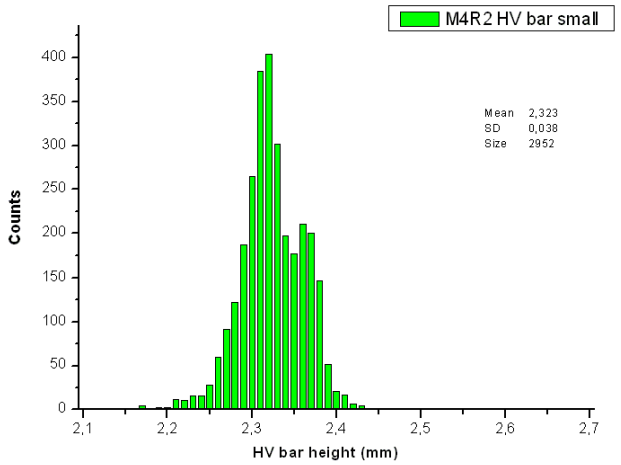

Figure 5.20: HV bar small height distribution for M4R2 panels.

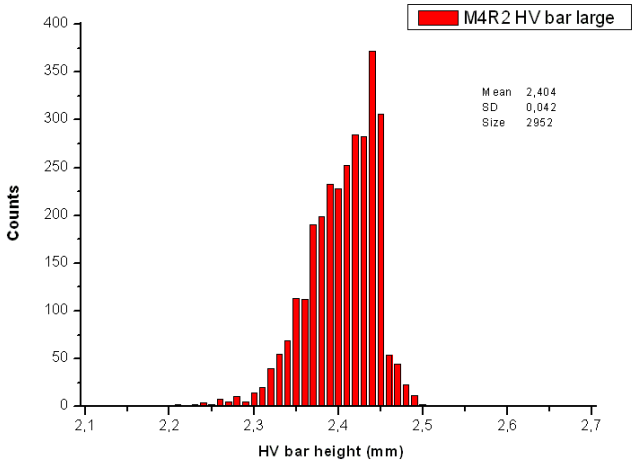

Figure 5.21: HV bar large height distribution for M4R2 panels.

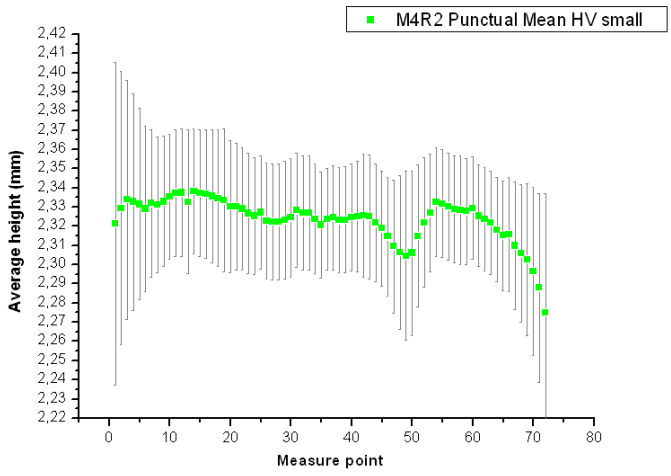

Figure 5.22: HV bar small average height (mm) vs measure point for M4R2 panels.

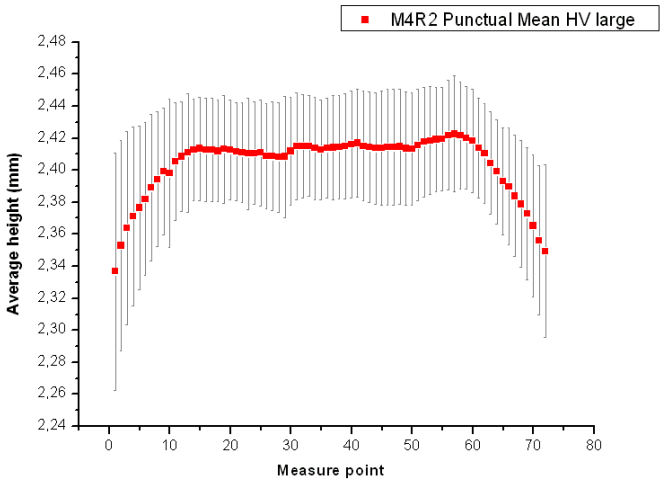

Figure 5.23: HV bar large average height (mm) vs measure point for M4R2 panels.

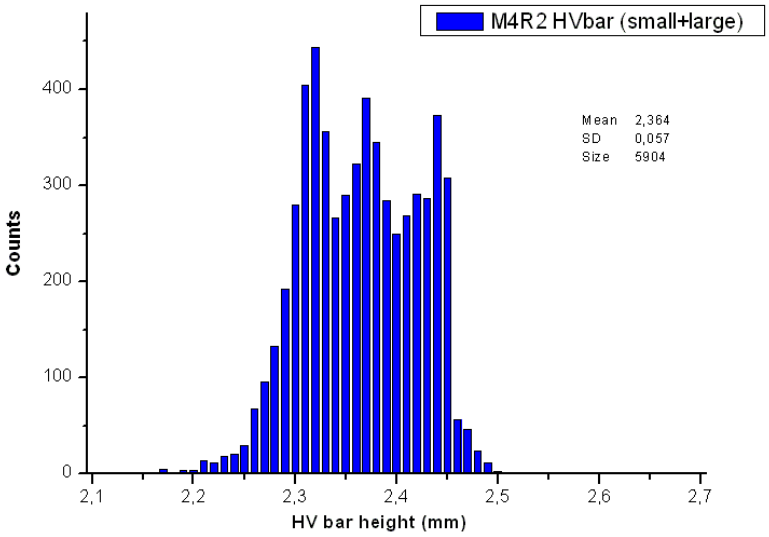

Figure 5.24: HV bar height distribution for M4R2 panels.

M4R3 Over a total of 48 measured panels 4 have been rejected for excessive height on the large HV bar. Here are summarized statistical informations:

- Average height (standard deviation) on HV bar small: 2.362 mm (0.025 mm)
- Average height (standard deviation) on HV bar large: 2.375 mm (0.040 mm)
- Overall average height (standard deviation) on HV bar: 2.369 mm (0.034 mm)

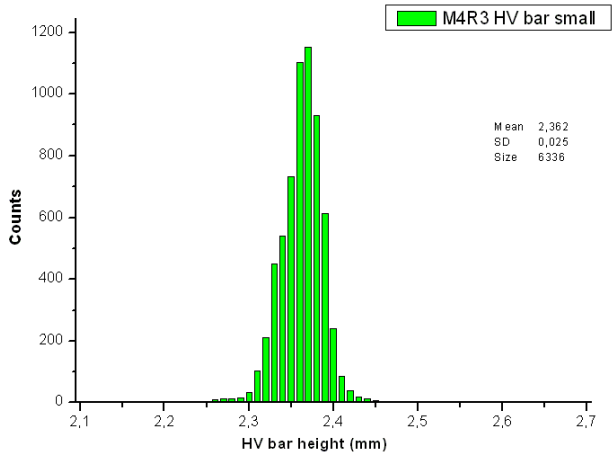

Figure 5.25: HV bar small height distribution for M4R3 panels.

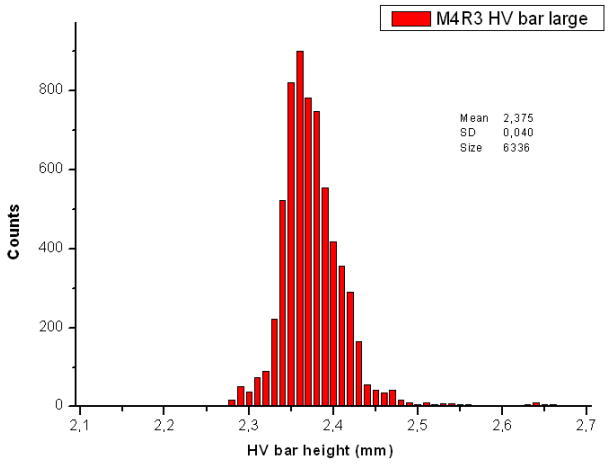

Figure 5.26: HV bar large height distribution for M4R3 panels.

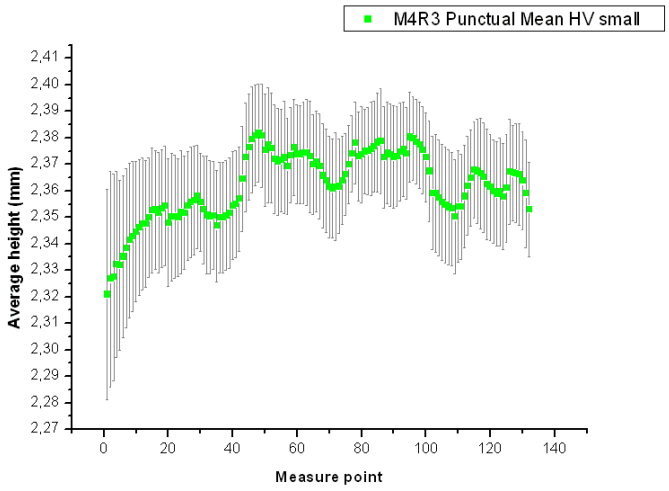

Figure 5.27: HV bar small average height (mm) vs measure point for M4R3 panels.

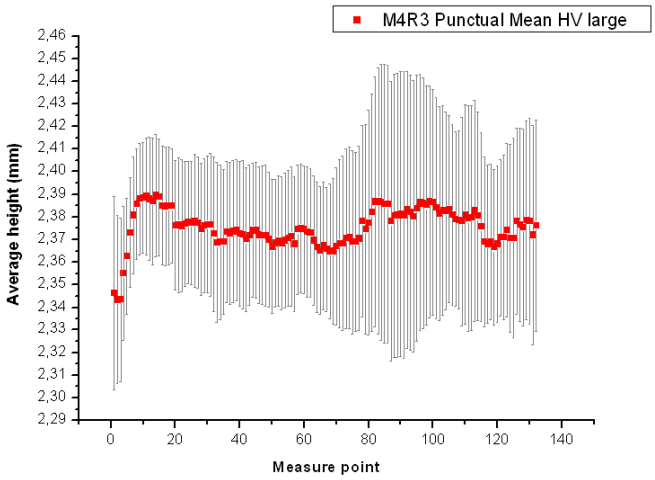

Figure 5.28: HV bar large average height (mm) vs measure point for M4R3 panels.

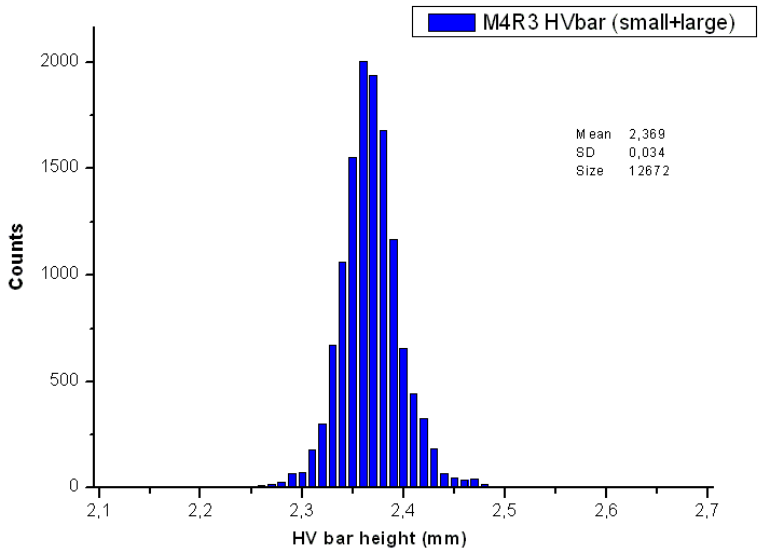

Figure 5.29: HV bar height distribution for M4R3 panels.

M5R2 Over a total of 44 measured panels 3 have been rejected for excessive height on the large (2) and small (1) HV bar. Here are summarized statistical informations:

- Average height (standard deviation) on HV bar small: 2.355 mm (0.050 mm)
- Average height (standard deviation) on HV bar large: 2.403 mm (0.049 mm)
- Overall average height (standard deviation) on HV bar: 2.379 mm (0.055 mm)

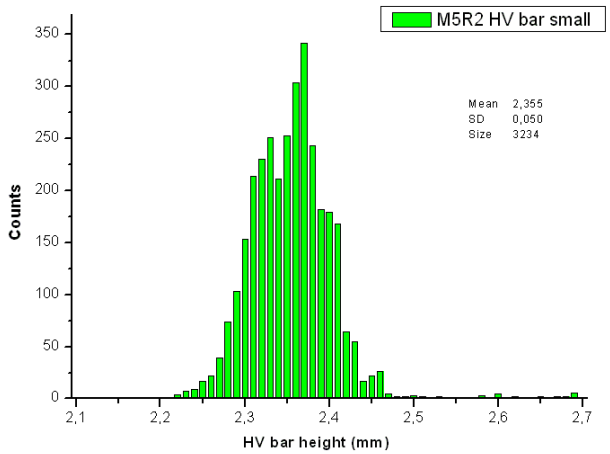

Figure 5.30: HV bar small height distribution for M5R2 Panels.

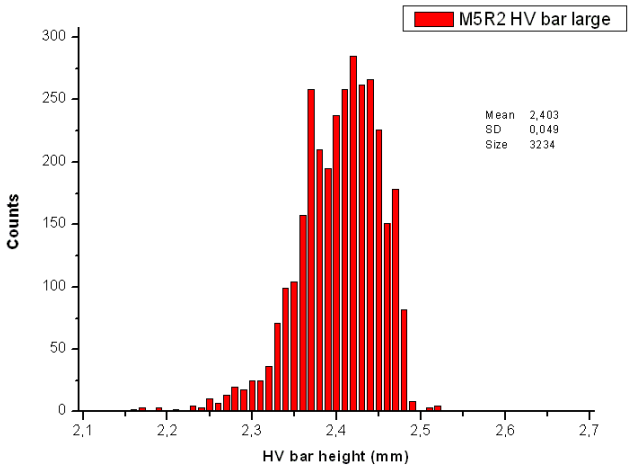

Figure 5.31: HV bar large height distribution for M5R2 Panels.

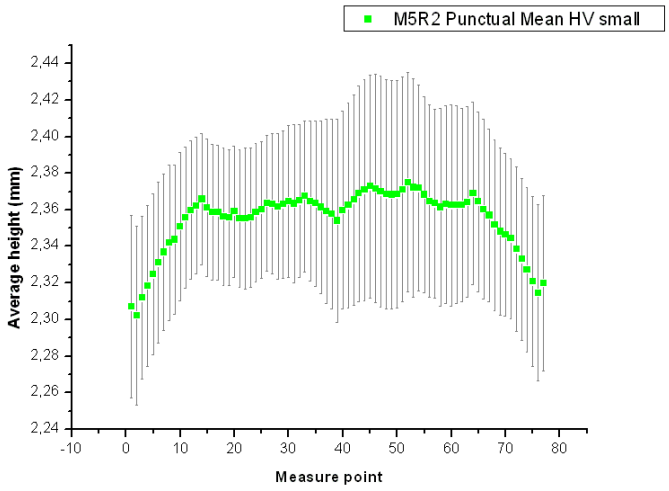

Figure 5.32: HV bar small average height (mm) vs measure point for M5R2 panels.

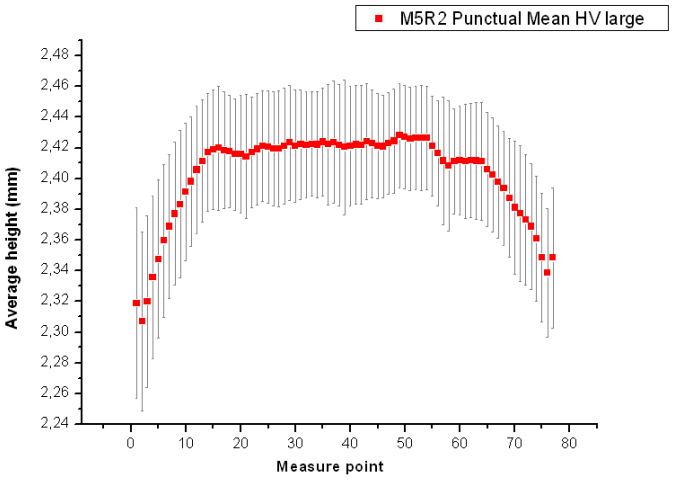

Figure 5.33: HV bar large average height (mm) vs measure point for M5R2 panels.

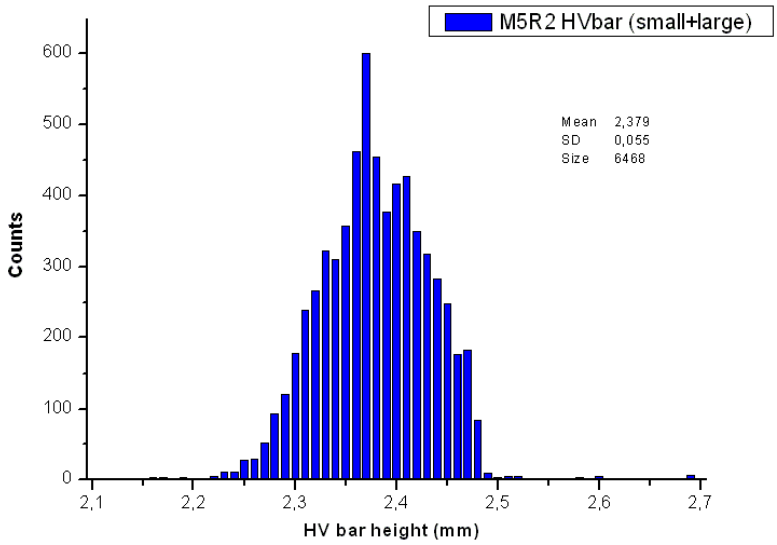

Figure 5.34: HV bar height distribution for M5R2 panels.

Summary Over a total of 303 measured panels 24 have been rejected for excessive height on the large (21) and small (3) HV bar. Here are summarized statistical informations:

- Average height (standard deviation) on HV bar small: 2.372 mm (0.045 mm)
- Average height (standard deviation) on HV bar large: 2.389 mm (0.049 mm)
- Overall average height (standard deviation) on HV bar: 2.381 mm (0.048 mm)

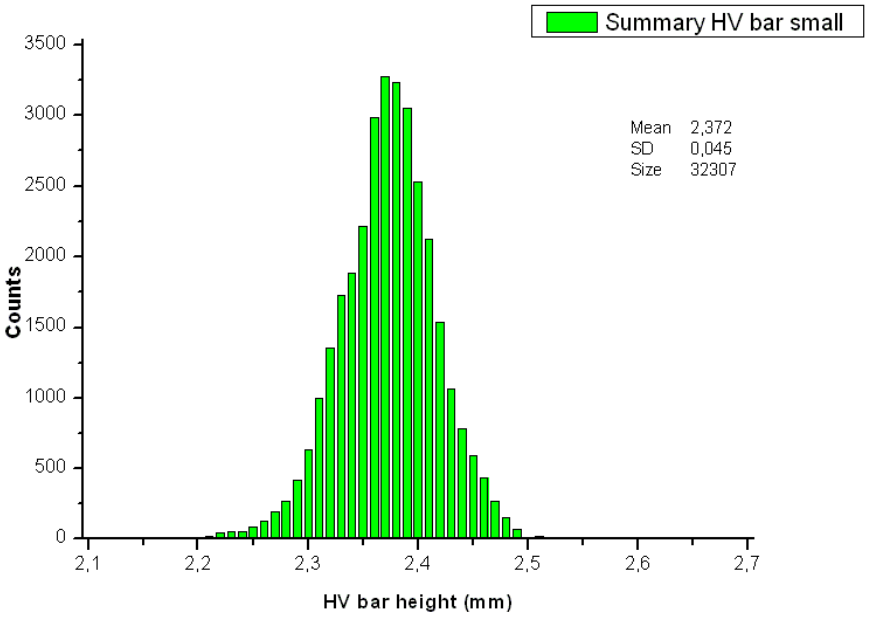

Figure 5.35: HV bar small height distribution for ALL panels.

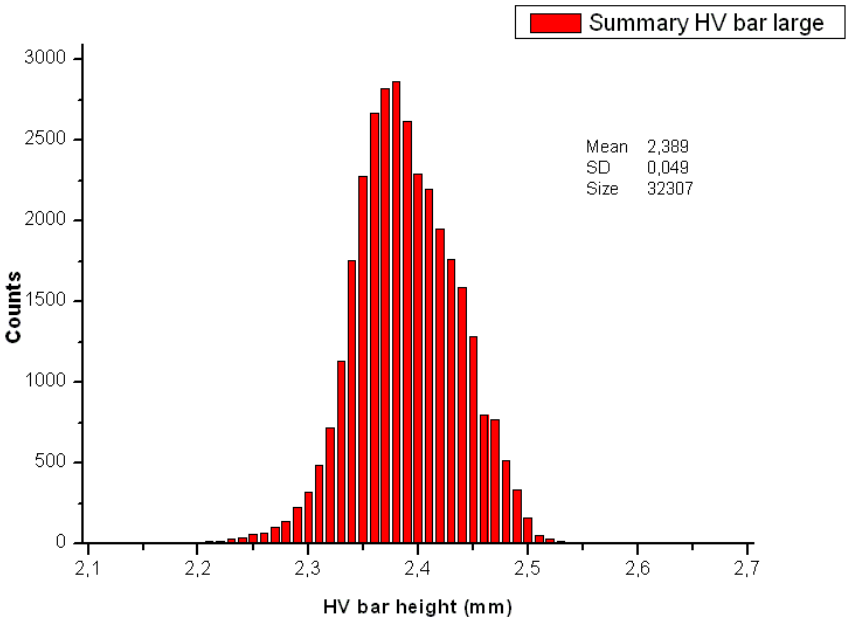

Figure 5.36: HV bar large height distribution for ALL panels.

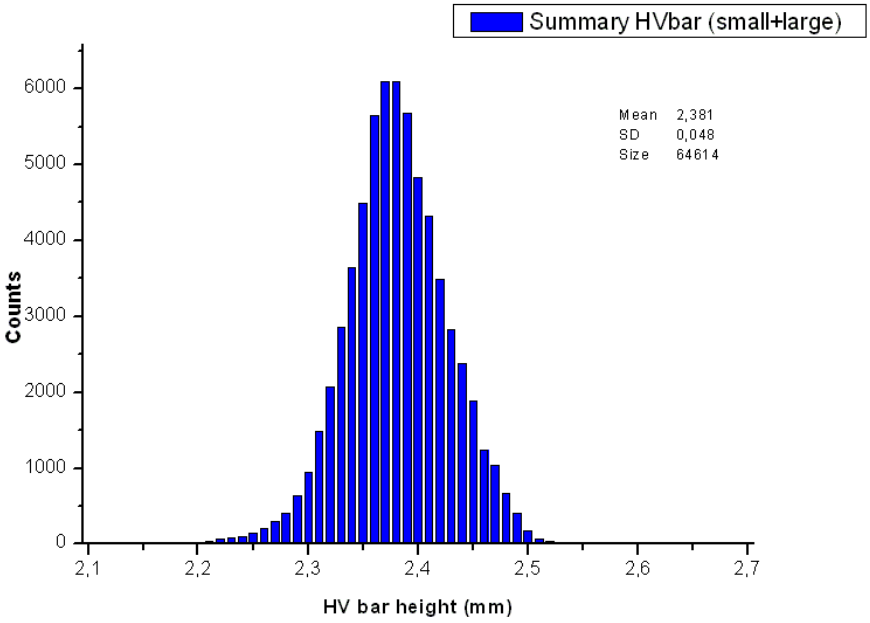

Figure 5.37: HV bar height distribution for ALL panels.

5.4 Production Tests

Production tests are performed inside the clean room on all the panels, i personally collaborated during the panel construction and the panel testing during the whole period of production. Both tests, wire pitch measurement and wire tension measurement, give information about the panel quality before the chamber assembling, so it's possible to recover the rejected panels and then to retest them to check their quality after the recovering procedures. In the following paragraphs are reported all the performed measures for each kind of test.

5.4.1 WPM results

A total number of 891 panels have been tested for the WPM, as made until now they are considered separately for each typology and together in the final summary plot. The distribution of all the distances between two consecutive wires is presented here, considering the data from left (green color) and right (red color) cameras separately and together (blue color).

The very slight asymmetries observed in some distributions can be charged to the large number of switches between different panels typologies in the whole production period. System re-calibrations were made after each switching, but also a mechanical displacement of few μm may determinate those asymmetries.

The use of an on-line software for this test allowed to recover all the potentially rejected panels before the following operation, re-testing them after the recovering procedure. Here are summarized data for all the performed tests:

M1R4 Average pitch:

- 2.000 mm (Standard deviation 0.005 mm) measured by left camera
- 1.997 mm (Standard deviation 0.009 mm) measured by right camera
- 1.999 mm (Standard deviation 0.006 mm) measured by both cameras
- 120 tested panels

M2R3 Average pitch:

- 1.999 mm (Standard deviation 0.010 mm) measured by left camera
- 1.999 mm (Standard deviation 0.011 mm) measured by right camera
- 1.999 mm (Standard deviation 0.011 mm) measured by both cameras
- 275 tested panels

M4R2 Average pitch:

- 1.999 mm (Standard deviation 0.008 mm) measured by left camera
- 1.997 mm (Standard deviation 0.009 mm) measured by right camera
- 1.998 mm (Standard deviation 0.009 mm) measured by both cameras
- 122 tested panels

M4R3 Average pitch:

- 2.000 mm (Standard deviation 0.006 mm) measured by left camera
- 2.000 mm (Standard deviation 0.008 mm) measured by right camera
- 2.000 mm (Standard deviation 0.007 mm) measured by both cameras
- 230 tested panels

M5R2 Average pitch:

- 2.000 mm (Standard deviation 0.013 mm) measured by left camera
- 2.000 mm (Standard deviation 0.008 mm) measured by right camera
- 2.000 mm (Standard deviation 0.011 mm) measured by both cameras
- 144 tested panels

Summary Average pitch:

- 2.000 mm (Standard deviation 0.009 mm) measured by left camera
- 1.999 mm (Standard deviation 0.009 mm) measured by right camera
- 1.999 mm (Standard deviation 0.009 mm) measured by both cameras
- 891 tested panels

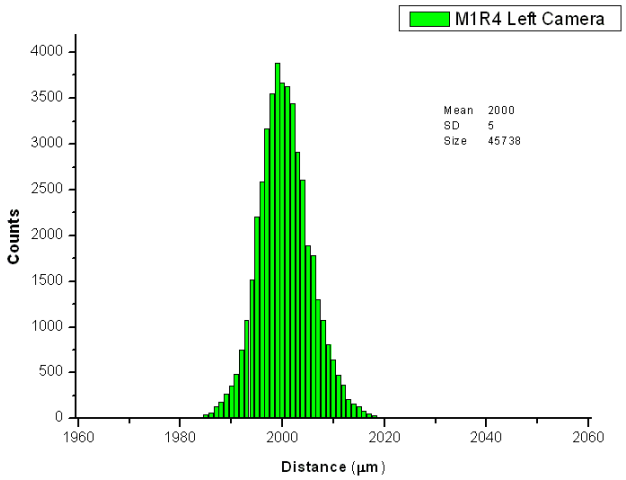

Figure 5.38: Distances distribution (μm) between 2 consecutive wires for M1R4 left and right camera.

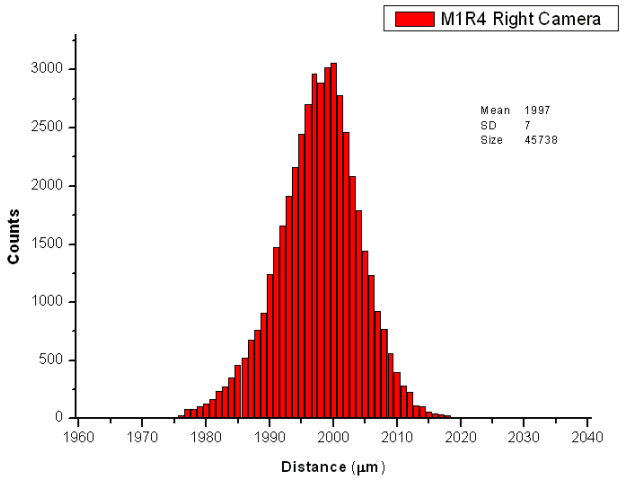

Figure 5.39: Distances distribution (μm) between 2 consecutive wires for M1R4 left and right camera.

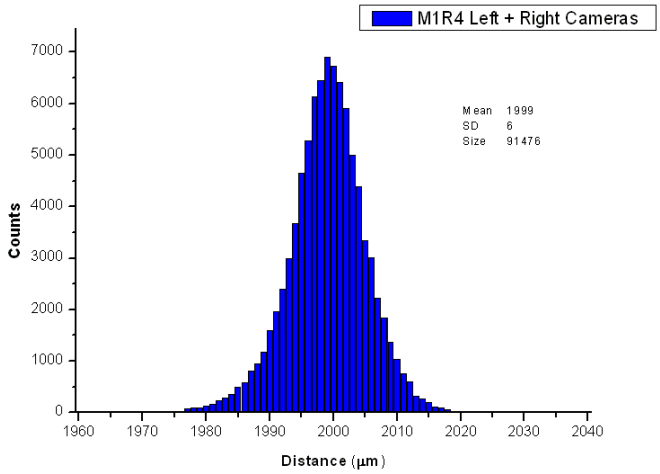

Figure 5.40: Distances distribution (μm) between 2 consecutive wires for M1R4.

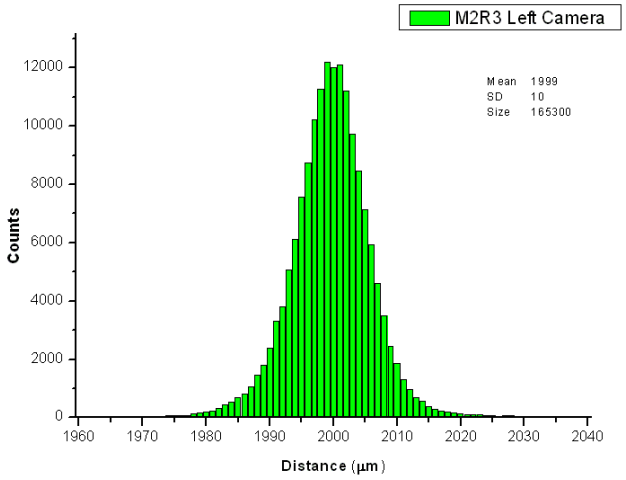

Figure 5.41: Distances distribution (μm) between 2 consecutive wires for M2R3 left and right camera.

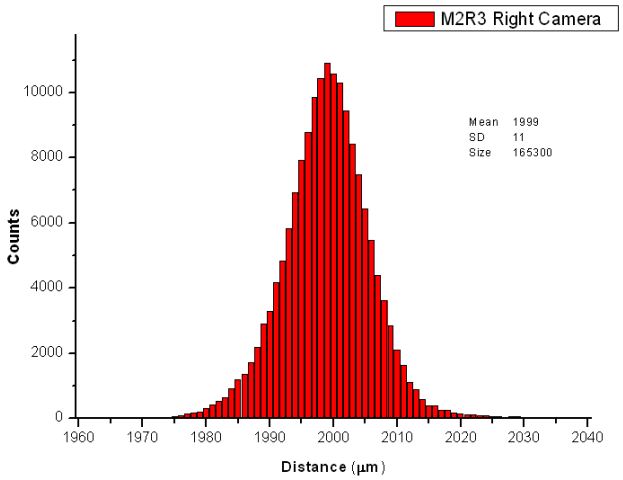

Figure 5.42: Distances distribution (μm) between 2 consecutive wires for M2R3 left and right camera.

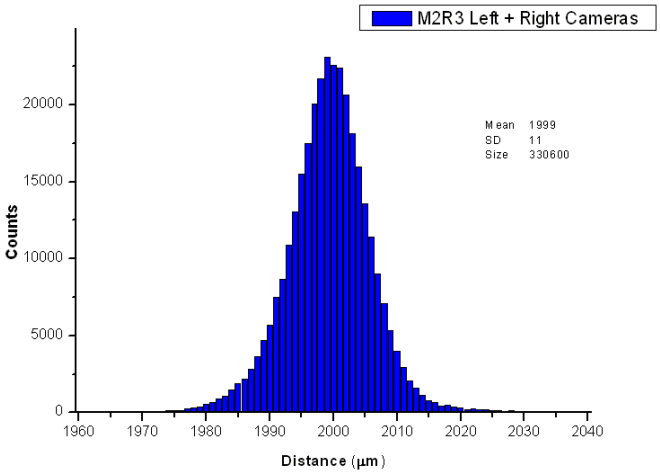

Figure 5.43: Distances distribution (μm) between 2 consecutive wires for M2R3.

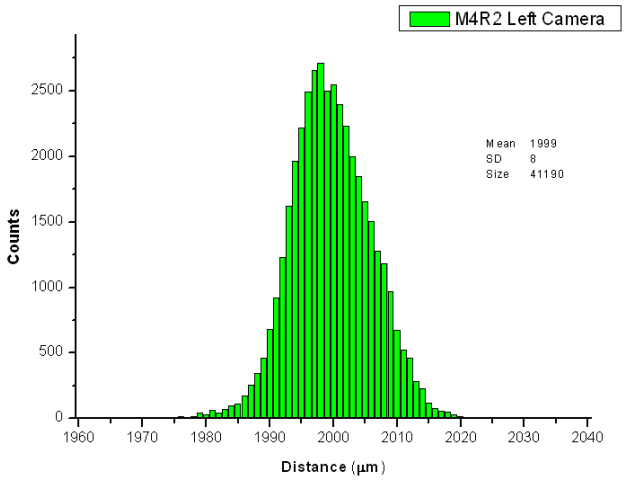

Figure 5.44: Distances distribution (μm) between 2 consecutive wires for M4R2 left and right camera.

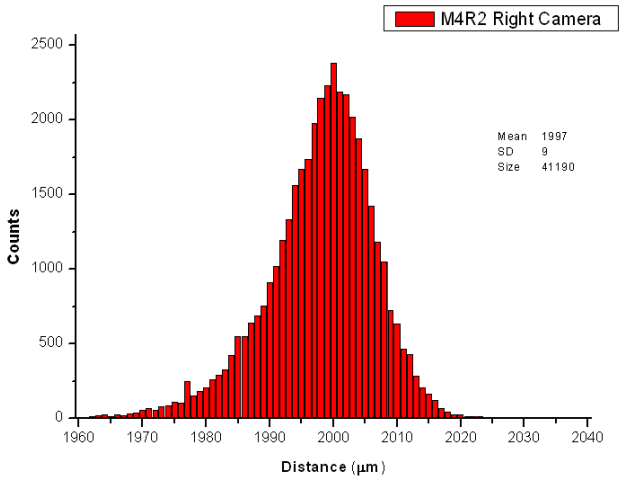

Figure 5.45: Distances distribution (μm) between 2 consecutive wires for M4R2 left and right camera.

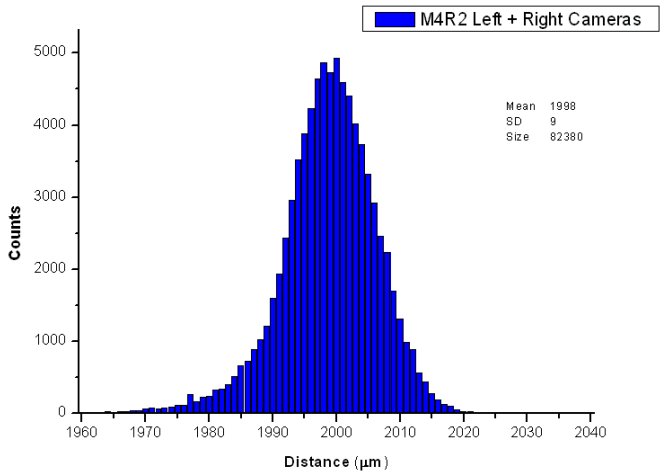

Figure 5.46: Distances distribution (μm) between 2 consecutive wires for M4R2.

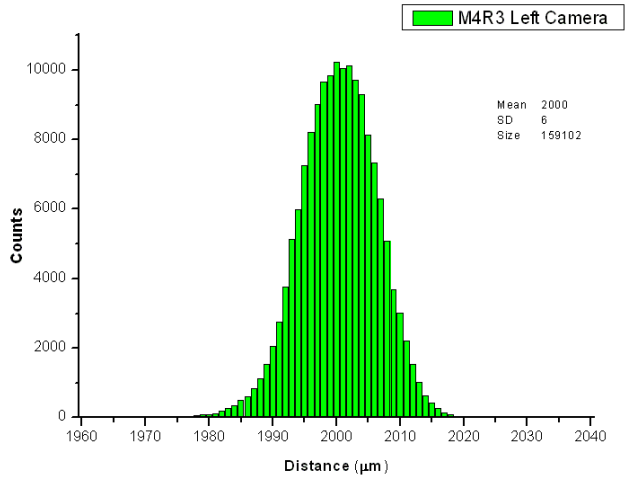

Figure 5.47: Distances distribution (μm) between 2 consecutive wires for M4R3 left and right camera.

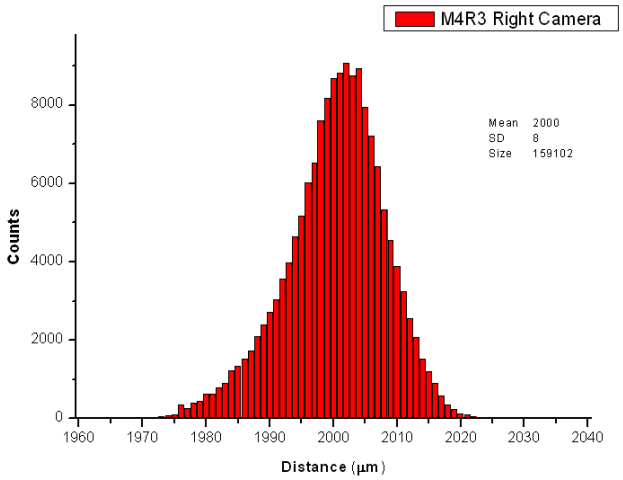

Figure 5.48: Distances distribution (μm) between 2 consecutive wires for M4R3 left and right camera.

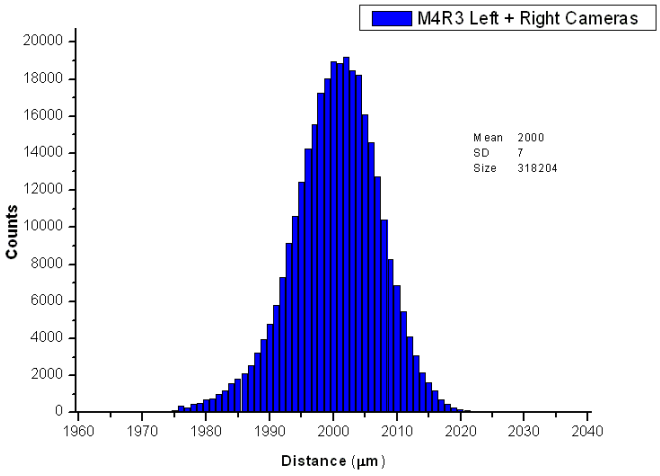

Figure 5.49: Distances distribution (μm) between 2 consecutive wires for M4R3.

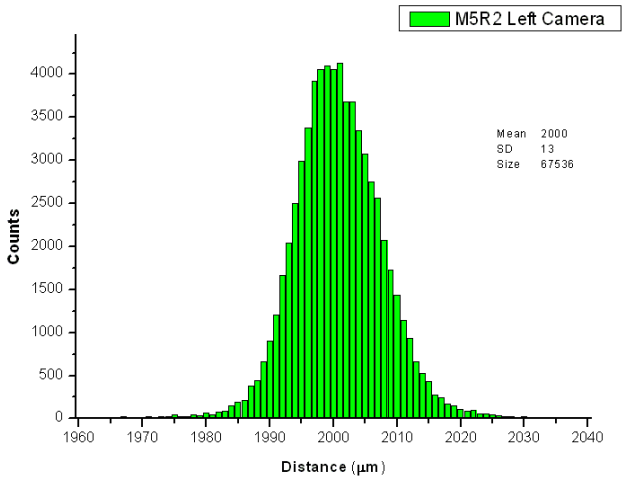

Figure 5.50: Distances distribution (μm) between 2 consecutive wires for M5R2 left and right camera.

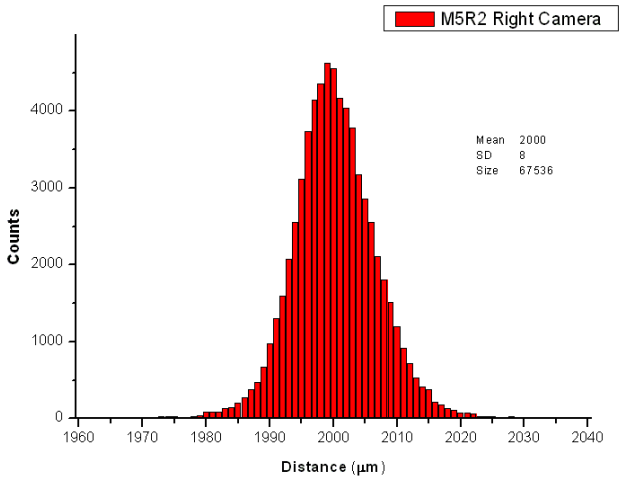

Figure 5.51: Distances distribution (μm) between 2 consecutive wires for M5R2 left and right camera.

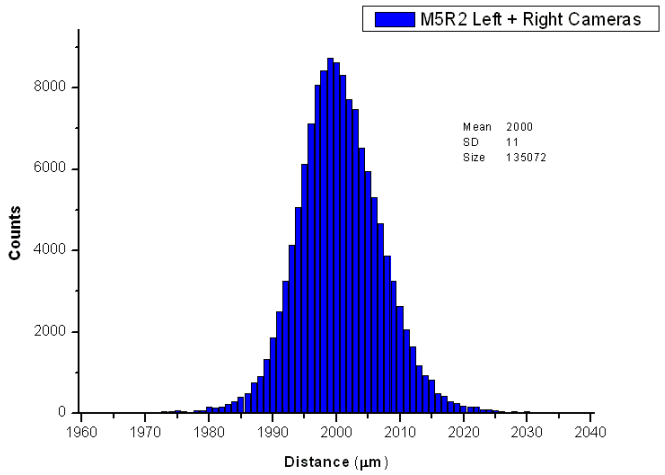

Figure 5.52: Distances distribution (μm) between 2 consecutive wires for M5R2.

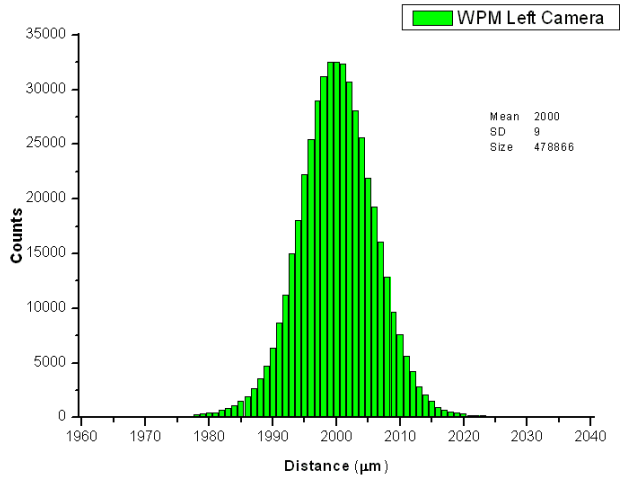

Figure 5.53: Distances distribution (μm) between 2 consecutive wires for ALL panels, left and right camera.

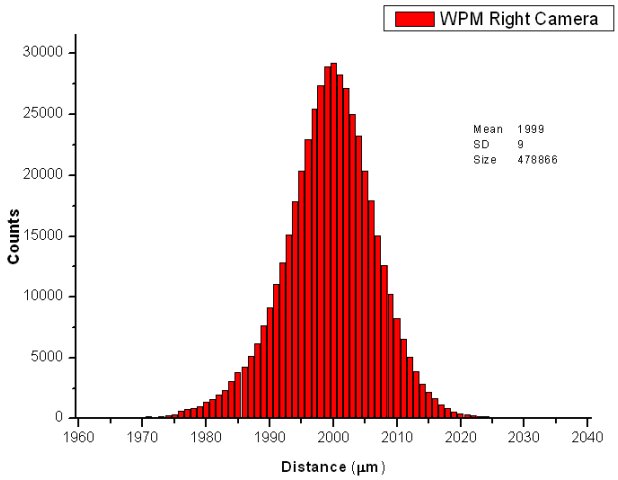

Figure 5.54: Distances distribution (μm) between 2 consecutive wires for ALL panels, left and right camera.

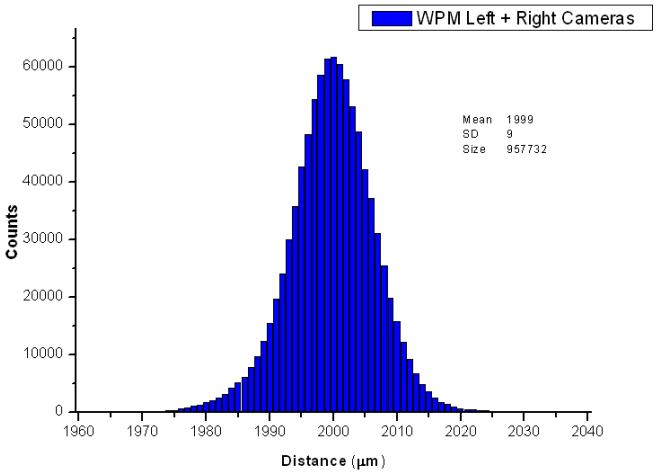

Figure 5.55: Distances distribution (μm) between 2 consecutive wires for ALL panels.

5.4.2 WTM results

The same amount of 891 panels have been tested for the WTM, also for this test they are considered separately for each typology and together in the final summary plot. Here are presented the distributions of all measured wire mechanical tensions (histogram in blue color) for each kind of panel and for the whole production, and the average mechanical tension on each point of measure (indicated naming all wires by consecutive integer numbers starting after the guard wire) for each typology of panels.

The anomalous distribution observed for the M5R2 panels has to be charged to some modifications implemented on the WGS machine. The use of heating bands instead of the lamps, initially induced wire relaxations, leading to modify the electronic tensioner settings to avoid this problem. Also defective wire batches leaded to some electronic tensioner settings modification in order to reduce the risk of wire breaks. It also explains some asymmetry on the distribution observed for M1R4, M2R3 and M4R2 panels.

On the average tension per wire plots can be observed that the first and last two measures are out of the expected distribution, this is due to the manual wire displacing on the frame, needed to position the guard wires before the wire gluing (see section 4.2.3). It has also to be noted that average tension distribution is not flat as expected for M4R3 and M5R2 panels, this effect is probably due to the supports tension settings between the two arms of the wiring frame.

The use of a quick off-line analysis tool allowed to have detailed informations about the potentially rejected panels, all the out of specification wires were marked, and then replaced manually with a recovery procedure. All the panels are then recovered before the following operation, and re-tested after the recovering procedure. Here are summarized average measured tension (and standard deviation) for all the performed tests:

- M1R4: 70.89 g ($\sigma = 4.58$ g)
- M2R3: 69.76 g ($\sigma = 5.99$ g)
- M4R2: 71.10 g ($\sigma = 5.26$ g)
- M4R3: 68.11 g ($\sigma = 4.69$ g)
- M5R2: 70.41 g ($\sigma = 4.90$ g)
- Overall: 69.55 g ($\sigma = 5.34$ g)

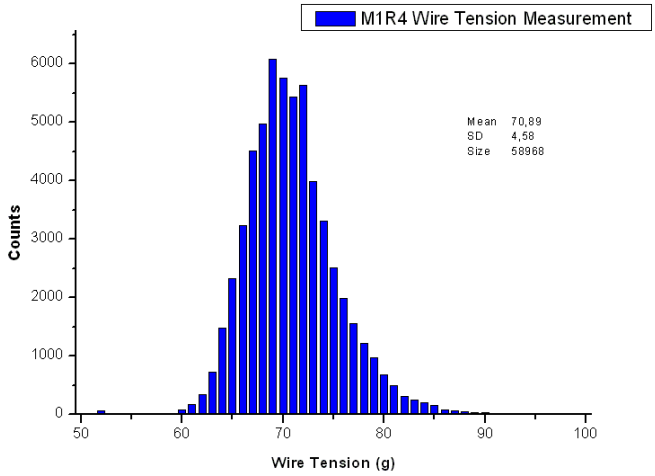

Figure 5.56: Wire tension distribution (g) for M1R4 panels.

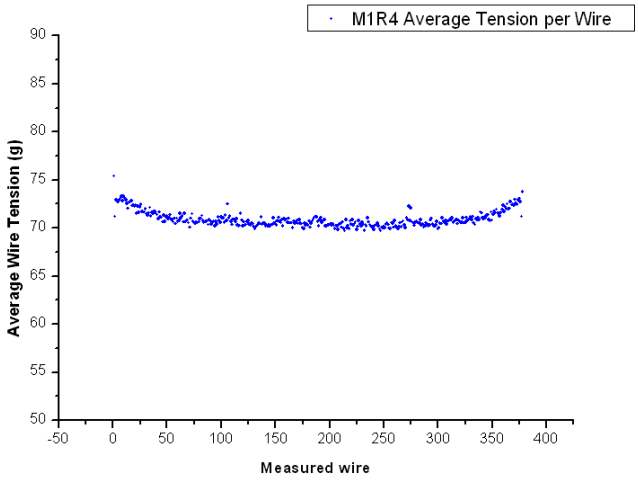

Figure 5.57: Average wire tension (g) vs wire number for M1R4 panels.

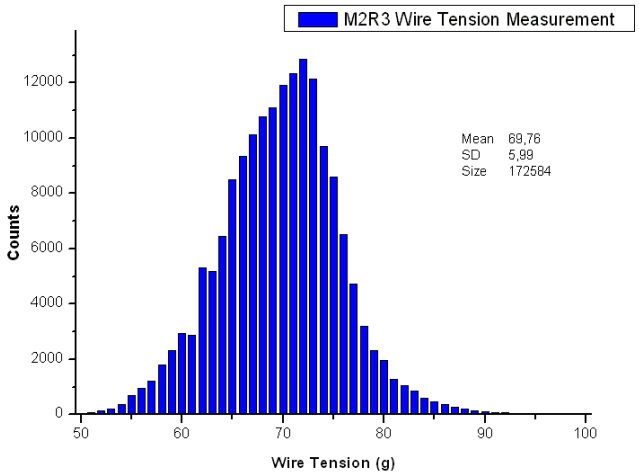

Figure 5.58: Wire tension distribution (g) for M2R3 panels.

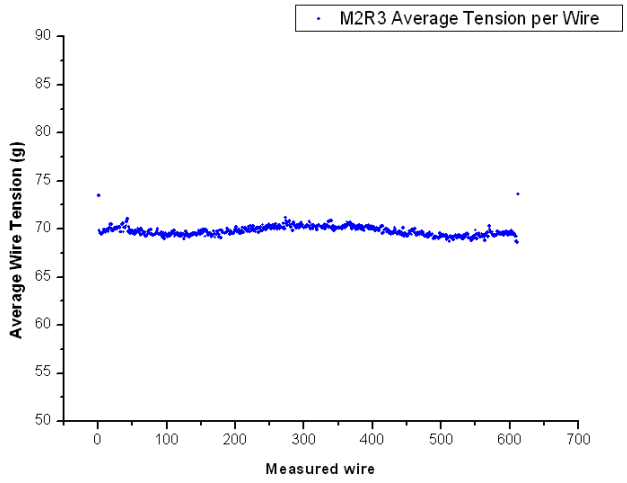

Figure 5.59: Average wire tension (g) vs wire number for M2R3 panels.

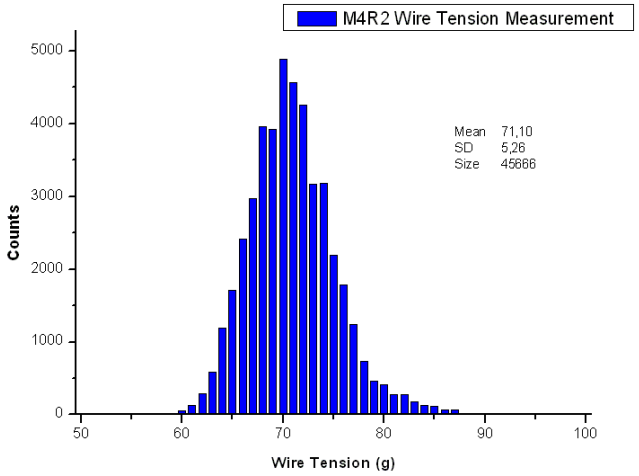

Figure 5.60: Wire tension distribution (g) for M4R2 panels.

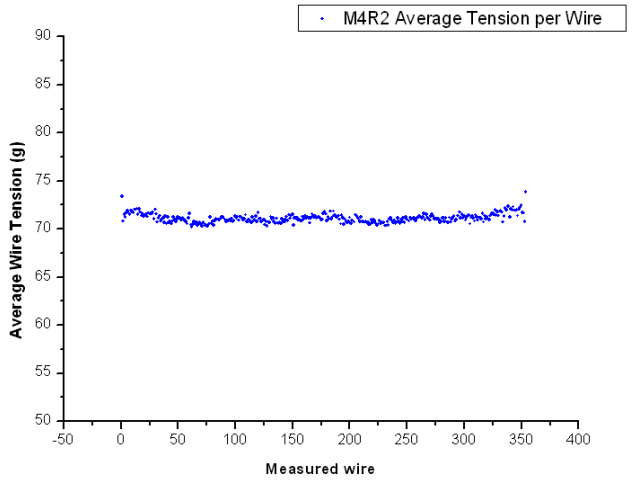

Figure 5.61: Average wire tension (g) vs wire number for M4R2 panels.

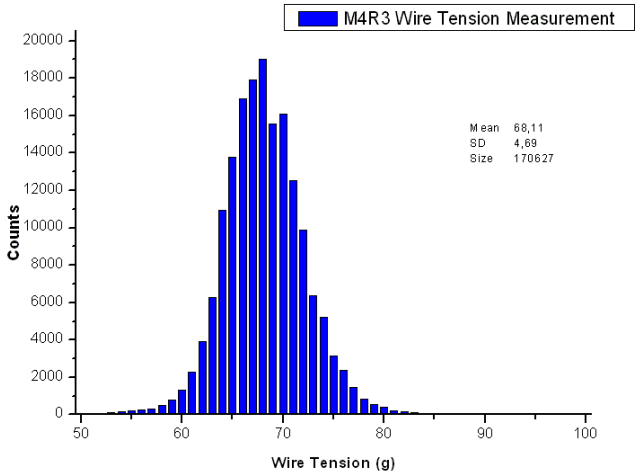

Figure 5.62: Wire tension distribution (g) for M4R3 panels.

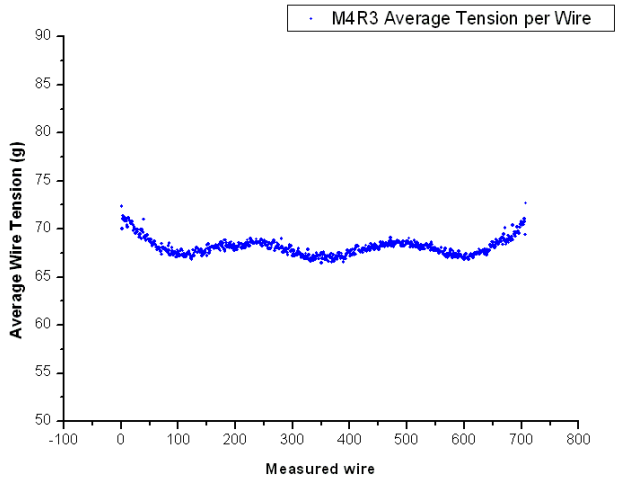

Figure 5.63: Average wire tension (g) vs wire number for M4R3 panels.

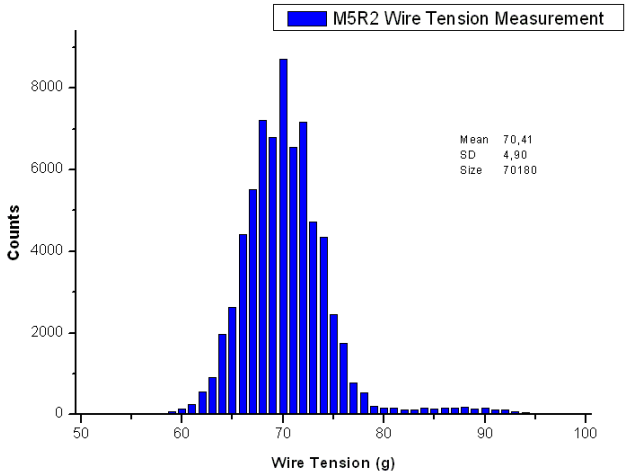

Figure 5.64: Wire tension distribution (g) for M5R2 panels.

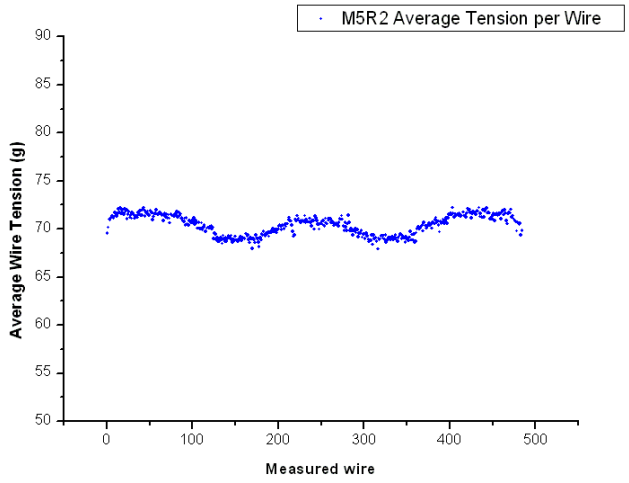

Figure 5.65: Average wire tension (g) vs wire number for M5R2 panels.

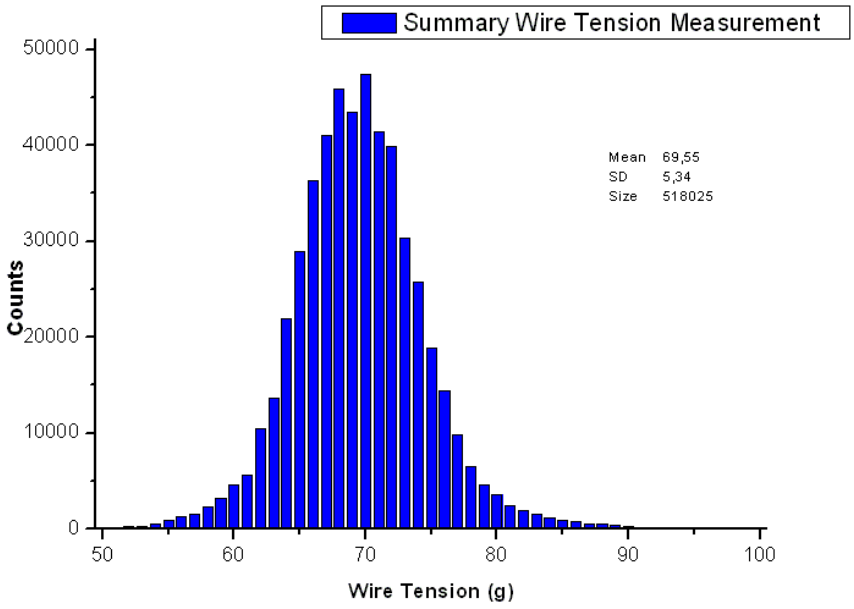

Figure 5.66: Wire tension distribution (g) for ALL panels.

5.5 Post-production Tests

Post-production tests are performed only on assembled chambers, made using the panels that successful passed preliminary and production tests. Here are presented results from all the 246 assembled chambers, divided by typology, and indicated by their chamber ID number. I personally collaborated in developing the testing system, and the analysis tools, still collaborating as usual on chamber tests.

5.5.1 Gas tightness test results

Over the total number of 246 assembled chambers, 237 passed the gas tightness test. The following plots indicate the final registered leak value referred to each single chamber, after any needed recovering procedure. All the rejected chambers presented very large leaks, so that it wasn't possible to reach the requested conditions for the test (5 *mbar* overpressure). Any recovering procedure was very dangerous with large leaks, indeed the first 6 M2R3 chambers repaired using the Adekit 140 black glue, and the other 3 chambers repaired using conformal coating weren't properly working at all. Here are summarized leak informations about each kind of chambers, and about the whole production:

- M1R4: 59 chambers (58 passed the leak test)
- M2R3: 67 chambers (61 passed the leak test)
- M4R2: 29 chambers (28 passed the leak test)
- M4R3: 56 chambers (55 passed the leak test)
- M5R2: 35 chambers (35 passed the leak test)

The overall average leak is 0.27 *mbar/h* (Standard deviation 0.22 *mbar/h*).

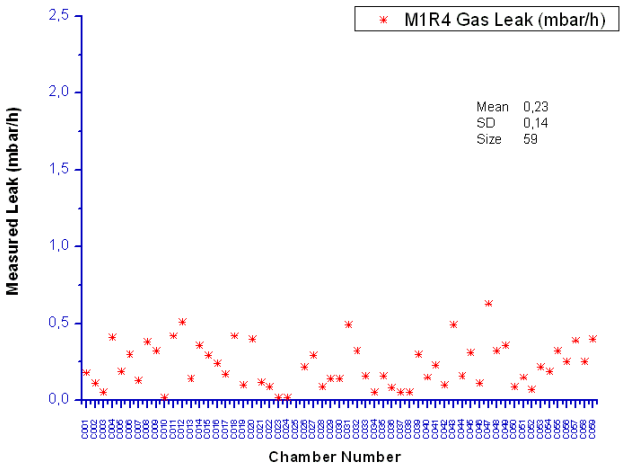

Figure 5.67: Measured leak (mbar/h) vs chamber ID number for M1R4 chambers.

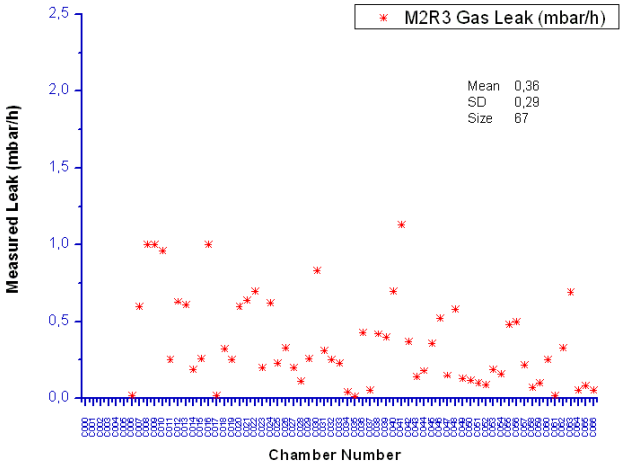

Figure 5.68: Measured leak (mbar/h) vs chamber ID number for M2R3 chambers.

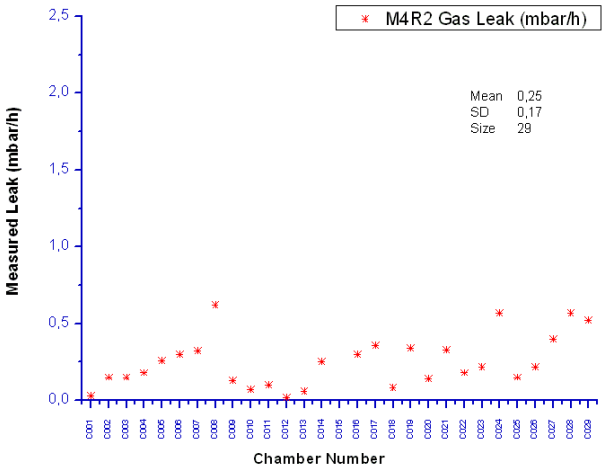

Figure 5.69: Measured leak (mbar/h) vs chamber ID number for M4R2 chambers.

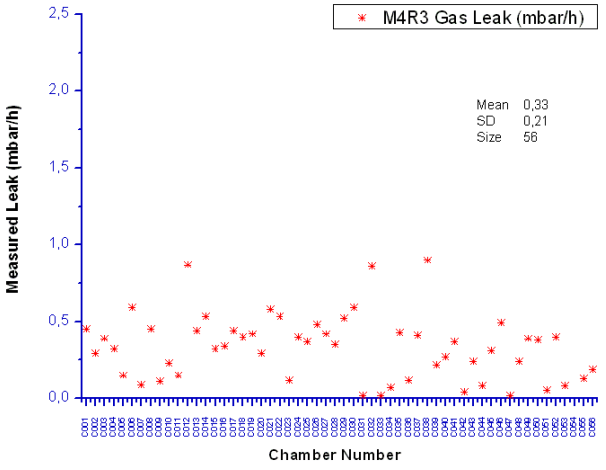

Figure 5.70: Measured leak (mbar/h) vs chamber ID number for M4R3 chambers.

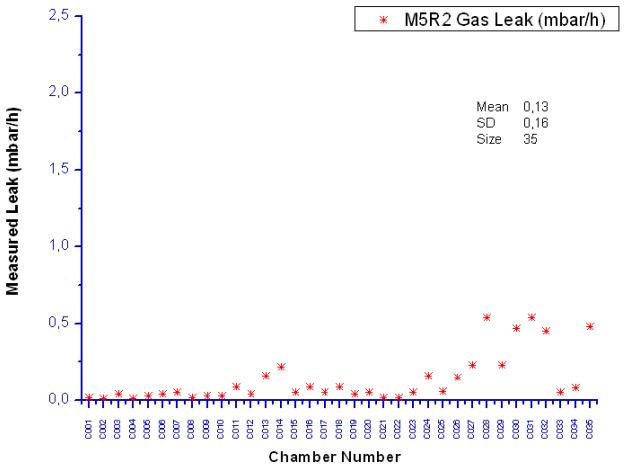

Figure 5.71: Measured leak (mbar/h) vs chamber ID number for M5R2 chambers.

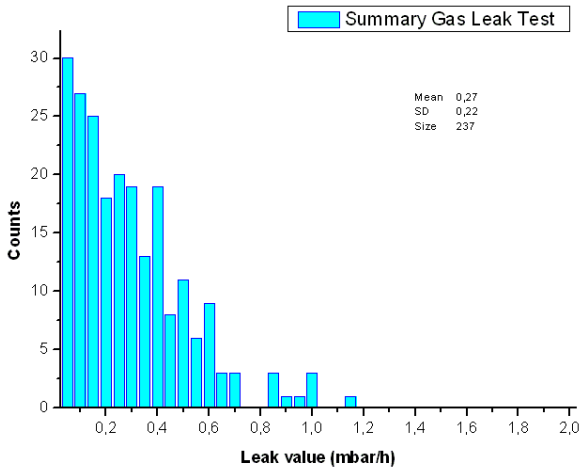

Figure 5.72: Leak value distribution (mbar/h) for ALL chambers.

5.5.2 HV test results

Over the total number of 246 assembled chambers, 227 passed the HV test. The following plots indicate the final registered average value on each chamber (referred to single gap) for the measured dark current (nA) at 2850 V. Most part of the bad chambers are M2R3 assembled during the training period. Chambers with broken wires inside, with conformal coating from gas tightness recovering inside, and with other problems that didn't allow to perform the HV test are considered as bad, and dark current values are not shown here. Here are summarized HV test informations about each kind of chambers, and about the whole production:

- M1R4: 59 chambers (58 passed the HV test)
- M2R3: 67 chambers (55 passed the leak test)
- M4R2: 29 chambers (28 passed the leak test)
- M4R3: 56 chambers (52 passed the leak test)
- M5R2: 35 chambers (34 passed the leak test)

The overall average dark current per single gap at 2850 V is 3.97 nA (Standard deviation 2.45 nA).

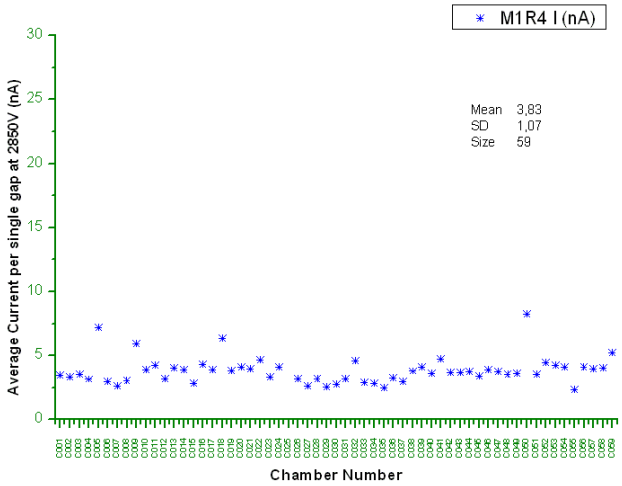

Figure 5.73: Average current per single gap (nA) at 2850V vs chamber ID number for M1R4 chambers.

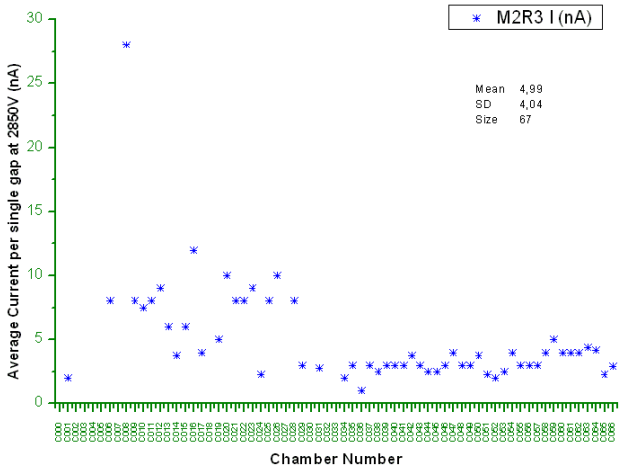

Figure 5.74: Average current per single gap (nA) at 2850V vs chamber ID number for M2R3 chambers.

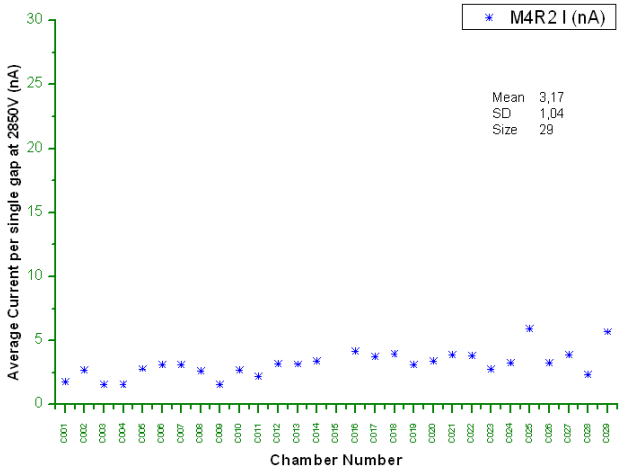

Figure 5.75: Average current per single gap (nA) at 2850V vs chamber ID number for M4R2 chambers.

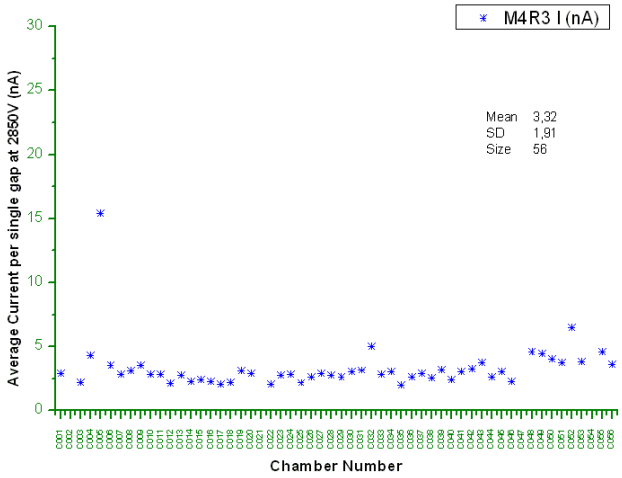

Figure 5.76: Average current per single gap (nA) at 2850V vs chamber ID number for M4R3 chambers.

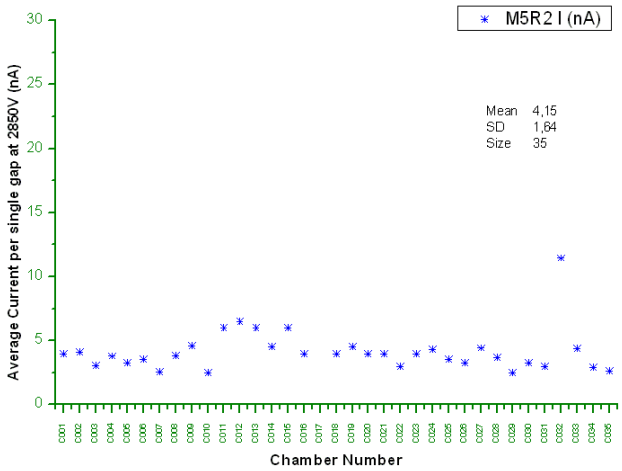

Figure 5.77: Average current per single gap (nA) at 2850V vs chamber ID number for M5R2 chambers.

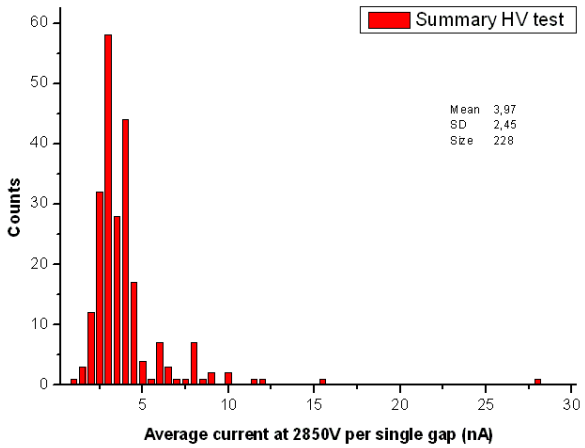

Figure 5.78: Average current per single gap (nA) at 2850V distribution for all chambers.

5.5.3 Gas gain uniformity test results

Gas gain uniformity test are performed only on chambers that passed gas tightness and HV tests, classification method and criteria are explained in section 4.3.3. A total of 217 chambers have been tested in Ferrara, all the chambers that didn't pass HV and gas tightness test haven't been tested for gas gain uniformity, also 5 of the first 14 chambers M2R3 type haven't been tested here, but in Roma 2 university, when the test table was still not working in Ferrara.

In this section are presented only results from the test performed in Ferrara, as usual they are divided by chamber typology, considering two separate bi-gaps (AB, CD) for all chambers but M1R4, that has only a single bi-gap. Average gas gain on all measured points normalized to 1 is represented by blue spots, vertical lines indicate the spread, while lower and upper cap indicate respectively minimum and maximum gain over all points. As for the other post-production test the tested chamber is indicated by its ID number.

Here are summarized gas gain uniformity test informations about each kind of chambers, and about the whole production:

- M1R4: 58 chambers tested (58 A quality)
- M2R3: 49 chambers (45 AA, 4 AB)
- M4R2: 28 chambers (26 AA, 2 BA)
- M4R3: 52 chambers (50 AA, 1 AB, 1 BA)
- M5R2: 30 chambers (26 AA, 2 AB, 1 CA, 1 CB)

Over a total of 227 chambers eligible for this test (considering HV and gas tightness test results), 217 have been tested, 5 have been excluded due to cathode surface problems (PP chambers) or to problem (e.g. broken wires) occurred after the HV test, then 5 have been tested outside Ferrara and resulted AA quality. The total number of good chambers is 220.

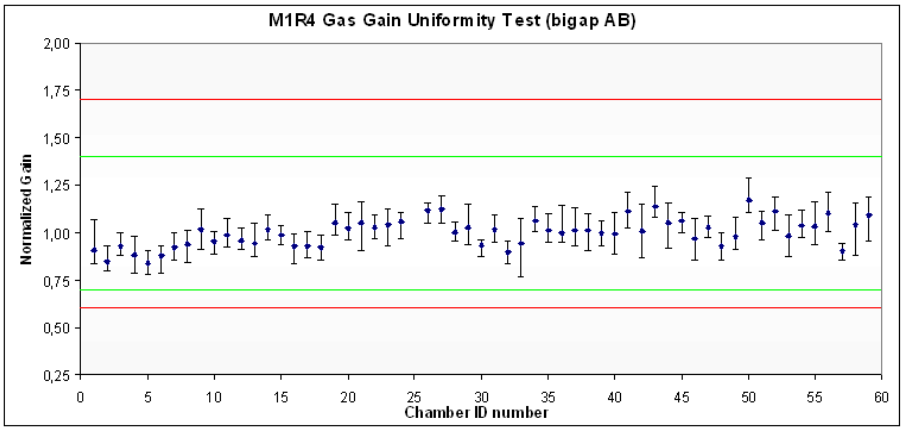

Figure 5.79: M1R4 Gas Gain Uniformity Test.

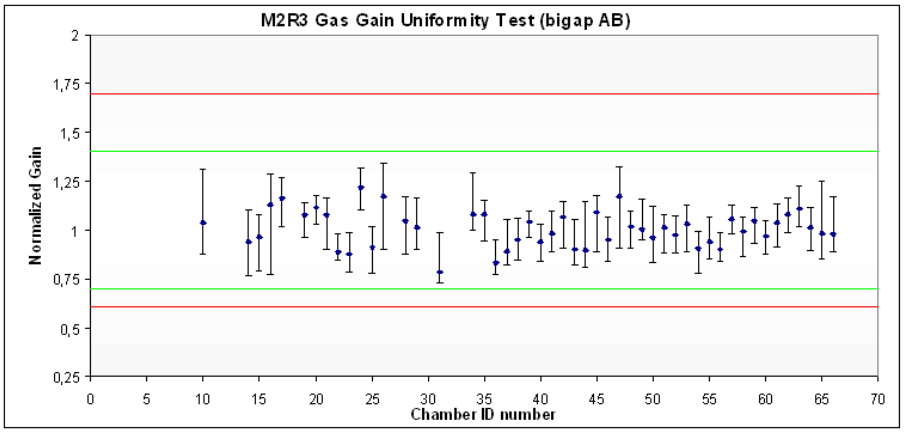

Figure 5.80: M2R3 (bi-gap AB) Gas Gain Uniformity Test.

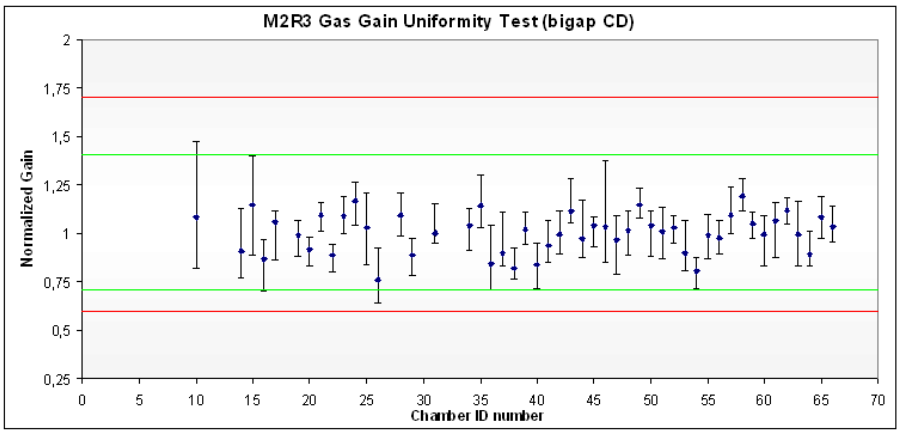

Figure 5.81: M2R3 (bi-gap CD) Gas Gain Uniformity Test.

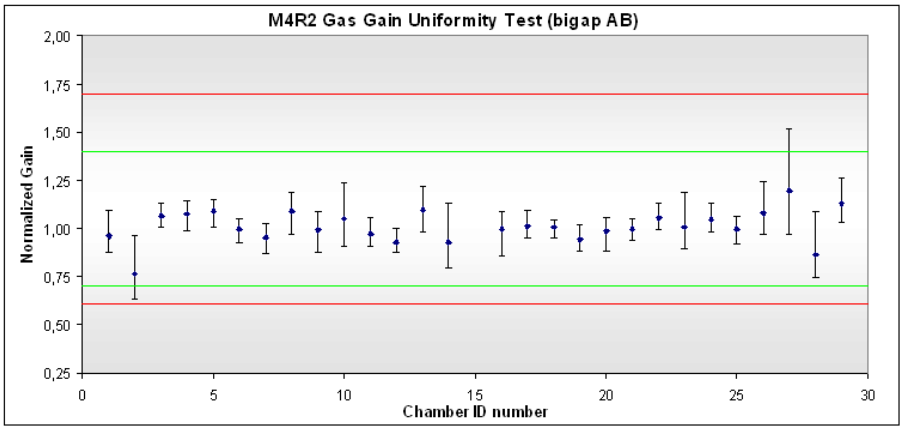

Figure 5.82: M4R2 (bi-gap AB) Gas Gain Uniformity Test.

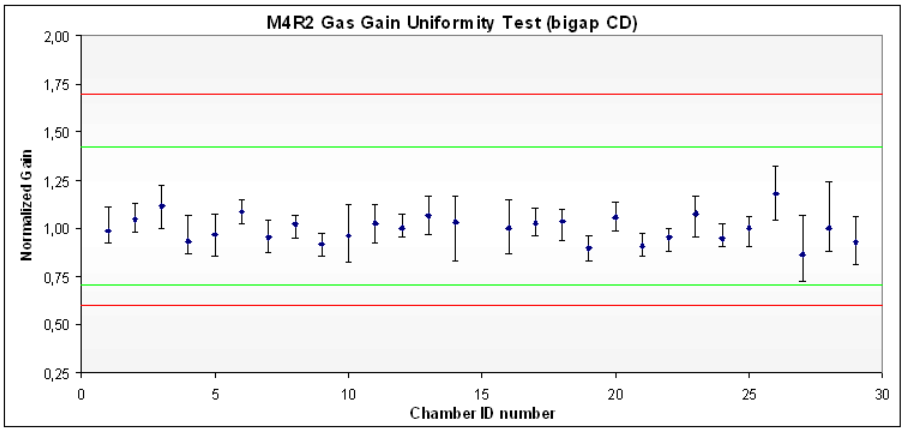

Figure 5.83: M4R2 (bi-gap CD) Gas Gain Uniformity Test.

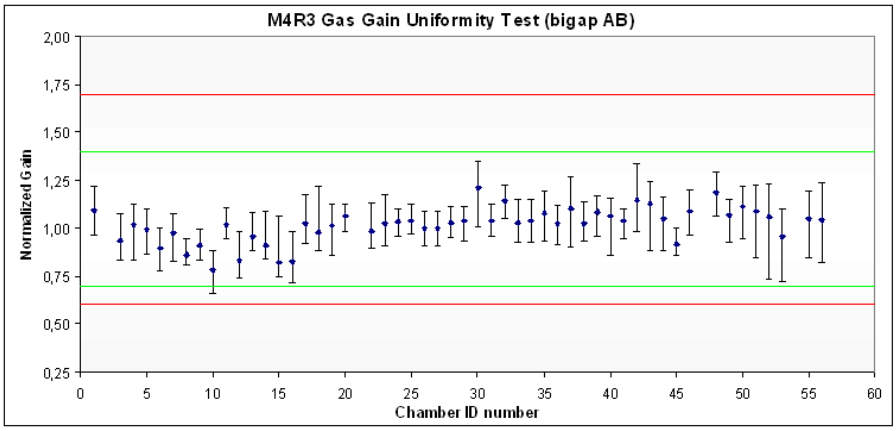

Figure 5.84: M4R3 (bi-gap AB) Gas Gain Uniformity Test.

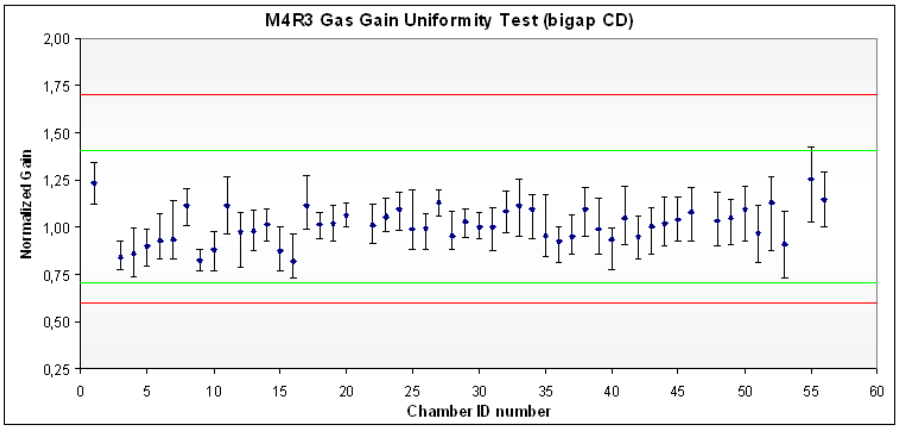

Figure 5.85: M4R3 (bi-gap CD) Gas Gain Uniformity Test.

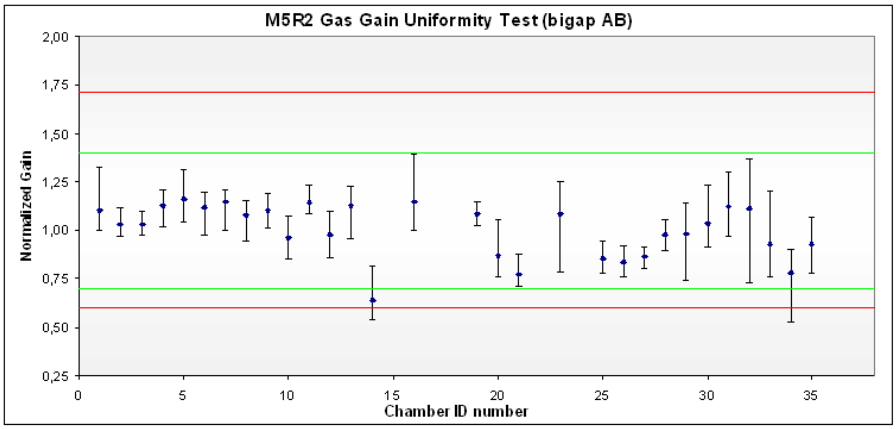

Figure 5.86: M5R2 (bi-gap AB) Gas Gain Uniformity Test.

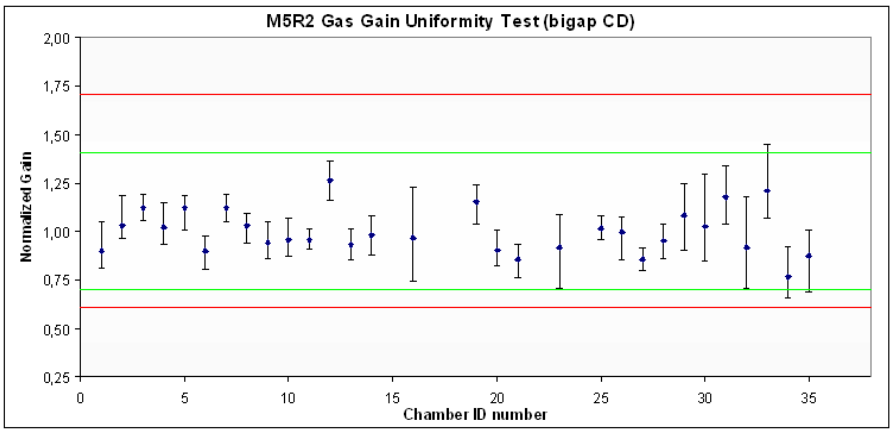

Figure 5.87: M5R2 (bi-gap CD) Gas Gain Uniformity Test.

Conclusions

The goal to construct the planned amount of MWPC for the LHCb Muon Detector has been achieved by the INFN Ferrara group during the period from the summer of year 2004 and the end of year 2006. The need of an effective Quality Management System was mandatory to ensure the satisfaction of the LHCb collaboration requirements, but also to solve the various problems encountered during the whole production period. My contribution to the LHCb Ferrara group expressed into the developing of the Quality assurance and Quality control (QaQc) System as well as on the large amount of measurements and data analysis made during the whole production in Ferrara. The realization of several tests and data analysis at the Gamma Irradiation Facility (GIF) at CERN has been also a relevant priority for my PhD studies.

A system of 6 main tests (HV bar height, Wire Pitch Measurement, Wire Tension Measurement, Gas tightness, Dark Current and Gas Gain Uniformity) continuously improved to guarantee the maximum of efficiency, allowed to construct and to test 246 MWPC, leading to the total number of 220 good chambers for the Muon Detector. Beam tests at high particle rate, carried out at the Gamma Irradiation Facility, allowed to found parasitic emissions from a particular type of cathodic surfaces, leading to exclude this materials from the following productions.

The whole QaQc System has been realized, and subsequently improved, referring to the guidelines given by the ISO 9001:2000 international standard for quality management systems, and the study and the application, where possible, of these guidelines has been also a notable part of my PhD work.

A continuous feedback from the quality tests data analysis is one of the fundamental principles stated into the ISO 9001:2000, those analysis have been carried out continuously during the whole period of my PhD, increasing the overall quality of the produced chambers time by time.

A total of 303 panels have been tested for HV bars height during the whole considered period leading to a final number of 24 rejected panels (7.9%), informations from this test gave us the possibility to ask for height corrections to our panels supplier, leading a considerable material quality enhancement after a problematic beginning (12 rejected panels over 81, 14.8%, in the first 6 months of production).

A total of 891 good (wired) panels have been constructed during the whole production period, and the system of 'on-line test software' and 'quick off-line

analysis' for wire pitch measurement and wire tension measurement, allowed to quickly identify potentially rejected panels, leading to successfully recover all of them before the chamber assembling.
Once assembled, 220 MWPCs over 246 passed all the tests (10,6% rejected), but a very large number of the rejected chambers (11 over 26, 42%) were assembled during the first 6 months of production leading also here to a considerable enhancement of the overall production quality. Moreover can be considered the problematic beginning as a 'training construction period', mandatory for any production center, and has not to be forgotten the cathode surface problem imputable only to material defectiveness and not the quality of production. All these considerations lead to better understand the real improvement given by an efficient QMS, and the real contribution given by the Ferrara group to the LHCb collaboration.

Bibliography

[1] A. D. Sakharov. *Violation of CP Invariance, CP Asymmetry, and Baryon Asymmetry of the Universe.* Pisma Zh. Eksp. Teor. Fiz., 5:32, 1967.

[2] I. J. R. Aitchison and A. J. G Hey. *Gauge Theories in Particle Physics.* Institute of Physics Publishing, 1996.

[3] J.H. Christenson et al. *Evidence for the 2π decay of the k_2^0 meson.* Phys. Rev. Lett., 13:138, 1964.

[4] BaBar Collaboration, B. Aubert et al., *Observation of CP violation in the B^0 meson system.* Phys. Rev. Lett., 87:091801 2001.

[5] BELLE Collaboration, K. Abe et al., *Observation of large CP violation in the neutral B meson system.* Phys. Rev. Lett., 87:091802, 2001.

[6] L. Wolfenstein. *Parametrization of the Kobayashi-Maskawa matrix.* Phys. Rev. Lett., 51:1945, 1983.

[7] S. Eidelman et al. *Review of Particle Physics.* Physics Letters B, 592, 2004.

[8] G. Gomez-Ceballos (CDF). *Measurement of the $B_s^0 - \bar{B}_s^0$ oscillation frequency.* Procs. 4th Flavor Physics and CP Violation Conference (FPCP 2006), Vancouver, April 2006.

[9] P. Ball et al. *B decays at the LHC.* 2000, hep-ph/0003238.

[10] M. Battaglia et al. *The CKM matrix and the unitarity triangle,* arXiv: hep-ph/0304132, 2003.

[11] B. Kayser, M. Kuroda, R. D. Peccei, and A. I. Sanda. *B hadronic asymmetries and spin correlations. Phys. Lett.*, B237:508, 1990.

[12] J. Charles et al., *[CKMfitter Group],* Eur. Phys. J. C41, 1 (2005), hep-ph/0406184.

[13] P. Lefèvre and T. Pettersson. *The Large Hadron Collider: conceptual design.* CERN/AC/95/05/LHC, 1995.

[14] ATLAS Collaboration, W.W. Armstrong et al. *ATLAS: Technical Proposal for a General-Purpose pp Experiment at the Large Hadron Collider at CERN.* CERN/LHCC/94-43, 1994.

[15] CMS Collaboration. *Technical Proposal.* CERN/LHCC/94-38, 1994.

[16] ALICE Collaboration, N. Ahmad et al. *A Large Ion Collider Experiment - Technical Proposal.* CERN/LHCC/95-71, 1995.

[17] LHCb Collaboration. *Technical Proposal.* CERN-LHCC/98-4, 1998.

[18] P. Nason et al. *Bottom production.* In Proceedings of the 1999 Workshop on Standard Model Physics at the LHC, volume CERN 2000-004, 1999.

[19] T. Nakada and O. Schneider. *LHCb Trigger.* In Proceedings of the 4th International Workshop on B Physics and CP Violation, February 19-23, 001, Ise-Shima (Japan).

[20] LHCb Collaboration. *LHCb Reoptimized Detector Design and Performance - Technical Design Report.* CERN/LHCC/2003-030, 2003.

[21] LHCb Collaboration. *LHCb VELO Technical Design Report.* CERN/LHCC/2001-0011.

[22] LHCb Collaboration. *LHCb RICH Technical Design Report.* CERN/LHCC/2000-0037.

[23] T. Gys et al. *Performance of Full-Scale Pixel HPD tubes in low Magnetic Fields.* LHCb 2000-69 RICH.

[24] LHCb Collaboration. *LHCb Inner Tracker Technical Design Report.* CERN/LHCC/2002-029.

[25] LHCb Collaboration. *LHCb Outer Tracker Technical Design Report.* CERN/LHCC/2001-026.

[26] LHCb Collaboration. *LHCb Magnet Technical Design Report.* CERN/LHCC/2000-007.

[27] LHCb Collaboration. *LHCb Calorimeters Technical Design Report.* CERN/LHCC/2000-036.

[28] LHCb Collaboration. *LHCb Muon System Technical Design Report.* CERN/LHCC/2001-010.

[29] LHCb Collaboration. *LHCb Trigger System Technical Design Report.* CERN/LHCC/2003-031.

[30] G. Barrand et al. *Gaudi - a software architecture and framework for building HEP data processing applications.* Comput. Phys. Commun., 140:45-55, 2001. LHCb Collaboration.

[31] D. J. Lange. *The EvtGen particle decay simulation package.* Nucl. Instrum. Meth. A, 462:152-155, 2001.

[32] S. Agostinelli et al. *Geant4: A simulation toolkit.* Nucl. Instr. and Meth. A, 506:250-303, 2003.

[33] R. Brun and F. Rademakers. *Root - an object orientated analysis framework.* Nucl. Instrum. Meth. A, 389:81-86, 1997.

[34] F. Sauli. *GEM: A new concept for electron amplification in gas detectors.* Nucl. Instr. and Meth. in Phys. Res. A,386:531, 1997.

[35] LHCb Collaboration. *Second Addendum to the LHCb Muon System Technical Design Report.* CERN/LHCC/2005-012.

[36] A. Balla et al. *The muon chamber mapping for the IB system.* LHCb 2004-004 Muon.

[37] W. Riegler. *Detector Physics and Performance Simulations of the MWPCs for the LHCb Muon System.* LHCb 2000-060 Muon.

[38] B. Schmidt et al. *Results from a 2 mm pitch MWPC prototype for the LHCb Muon System.* LHCb 2003-002 Muon.

[39] D. Moraes et al. *The CARIOCA Front End Chip for the LHCb muon chambers.* LHCb 2003-009 Muon.

[40] S. Cadeddu, C. Deplano and A. Lai. *The DIALOG chip in the front-end electronics of the LHCb Muon Detector.* IEEE Trans.Nucl.Sci. 0-783-8701-5, 2004.

[41] CARDIAC technical documentation: http://lhcb-muon.web.cern.ch/lhcb-muon/electronics/cardiac.html

[42] ISO 9001:2000. *Quality management systems - Requirements.* 2000.

[43] A. Kachtchouk et al. *Design and Construction of the Wire Chambers for the LHCb Muon System.* LHCb 2001-026, public note.

[44] W. Baldini et al. *A Laser Based Instrument for MWPC Wire Tension Measurement.* (Submitted, NIM).

[45] S. Agosteo et al. *A facility for the test of large-area muon chambers at high rates.* Nucl. Instrum. Meth. A, vol. 452, Mar. 2000.

[46] L. Malter. *Thin film field emission.* Phys.Rev.50 (1936), 48-54.

Ringraziamenti

Ringrazio in primo luogo il mio relatore, Prof. Mauro Savriè, da cui ho imparato molto, per tutti i suoi indispensabili consigli durante il mio lavoro e nella stesura del mia tesi. Ringrazio inoltre tutto il gruppo dei Muoni di LHCb per la costruttiva collaborazione instaurata in questi anni, e in particolare il Dr. Wander Baldini, per tutti i suoi preziosi consigli nonchè per le nostre utilissime discussioni.

Molti ringraziamenti vanno a mia madre, Gisella, per aver sempre sostenuto affettuosamente il mio lavoro, e a tutti i miei cari amici e colleghi, Diego, Irene, Susanna e Federico, per la loro presenza e il loro appoggio, che hanno reso questa esperienza ancora più interessante e piacevole nonchè ricca di stimoli per il futuro.

Il mio più grande ringraziamento va però a mio padre, Gianni, che più di ogni altro ha appoggiato e incoraggiato le mie scelte ogni singolo giorno della mia vita, prima della sua prematura scomparsa nel mese di marzo dello scorso anno.